AN ABSTRACT OF THE THESIS OF

Achim Hill for the degree of Doctor of Philosophy in Electrical and Computer Engineering presented on August 2, 1989.

Title: Quasi-TEM and Full Wave Numerical Methods for the Characterization of Microstrip Discontinuities

Redacted for privacy

Abstract approved: _____
Dr. Vijai K. Tripathi

Static and dynamic numerical techniques which are suited for the analysis and simulation of various planar microstrip components encountered in hybrid and monolithic microwave integrated circuits are presented. The static analysis makes use of an excess source formulation in conjunction with an efficient mathematical treatment to extract the discontinuity parameter for single and coupled microstrip bend discontinuities. The boundary value problem is solved in a moment method procedure where surface currents on a triangular subdomain are employed as basis functions for inductance calculations. Surface charges of constant magnitude together with their multiple images are used as expansion functions on a triangular domain for

capacitive computations. Two port equivalent circuit parameters are computed for single microstrip bends of variable bend angle and chamfer ratio. Equivalent circuits for the coupled microstrip bend four port are proposed and the circuit parameters are also computed for various bend angles.

In the second part of this work, a rigorous full wave analysis for shielded, passive microstrip components on a multilayered substrate is presented. The distinct feature of this technique is a novel, efficient formulation for establishing the system matrix in the moment method procedure which allows the derivation of the elements of any large matrix by a linear combination of elements in a precomputed index table. The table is obtained from a two-dimensional, discrete fast Fourier transform. In the moment method procedure, the two-dimensional surface current is represented by locally defined roof-top functions. The effect of the resonant modes, associated with the metallic enclosure on the numerical procedure are examined. Numerical results for various discontinuities including the microstrip open end, right angled bend with and without the compensated corner are computed by using the resonant technique and compared with other published computational and experimental data.

Quasi-TEM and Full Wave Numerical Methods for the Characterization of Microstrip Discontinuities

by

Achim Hill

A THESIS

submitted to

Oregon State University

in partial fullfilment of
the requirements for the degree of

Doctor of Philosophy

Completed August 2, 1989

Commencement June 1990

APPROVED:

Redacted for privacy

Professor of Electrical and Computer Engineering in charge of major

Redacted for privacy

Head of Electrical and Computer Engineering Department

Redacted for privacy

Dean of Graduate School

Date thesis is presented August 2, 1989

Typed by Achim Hill

Acknowledgements

Thanks is due to my major Professor, Dr. Vijai K. Tripathi for his encouragement and support.

Professors Dr. Joel Davis, Dr. Stephen Goodnick, Dr. Thomas Plant, Donald Amort and Dr. Toshimi Minoura are acknowledged for serving on my graduate committee and for reviewing the manuscript.

Contributions in form of discussions or correspondance by various collegues and friends from outside the campus are gratefully acknowledged. In particular I would like to express sincere thanks to Dr. N.H.L. Koster, University of Duisburg, Federal Republique of Germany; Ms. A. Skrivervik, Ecole Polytechnique Federale, Lausanne, Switzerland; Dr. J.R. Mautz, Syracuse University, New York; Dr. J. Rautio, Sonnet Software, Liverpool, New York and Mr. W.P. Harokopus, University of Michigan.

Further thanks is due to Mr. Claudio Fassardi from the Ocean Engineering Department at Oregon State University for providing various public domain software. Thanks is extended to my collegues Mr. Tagore Kollipara and Mr. Leonard Hayden for their help with measurements and to Mr. Andreas Weisshaar for programming the waveguide model.

Special thanks is due to Professors Dr.-Ing. W.H. Bloss and Dr. H. Sorg from the University of Stuttgart for their support of my desire to study a year in the USA.

I appreciate the support of the Fullbright Commission and the Friedrich-Ebert Studienstiftung during the beginning of my study abroad. Further funding throughout the course of this work was

provided by a research grant from EEsof Inc. in Westlake Village, California and by the Department of Electrical and Computer Engineering at Oregon State University in form of Teaching Assistantships.

Final thanks is due to my mother Amalie Hill, my brother Oliver Hill and to my friend Jayne Lukins for their understanding and patience and to my host family, the Balints, for their help and friendship.

TABLE OF CONTENTS

LIST OF FIGURES

LIST OF SYMBOLS

$\mathbf{A}$	Magnetic vector potential
A_{jn}	Area of triangle T_{jn}
a	Region on microstrip bend; width of shielding box
B	Magnetic flux density
b	Region on microstrip bend; length of shielding box
c	Region on microstrip bend; height of shielding box
C_e	Excess capacitance
CH	Chamfer ratio
e	Area coordinate
g	Gap width
H	Substrate height
H_1	Height of dielectric layer 1
H_2	Height of dielectric layer 2
I	Current
[I]	Identity matrix
J	Current density
j	Imaginary unit
k	Wave number
k_x, k_y, k_z	Components of wave number
k_0	Wave number in free space
l	Length of transmission line
l_a	Length of transmission line section in region a
l_c	Length of transmission line section in region c
L_e	Excess inductance
$\mathbf{l}_{jn}$	Vector on triangle T_{jn}, opposite interior node j

M	Number of subsection on discretized surface in x-direction
N	Number of interior nodes; number of subsection on discretized surface in y-direction
N_1	Number of interior nodes on conductor 1
N_2	Number of interior nodes on conductor 2
n	Unit vector normal to conductor surface
NJ	Number of triangles covered by J_j
NL1	Identification vector for l_{jn}, 1st node
NL2	Identification vector for l_{jn}, 2nd node
NLA	Number of nodes on line a
NLC	Number of nodes on line c
NN	Number of nodes on microstrip bend
NNT	Identification vector for triangles in terms of node numbers
NTA	Number of triangles on region a of microstrip bend
NTB	Number of triangles on region a and b of microstrip bend
NTC	Total number of triangles on microstrip bend
NTJ	Identification vector for triangle T_{jn} as defined by NNT
NVBA	Identification vector for nodes on line a that fall on a stripline edge
P	Unit pulse function over triangular domain
Q_e	Excess charge
Q	Total charge
q	Surface charge density
q_a	Surface charge density on region a
q_c	Surface charge density on region c
q_e	Excess charge density
RHS	Right hand side

r'	Position vector
r''	Image of r' about ground plane
S	Metallized surface
[S]	S parameter matrix
T_{jn}	Triangle n associated with interior node j
u	Scalar function, represents excess currents
U	Voltage
v	Speed of light in vacuum
W	Width of microstrip line
[Z']	Normalized network impedance matrix
Z	Characteristic impedance of transmission line
α	Bend angle
β	Propagation constant
Δx	Discretization in x-direction
Δy	Discretization in y-direction
ϵ_o	Permittivity in vacuum
ϵ_r	Relative dielectric constant
ϕ	Magnetic flux
ϕ_a	Magnetic flux per unit length of strip a
ϕ_c	Magnetic flux per unit length of strip c
Φ	Z-component of magnetic vector potential
ψ	Z-component of electric vector potential
μ_o	Permittivity in vacuum
$\nabla_s u$	Surface gradient of u
$\sum_m$	Summation over m, from m=0 to m=∞
ω	Angular frequency

QUASI-TEM AND FULL WAVE NUMERICAL METHODS FOR THE CHARACTERIZATION OF MICROSTRIP DISCONTINUITIES

1. INTRODUCTION

The process of high frequency integrated circuit design depends heavily on software tools. Before the manufacturing process it is most desirable to characterize the circuit structure in terms of its physical parameters such that a specified electrical performance is realized in an optimum sense. Deviations from desired performance parameters can be accounted for by changing certain geometries after fabrication of microwave integrated circuits (MICs). This, however, results in additional costs and is not practical for monolithic microwave integrated circuits (MMICs) where dimensions are small and certain structures remain inaccessible once the chip is manufactured. High costs for the fabrication of MIC and MMIC prototypes dictate a heavy dependence on accurate computer-aided design (CAD).

A large number of techniques to model passive as well as active structures have been developed in the past. Passive structures like striplines, parallel striplines in a multilayered medium, crossing striplines and various types of resonators have been characterized for quasi-static and high frequency operation. Discontinuities in strip width and direction are known as T-junctions, right angle bends, open circuits and gaps, for example. These structures are modeled in terms of a multiport consisting of equivalent lumped elements for quasi-TEM propagation or network parameters like impedance matrix or scattering matrix for hybrid field analysis. With decreasing dimensions in MICs

and higher operating frequencies, hybrid mode solutions become progressively important. In addition, closely spaced circuit elements can no longer be treated as isolated components. Electromagnetic coupling phenomena including surface waves and radiation effects demand an accurate analysis of high density circuits. Investigations of coupled discontinuities has been given little attention in the past. Due to recent advances in microwave and millimeter wave hybrid and monolithic circuit techniques, a development of computer-aided modeling tools for coupled discontinuities in a high density environment is essential for a successful design. Currently, a large number of research activities in the CAD area of MMICs are directed towards the analysis and improvement of discontinuity models since the "inadequacy of the modeling of junctions and discontinuities in transmission structures has been recognized as one of the key bottlenecks in microwave/mmwave CAD." Present techniques for rigorous full-wave treatments of boxed micro-strip structures require intensive computation times. Therefore, a development of accurate high speed techniques for the analysis of passive components is a necessity for cost-effective (M)MIC design.

Figure 1-1 shows various single and coupled microstrip discontinuities that can be characterized with the methods presented in this work.

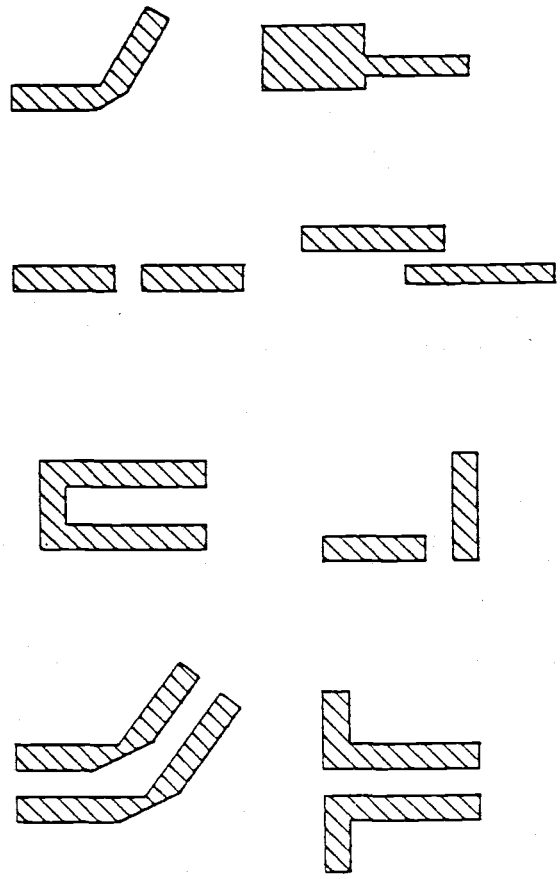

Figure 1-1. A class of microstrip two-port and four-port discontinuities.

2. ASSUMPTIONS

In this work microstrip lines on single- and double-layered dielectric interfaces are considered. All metallized surfaces are assumed to be of zero thickness. Dielectric layers are homogeneous, isotropic and nonmagnetic. Conductor losses as well as dielectric losses are zero.

For the electromagnetic field quantities a phase variation of the form $\exp(j\omega t - \beta x)$ is assumed. In the second part of this work geometries and frequencies were chosen such that only the fundamental microstrip mode propagates on the associated microstrip lines.

3. QUASI-STATIC ANALYSIS

3.1 Introduction

In the past, different methods have been developed for modeling planar microstrip discontinuities. Theoretical results based on quasi-static calculations together with experimental data are used to derive mathematical formulas which lead to fast computation times of discontinuity parameters [1-22]. In early papers, the discontinuity parameters were obtained from a subtraction of two almost equal numbers which resulted in large errors for the lumped elements in the equivalent circuit of the discontinuity.

In 1972 Silvester and Benedek introduced an excess charge technique which was applied to model a microstrip open circuit [5]. The formulation allows the direct calculation of charge deviation caused by the discontinuity and leads to a more accurate identification of discontinuity parameters. Moreover, the excess method overcame the limitations of previous methods which were restricted to finite length strips and thus could not represent the actual situation in which the strips extend so far from the discontinuity that they may be considered as semi-infinite. The excess charge technique became a standard for the computation of various discontinuity geometries. Subsequent publications were concerned with the modeling of the capacitive effect of microstrip gaps, step width changes, T junctions, crossings and right angle bends [6,8]. In 1974 Gopinath and Easter applied the excess technique to the evaluation of the corner inductance of a right angle bend which seemed to be superior to the skin effect formulation

"probably because current continuity through the discontinuity is not always maintained" [12]. Since a wire grid model was used in the expansion procedure of the moment method formulation results were inaccurate and the method required large storage space.

About 8 years later Rao et al. [37] state that the wire grid model is not well suited for calculating near field and surface quantities. The quasi-static methods for calculating excess discontinuity parameter were improved over the years and in 1978, final results for excess capacitances and inductances of various discontinuities were presented [17,18]. The major difference to earlier publications was the use of higher order finite element expansion functions over a rectangular domain. A skin effect formulation in conjunction with a generalized matrix inverse technique was used to assure auxiliary conditions such as the solenoidal property of the currents and tangential current flow at edges of conductors.

In 1984 Mautz and Harrington [39,40] used the excess technique in the evaluation of a microstrip via discontinuity. In contrast to the previous method, integral equations are derived from the boundary condition that the normal magnetic field be zero on the strip line surface. The governing equation is solved by the method of moments using pulse expansion functions on triangular patches.

An alternative technique in the evaluation of discontinuity effects is the magnetic wall wave guide model [25] which is able to predict frequency dependence within a limited range but does not directly define an equivalent circuit model for the discontinuity. The wave guide model is relatively straightforward to implement, but

has its limitations when coupled discontinuities are to be considered. The model replaces a microstrip line by a parallel plate waveguide with effective geometrical dimensions and dielectric constant. The model-waveguide is then used in the analysis of the discontinuities.

Quasi-static results for the equivalent parameter of single microstrip bend discontinuities have been published in the past. However the results of various publications differ considerably for the excess inductance. Due to this fact, the single microstrip bend has been analyzed again. In the proximity analysis, use is made of surface currents which is considered an improvement [37] as compared to [20] where a wire grid was used to model currents in the discontinuity region.

The excess parameters are derived in the following for rectangular geometries. For variable bend angle corresponding quantities have to be used in vectorized form with associated dot product.

3.2 Single Bend

3.2.1 Equivalent Circuit

An equivalent circuit to model the microstrip right angle corner has been suggested earlier [2]. The microstrip corner along with the equivalent circuit model is shown in Figures 3-1a and 3-1b, respectively. The shunt capacitance accounts for the stray field at the corner. The series inductances reflect the current crowding effect associated with the corner region. Variable bend angle and chamfer are assessed by the same equivalent circuit.

3.2.2 Excess Capacitance

Consider the microstrip discontinuities shown in Figure 3-1a. In region a, a microstrip line runs parallel to the z axis from $z = -\infty$ to $z = z_a$. In region c, a microstrip line runs parallel to the x axis from $x = x_c$ to $x = \infty$. The lines in region a and region c are connected through a right angle bend section in region b. All strips of width W and height H over a ground plane are mounted on a substrate with relative dielectric constant ϵ_r.

The excess capacitance is defined by

$$C_e = \lim_{\substack{l_a \to \infty \\ l_c \to \infty}} \frac{Q_e}{U} \tag{3.2.1}$$

where

$$Q_e = Q - l_a Q_a - l_c Q_c \tag{3.2.2}$$

The excess charge Q_e is decomposed into Q, the total charge on the striplines for $(-l_a < z, l_c > x)$ and the discontinuity region and the charge contributions $l_a Q_a$, $l_c Q_c$. Q_a corresponds to the charge per unit strip length on strip a that would be required to raise strip a to the potential U if the stripline in region c and the discontinuity in region b were absent and if strip a extended to infinity in the z direction. Similarly, Q_c is the charge per unit length on strip c that would be required to rise the potential on strip c to U if strip a and the discontinuity were removed and strip c extended to infinity in the x direction.

For l_a and l_c sufficiently large, the charges per unit length on strip a and strip c approach Q_a and Q_c respectively as the observation point is moved away from the discontinuity region b.

The excess charge is derived from an integral equation which is formulated by making use of the excess charge technique [5,39]. The definition of the charge in (3.2.2) implies

$$Q = \int q \, dS \tag{3.2.3}$$

$$Q_a = \int q_a \, dx \tag{3.2.4}$$

$$Q_c = \int q_c \, dz \tag{3.2.5}$$

q is the surface charge density that exists on the metallized surface S, q_a is the surface charge density that would be required to raise strip a to the potential U if strip c and the discontinuity region b were absent and if strip a extended to infinity; q_c is defined as the surface charge density on strip c that would be required to raise strip c to the potential U if strip a and the discontinuity region b were removed and strip c extended to infinity.

In order to avoid the large numerical error due to the subtraction in (3.2.2), q is expressed as

$$q = \begin{cases} q_e + q_a \text{ , region a} \\ q_e \text{ , region b} \\ q_e + q_c \text{ , region c} \end{cases} \tag{3.2.6}$$

The excess surface charge density q_e in (3.2.6) exists on region a,b and c. However, it approaches zero as the observation point moves away from the discontinuity region b.

Substituting (3.2.3)–(3.2.6) in (3.2.1) yields

$$C_e = \frac{1}{U} \int q_e \, dS \tag{3.2.7}$$

Integral equations for q_e, q_a and q_c are obtained in the following. Let

$$q_a^- = q_a \quad , \quad -\infty < z < z_a \tag{3.2.8}$$

$$q_a^+ = q_a \quad , \quad z_a < z < \infty \tag{3.2.9}$$

$$q_c^- = q_c \quad , \quad -\infty < x < x_c \tag{3.2.10}$$

$$q_c^+ = q_c \quad , \quad x_c < x < \infty \tag{3.2.11}$$

Substitution of (3.2.8)–(3.2.11) into (3.2.6) gives

$$q = q_e + q_a^- + q_c^+ \tag{3.2.12}$$

Using (3.2.12), the governing equation for excess potential is written as,

$$U(q_e) = U - U(q_a^-) - U(q_c^+) \tag{3.2.13}$$

The above equation is valid on the total metallized surface. To improve the accuracy in calculating $U(q_a^-)$ on region a and $U(q_c^+)$ on region c, substitute

$$q_a^- = q_a - q_a^+ \quad \text{on region a} \tag{3.2.14}$$

$$q_c^+ = q_c - q_c^- \quad \text{on region c} \tag{3.2.15}$$

in (3.2.13) and utilizing the fact that q_a and q_c raise the potential on the striplines to U yields

$$U(q_e) = \begin{cases} U(q_a^+) - U(q_c^+) \ , \text{ region a} \\ U - U(q_a^-) - U(q_c^+) \ , \text{ region b} \\ U(q_c^-) - U(q_a^-) \ , \text{ region c} \end{cases} \tag{3.2.16}$$

Note, in (3.2.16) on regions a and c no fields are evaluated on the source regions. The integral equation (3.2.16) is solved by first expanding the excess charge as

$$q_e = \sum_{j=1}^{N} a_j \, P_j(\mathbf{r}') \tag{3.2.17}$$

where P_j is the unit pulse function on triangle T_j.

$$P_j(\mathbf{r}') = \begin{cases} 1 \ , \ \mathbf{r}' \text{ on } T_j \\ 0 \ , \text{ otherwise} \end{cases} \tag{3.2.18}$$

Next (3.2.17) is substituted into (3.2.16) and (3.2.16) is enforced at the centroid of each triangular patch. The resulting matrix equation of dimension N is written as

$$[P] \, [A] = [V] \tag{3.2.19}$$

with $A_j = a_j$ and P_{ij} is the potential integral over the triangular surface T_j evaluated at the centroid of T_i. V_i is the right hand side of (3.2.16) evaluated at the centroids of T_i. Potential integrals in P_{ij} and V_i are given in the Appendix. Once (3.2.19) is solved for the coefficients a_j, the excess capacitance is computed from (3.2.7).

3.2.3 Excess Inductance

Consider the microstrip discontinuity in Figure 3-1a with geometry and regions as defined for the capacitive case.

The excess inductance is defined by

$$L_e = \lim_{\substack{l_a \to \infty \\ l_c \to \infty}} \frac{(\phi - l_a \phi_a - l_c \phi_c)}{I} \tag{3.2.20}$$

The quantities ϕ in (3.2.20) are defined in terms of the magnetostatic problem in which the total current I flows from $z = -\infty$ on region a through the discontinuity region b to $x = \infty$ on region c. ϕ is the magnetic flux which passes through a loop formed by the portion of the strips and discontinuity for which $(-l_a < z, x < l_c)$, the ground plane and connecting lines at $z = -l_a$ and $x = l_c$. The quantity ϕ_a (ϕ_c) is the magnetic flux per unit length of strip a (c) sufficiently far away from the discontinuity. The flux is defined as

$$\phi = \int_{S_1} \mathbf{B}(J) \cdot \mathbf{n} \, dS \tag{3.2.21}$$

where S_1 is the surface enclosed by the loop defined in the previous paragraph. $\mathbf{B}(J)$ is the magnetic field due to the existence of J in the presence of the ground plane, $\mathbf{n}$ is the unit vector normal to S_1. Expressing $\mathbf{B}$ in terms of magnetic vector potential and applying Stokes theorem yields

$$\phi = \int_{C_1} \mathbf{A}(J) \cdot d\mathbf{l} \tag{3.2.22}$$

where C_1 is the loop described in the paragraph that follows (3.2.20). From the image method it can be concluded that the tangential component of the magnetic vector potential on the ground plane vanishes. Far from the discontinuity the magnetostatic vector potential on strip a (c) is entirely z (x) directed. Therefore the path of integration along the ground plane and the connecting lines at $z = -l_a$ and $x = l_c$ does not contribute to the flux which reduces C_1 in (3.2.22). As has been shown in [40], an expression for the flux can be derived as

$$\phi = \frac{1}{I} \int A(J') \; J \; dS \tag{3.2.23}$$

where J is the total current distribution on S, J is the current density on the strip which is associated with the total current I, the excess current is not part of J. The total current associated with the excess current is zero.

In contrast to (3.2.23) the expression for ϕ in terms of stored energy is

$$\phi = \frac{1}{I} \int A(J') \; J' \; dS \tag{3.2.24}$$

For the computational implementation of the method, (3.2.23) leads to a more efficient evaluation of the flux as compared to (3.2.24).

In order to dispose of the subtractions in (3.2.20), the current J′ is decomposed as follows

$$J' = J_{abc} + J_e \tag{3.2.25}$$

where,

$$J_{abc} = \begin{cases} J_a \text{ , on strip a} & , -\infty < z < z_a \\ J_b \text{ , on region b} & , z > z_a \text{ , } x < x_c \\ J_c \text{ , on strip c} & , x_c < x < \infty \end{cases} \tag{3.2.26}$$

J′ approaches J_a and J_c far from the discontinuity on region a and c respectively. The total current of J_a and J_c is I. J_b is any solenoidal current density that assures continuous current flow from J_a on line a through the discontinuity to J_c on line c and exists only on the discontinuity region b.

Substituting J_{abc} for J in (3.2.23) and (3.2.25) for J′ in (3.2.23) yields

$$\phi = \frac{1}{I} \int A(J_{abc})\ J_{abc}\ dS + \frac{1}{I} \int A(J_e)\ J_{abc}\ dS \tag{3.2.27}$$

Introducing the new variables

$$J_a^- = J_a \quad , \quad -\infty < z < z_a$$

$$J_a^+ = J_a \quad , \quad z_a < z < \infty$$

$$J_c^- = J_c \quad , \quad -\infty < x < x_c$$

$$J_c^+ = J_c \quad , \quad x_c < x < \infty \tag{3.2.28}$$

letting currents J_a and J_c extend to infinity

$$J_a = J_a^- + J_a^+ \tag{3.2.29}$$

and

$$J_c = J_c^- + J_c^+ \tag{3.2.30}$$

using (3.2.29) and (3.2.30), (3.2.26) is recast as

$$J_{abc} = J_a^- + J_b + J_c^+ \tag{3.2.31}$$

Substituting J_{abc} in (3.2.27) by (3.2.31) and making use of (3.2.29) and (3.2.30) yields

$$\phi = \frac{1}{I}\int_a A(-J_a^+ + J_b + J_c^+ + J_e)\, J_a^-\, dS$$

$$+ \frac{1}{I}\int_b A(J_a^- + J_b + J_c^+ + J_e)\, J_b\, dS$$

$$+ \frac{1}{I}\int_c A(-J_c^- + J_b + J_a^- + J_e)\, J_c^+\, dS$$

$$+ \frac{1}{I}\int_a A(J_a)\, J_a^-\, dS$$

$$+ \frac{1}{I}\int_c A(J_c)\, J_c^+\, dS \qquad (3.2.32)$$

The sum of the last two integrals in the expressions for ϕ are recognized as

$$l_a\, \phi_a + l_c\, \phi_c \qquad (3.2.33)$$

Substituting (3.2.32) with (3.2.33) in (3.2.20) leads to the evaluation of the excess inductance without performing the subtractions in (3.2.20) which enhances the accuracy of the method. After performing the substitutions, the final expression for L_e becomes

$$L_e = \frac{1}{I^2}\left(\int_a A(J_c^+ - J_a^+ + J_e + J_b)\, J_a^-\, dS\right.$$

$$+ \int_b A(J_a^- + J_c^+ + J_e + J_b)\, J_b\, dS$$

$$\left. + \int_c A(J_a^- - J_c^- + J_e + J_b)\, J_c^+\, dS\right) \qquad (3.2.34)$$

In order to compute (3.2.34) the excess current distributions J_e needs to be determined. The strip current J_a and J_c are obtained from the standard moment method technique [60]. In evaluating the excess current, triangular basis functions are used in the moment method procedure. For excess calculations of a single discontinuity, this approach has been used previously in [40]. The computation of J_e is outlined in the following.

Substituting (3.2.25) in the boundary condition that the magnetic field be zero on the metallized surface S yields

$$\mathbf{n}\cdot\nabla \times \mathbf{A}(J_e) = -\mathbf{n}\cdot\nabla \times \mathbf{A}(J_{abc}) \tag{3.2.35}$$

Due to the solenoidal character of J_e there exists a scalar function u such that [40]

$$J_e = \mathbf{n} \times \nabla_s u(\mathbf{r}) \tag{3.2.36}$$

Construction of the moment solution of (3.2.35) is begun by expanding u as

$$u = I \sum_{j=1}^{N} a_j u_j \tag{3.2.37}$$

where u_j are expansion functions on S and a_j are constants to be determined. The discontinuity region b and the truncated strip regions a and c are modeled by triangular patches [38]. The triangles are chosen such that none of them crosses the lines $z = z_a$ and $x = x_c$. Each triangle is either entirely on strip a, entirely on the discontinuity region b, or entirely on strip c. Consider each triangle of which one vertex is the j^{th} interior node on S. Called (T_{jn}, n =

$1,2,\ldots N_j$), these triangles encircle the j^{th} interior node on S. The set of these triangles is the domain of u_j; u_j is expressed in terms of area coordinates e_{jn} associated with the vertex of T_{jn}

$$u_j = e_{jn} \quad , \quad n = 1,2,\ldots N_j \tag{3.2.38}$$

If J_j is the expansion function for J_e associated with u_j then

$$J_j = \mathbf{n} \times \nabla_s u_j(\mathbf{r}) = \frac{\mathbf{l}_{jn}}{2A_{jn}} \quad \text{on } T_{jn} \ , \ n = 1,2,\ldots N_j \tag{3.2.39}$$

where $\mathbf{l}_{jn}$ is a vector whose length is the length of the side of T_{jn} opposite the j^{th} interior node on S. A_{jn} is the area of the triangle T_{jn} on S.

Testing (3.2.35) with u_k on S yields

$$\int u_k \, \mathbf{n}\cdot\nabla \times \mathbf{A}(J_e) \, dS = -\int u_k \, \mathbf{n}\cdot\nabla \times \mathbf{A}(J_{abc}) \, dS \tag{3.2.40}$$

Using Stokes' theorem [40], (3.2.40) is converted to

$$\int J_k \, \mathbf{A}(J_e) \, dS = -\int J_k \, \mathbf{A}(J_{abc}) \, dS \tag{3.2.41}$$

The right hand side (RHS) of (3.2.41) is replaced by a form which is more suitable for calculation. Let the RHS of (3.2.41) be

$$R = R_a + R_b + R_c \tag{3.2.42}$$

where R_a, R_b and R_c are the RHS of (3.2.41) evaluated over the region a,b and c respectively. After substituting (3.2.31) in (3.2.42) and making use of the fact that the normal magnetic field on a line with the removed discontinuity is zero, the following expressions are obtained

$$R_a = -\int_a J_k \, A(-J_a^+ + J_b + J_c^+) \, dS \tag{3.2.43}$$

$$R_b = -\int_b J_k \, A(J_a^- + J_b + J_c^+) \, dS \tag{3.2.44}$$

$$R_c = -\int_c J_k \, A(J_a^- + J_b - J_c^-) \, dS \tag{3.2.45}$$

Note that in (3.2.43) and (3.2.45), the points of evaluation are free of source currents which enhances the accuracy of the solution. The following linear system results from the testing procedure in the moment method:

$$[P]\,[A] = [V] \tag{3.2.46}$$

where A represents the unkonwn coefficients in the expansion (3.2.37). Matrix elements are given by

$$P_{kl} = \sum_{m=1}^{N_k} \frac{l_{mk}}{2} [A(J_l)]^{mk} \qquad \begin{matrix} k = 1,2,\ldots N \\ l = 1,2,\ldots N \end{matrix} \tag{3.2.47}$$

where the superscript mk denotes evaluation at the centroid of T_{mk} and

$$[A(J_l)]^{mk} = \frac{\mu_o}{8\pi} \sum_{n=1}^{N_l} \frac{l}{A_{nl}} G(mk,nl) \tag{3.2.48}$$

with

$$G(mk,nl) = l_{nl} \int \frac{ds'}{|\mathbf{r}^{mk} - \mathbf{r}'|} - l_{nl} \int \frac{ds'}{|\mathbf{r}^{mk} - \mathbf{r}''|} \tag{3.2.49}$$

where $\mathbf{r}'$ is the position vector of the differential element of area ds', $\mathbf{r}''$ is the image of $\mathbf{r}'$ about the ground plane, and $\mathbf{r}^{mk}$ is the radius vector to the centroid of T_{mk}. Expressions for the integrals

in (3.2.49) have been developed in [38]. The RHS of (3.2.46) is given by

$$V_k = -\frac{1}{I}\sum_{m=1}^{N_k}\frac{l_{mk}}{2}\,[A(J_{abc})]^{mk} \tag{3.2.50}$$

where

$$\begin{aligned}[A(J_{abc})]^{mk} &= [A(-J_a^+ + J_b + J_c^+)]^{mk} && \text{on region a}\\ &= [A(J_a^- + J_b + J_c^+)]^{mk} && \text{on region b}\\ &= [A(J_a^- + J_b - J_c^-)]^{mk} && \text{on region c}\end{aligned} \tag{3.2.51}$$

J_b is expressed as

$$J_b = \frac{I\,l_{bn}}{2\,A_{bn}} \qquad \text{on } T_{bn},\ n = 1,2,\ldots,N_{N+1} \tag{3.2.52}$$

where A_{bn} is the area of T_{bn} and l_{bn} is a vector that is independent of position on T_{bn}. The normalized vector potential due to J_b is computed from

$$A(J_b)^{mk}/I = \frac{\mu_o}{8\pi}\sum_{n=1}^{N_{N+1}}\frac{1}{A_{bn}}\,G(mk,bn) \tag{3.2.53}$$

where N_{N+1} is the number of triangles on which J_b exists.

In (3.2.53), G(mk,nl) is given by (3.2.49) where l_{bn} is defined such that a continuous current flow from strip a through the discontinuity to strip c is maintained. Expressions for the integrals in (3.2.51) are given in the Appendix.

Once the excess current is determined from (3.2.46), the excess inductance can be computed from (3.2.34).

3.3 Coupled Bends

3.3.1 Equivalent Circuit

In order to incorporate coupling effects between the microstrip bend discontinuities shown in Figure 3-2a, an equivalent circuit is suggested in Figure 3-2c [23]. The coupled bends represent a four port with one symmetry plane and their characterization requires the determination of six model parameters. Bends with variable angles can be described by the same equivalent circuit. The coefficients of the excess capacitance and excess inductance matrix are related to the circuit parameter of Figure 3-2c by

$$C_1 = C_{11e} - C_{12e}$$

$$C_2 = C_{22e} - C_{12e}$$

$$C_m = -C_{12e}$$

$$L_1 = L_{11e}$$

$$L_2 = L_{22e}$$

$$L_m = L_{12e} \qquad (3.3.1)$$

3.3.2 Excess Capacitance Matrix

Consider the two closely spaced microstrip discontinuities shown in Figure 3-2a. In region a, two uniform coupled lines run parallel to the z axis from $z = -\infty$ to $z = z_a$. In region c, two uniform coupled lines run parallel to the x axis from $x = x_c$ to $x = \infty$. The lines in region a and c are connected through right angle bend sections in region b. All strips of width W and height H over a ground plane are

mounted on a substrate with relative dielectric constant ϵ_r. The excess capacitance matrix is defined by

$$\begin{bmatrix} Q_{e1} \\ Q_{e2} \end{bmatrix} = \begin{bmatrix} C_{11e} & C_{12e} \\ C_{21e} & C_{22e} \end{bmatrix} \begin{bmatrix} U_1 \\ U_2 \end{bmatrix} \tag{3.3.2}$$

where

$$\begin{aligned} Q_{e1} &= \lim_{\substack{l_a \to \infty \\ l_c \to \infty}} (Q_1 - l_a Q_{a1} - l_c Q_{c1}) \\ Q_{e2} &= \lim_{\substack{l_a \to \infty \\ l_c \to \infty}} (Q_2 - l_a Q_{a2} - l_c Q_{c2}) \end{aligned} \tag{3.3.3}$$

The excess charge $\mathbf{Q}_e = (Q_{e1}, Q_{e2})$ on conductors 1 and 2 is decomposed into $\mathbf{Q} = (Q_1, Q_2)$, the total charge on conductors 1 and 2 for ($-l_a < z$, $l_c > x$) and the charge contributions $l_a \mathbf{Q}_a$ and $l_c \mathbf{Q}_c$. $\mathbf{Q}_a$ corresponds to the charge per unit strip length on the uniformly coupled transmission lines in region a that would be required to raise strips 1 and 2 to the potential $\mathbf{U} = (U_1, U_2)$ if the striplines in region c and the discontinuity in region b were absent and if the coupled strips in region a extended to infinity in the z direction. A similar definition holds for $\mathbf{Q}_c$. The excess capacitance matrix in (3.3.2) can be computed by applying successively two voltage vectors $\mathbf{U}$, $(U_1, U_2) = (1,0)$, $(U_1, U_2) = (0,1)$. The corresponding excess charges are derived from an integral equation which is formulated by making use of the excess charge technique [5]. The definition of the charges in (3.3.3) imply

$$Q_i = \int q_i \, dS_i \tag{3.3.4}$$

$$Q_{ai} = \int q_{ai} \, dx_i \tag{3.3.5}$$

$$Q_{ci} = \int q_{ci} \, dz_i \tag{3.3.6}$$

$q = (q_1, q_2)$ is the surface charge density that exists on the metallized surface S, $q_a = (q_{a1}, q_{a2})$ is the surface charge density that would be required to raise the striplines in region a to the potential $U = (U_1, U_2)$ if the striplines in region c and the discontinuity region b were absent and if the strip lines in region a extended to infinity. A similar argument holds for $q_c = (q_{c1}, q_{c2})$.

In order to avoid the large numerical error due to the subtraction in (3.3.3), q_i is expressed as

$$q_i = \begin{cases} q_{ei} + q_{ai} \;, & \text{region } a_i \\ q_{ei} \;, & \text{region } b_i \\ q_{ei} + q_{ci} \;, & \text{region } c_i \end{cases} \tag{3.3.7}$$

The excess surface charge density q_{ei} in (3.3.7) exists on region a_i, b_i and c_i. However, it approaches zero as the observation point moves away from the discontinuity region b_i.

Substituting (3.3.4)-(3.3.7) in (3.3.3) yields

$$Q_{e1} = \int q_{e1} \, dS_1 \tag{3.3.8}$$

$$Q_{e2} = \int q_{e2} \, dS_2 \tag{3.3.9}$$

Integral equations for q_{ei} are obtained in the following. Let

$$q_{ai}^{-} = q_{ai} \quad , \quad -\infty < z < z_a \tag{3.3.10}$$

$$q_{ai}^{+} = q_{ai} \quad , \quad z_a < z < \infty \tag{3.3.11}$$

$$q_{ci}^{-} = q_{ci} \quad , \quad -\infty < x < x_c \tag{3.3.12}$$

$$q_{ci}^{+} = q_{ci} \quad , \quad x_c < x < \infty \tag{3.3.13}$$

Substitution of (3.3.10) through (3.3.13) into (3.3.7) gives

$$q_i = q_{ei} + q_{ai}^{-} + q_{ci}^{+} \tag{3.3.14}$$

Using (3.3.14), the governing equation for the excess potential is written as

$$U(q_e) = U - U(q_a^{-}) - U(q_c^{+}) \tag{3.3.15}$$

The above equation is valid on the total metallized surface. To improve the accuracy in calculating $U_i(q_a^{-})$ on region a_i and $U_i(q_c^{+})$ on region c_i, substitute

$$q_a^{-} = q_a - q_a^{+} \qquad \text{on region a} \tag{3.3.16}$$

$$q_c^{+} = q_c - q_c^{-} \qquad \text{on region c} \tag{3.3.17}$$

in (3.3.14) and utilizing the fact that q_a and q_c raise the potential on the striplines to U yields

$$U_i(q_e) = \begin{cases} U_i(q_a^{+}) - U_i(q_c^{+}) & , \quad \text{region } a_i \\ U_i - U_i(q_a^{-}) - U_i(q_c^{+}), & \quad \text{region } b_i \\ U_i(q_c^{-}) - U_i(q_a^{-}) & , \quad \text{region } c_i \end{cases} \tag{3.3.18}$$

Note in (3.3.18) on regions a_i and c_i no fields are evaluated on source regions. In order to alleviate storage requirements, (3.3.18) is evaluated iteratively, at step n the excess potential on strip 1 is

$$U_1(q_{e1(n+1)}) = \begin{cases} U_1(q_a^+) - U_1(q_c^+) - U_1(q_{e2n}), & \text{region } a_1 \\ U_1 - U_1(q_a^-) - U_1(q_c^+) - U_1(q_{e2n}), & \text{region } b_1 \\ U_1(q_c^-) - U_1(q_a^-) - U_1(q_{e2n}), & \text{region } c_1 \end{cases} \tag{3.3.19}$$

On strip 2, (3.3.19) applies with subscript 1 and 2 exchanged. The excess charges in (3.3.19) are expanded in a moment solution over a triangular region.

$$q_{ein} = \sum_{j=1}^{N_i} a_{ijn} P_{ij} \tag{3.3.20}$$

Substituting (3.3.20) in (3.3.19) and enforcing (3.3.19) at the centroids of the triangular patches on S results in a linear system of the form

$$\begin{aligned} P_1 A_{1(n+1)} &= V_1 - R_{2n} \\ P_2 A_{2(n+1)} &= V_2 - R_{1n} \end{aligned} \tag{3.3.21}$$

P_{ikl} represents the potential integral over the triangular patch T_{il} evaluated at the centroid of T_{ik}, $A_{i(n+1)l} = a_{il(n+1)}$ where a_{iln} is defined in (3.3.20). The RHS of (3.3.21) is given by the RHS of (3.3.19), again evaluated at the centroids of T_{ik}. The RHS of (3.3.21) is partitioned into V and R which allows an efficient numerical treatment. R_{1n}, for instance, represents the part of the RHS of (3.3.19) which corresponds to the integral over the triangular patch of the excess charge on conductor S_2 at the n^{th} iteration. R_{in} accounts for the coupling between the bends and needs to be updated at each iterative step. V_i corresponds to the remaining portion of the RHS in (3.3.19) and is computed once at the beginning of the algorithm

together with the matrix P_i in (3.3.21). P_i is stored in a suitable array in its LU decomposed form which is applied to subsequent iterations. R_{in} is obtained from a multiplication of the solution vector A with a potential vector that again is computed once at the beginning of the algorithm. Application of the iterative procedure as outlined above leads to a reduction of storage requirements by a factor of two as compared to the direct evaluation of (3.3.18).

The potential integrals that occur in the evaluation of P, V and R in (3.3.21) are given in the Appendix.

3.3.3 Excess Inductance Matrix

Consider the microstrip discontinuity in Figure 3-2b with defined regions a_i, b_i, c_i.

The excess inductance matrix is defined by

$$\begin{bmatrix} \phi_{e1} \\ \phi_{e2} \end{bmatrix} = \begin{bmatrix} L_{11e} & L_{12e} \\ L_{21e} & L_{22e} \end{bmatrix} \begin{bmatrix} I_1 \\ I_2 \end{bmatrix} \tag{3.3.22}$$

where

$$\begin{aligned} \phi_{e1} &= \lim_{\substack{l_a \to \infty \\ l_c \to \infty}} (\phi_1 - l_a \phi_{a1} - l_c \phi_{c1}) \\ \phi_{e2} &= \lim_{\substack{l_a \to \infty \\ l_c \to \infty}} (\phi_2 - l_a \phi_{a2} - l_c \phi_{c2}) \end{aligned} \tag{3.3.23}$$

The quantities ϕ in (3.3.23) are defined in terms of the magnetostatic problem in which the total current $I = (I_1, I_2)$ flows from $z = -\infty$ on region a through the discontinuity region b to $x = \infty$ on region c. ϕ_i

is the magnetic flux which passes through a loop formed by the portion of the strips and discontinuity for which ($-l_a < z,\ x < l_c$), the ground plane and connecting lines at $z = -l_a$ and $x = l_c$. The quantity $\phi_{ai}(\phi_{ci})$ is the magnetic flux per unit length of strip a_i (c_i) far from the discontinuity. An expression for the flux ϕ_1 on conductor 1 and ϕ_2 on conductor 2 can be derived in the same manner as was done for the single microstrip bend in section 3.2.3. The flux on conductor 1 due to the current distribution on conductor 1 in the presence of conductor 2 is referred to as ϕ_{11}, the flux on conductor 1 due to the current distribution on conductor 2 is referred to as ϕ_{12}. A similar argument holds for conductor 2. For the flux $\phi_1 = \phi_{11} + \phi_{12}$ and $\phi_2 = \phi_{21} + \phi_{22}$, the following expressions can be derived

$$\phi_{11} = \frac{1}{I_1} \int \mathbf{A}(J_1')\ J_1\ dS_1 \tag{3.3.24}$$

$$\phi_{12} = \frac{1}{I_1} \int \mathbf{A}(J_2')\ J_1\ dS_1 \tag{3.3.25}$$

$$\phi_{21} = \frac{1}{I_2} \int \mathbf{A}(J_1')\ J_2\ dS_2 \tag{3.3.26}$$

$$\phi_{22} = \frac{1}{I_2} \int \mathbf{A}(J_2')\ J_2\ dS_2 \tag{3.3.27}$$

where J_i' is the total current distribution on strip i, J_i is the current distribution on strip i which is associated with the total current I_i; the excess current is not part of J_i. The total current associated with the excess current is zero.

In order to dispose of the subtractions in (3.3.20) the currents J_1 and J_2 are decomposed as follows

$$J_i' = J_{iabc} + J_{ei} \tag{3.3.28}$$

where

$$J_{iabc} = \begin{cases} J_{ai} \text{ , on strip } a_i \text{ , } -\infty < z < z_b \\ J_{bi} \text{ , on region } b_i \text{ , } z_b < z,\ x < x_b \\ J_{ci} \text{ , on strip } c_i \text{ , } x_b < x < \infty \end{cases} \tag{3.3.29}$$

J_{ai} and J_{ci} are asymptotic values of the current densities that J_i' approaches as we go far from the discontinuity on strip a_i and c_i, respectively. The integral of J_{ai} and J_{ci} over the strip width is referred to as the total current of J_{ai} and J_{ci}, respectively. The total current of J_{ai} and J_{ci} is I_i. The total current of J_{ei} is zero. J_{bi} is any solenoidal discontinuity current density that assures continuous current flow from J_{ai} on line a_i through the discontinuity to J_{ci} on line c_i, and exists only on the discontinuity region b_i. Substituting J_{iabc} for J_i in (3.3.24)-(3.3.27) and (3.3.28) for J_i' in (3.3.24)-(3.3.27) yields

$$\phi_{11} = \frac{1}{I_1} \int A(J_{1abc}+J_{e1})\ J_{1abc}\ dS_1 \tag{3.3.30}$$

$$\phi_{12} = \frac{1}{I_1} \int A(J_{2abc}+J_{e2})\ J_{1abc}\ dS_1 \tag{3.3.31}$$

$$\phi_{21} = \frac{1}{I_2} \int A(J_{1abc}+J_{e1})\ J_{2abc}\ dS_2 \tag{3.3.32}$$

$$\phi_{22} = \frac{1}{I_2} \int A(J_{2abc}+J_{e2})\ J_{2abc}\ dS_2 \tag{3.3.33}$$

Introducing the new variables

$$J^{-}_{ai} = J_{ai} \ , \ -\infty < z < z_a$$

$$J^{+}_{ai} = J_{ai} \ , \ z_a < z < \infty$$

$$J^{-}_{ci} = J_{ci} \ , \ -\infty < x < x_c$$

$$J^{+}_{ci} = J_{ci} \ , \ x_c < x < \infty$$

$$J^{++}_{a1} = J_{a1} \ , \ z_b < z < \infty$$

$$J^{--}_{a1} = J_{a1} \ , \ -\infty < z < z_b$$

$$J^{++}_{c1} = J_{c1} \ , \ x_b < x < \infty$$

$$J^{--}_{c1} = J_{c1} \ , \ -\infty < x < x_b \qquad (3.3.34)$$

letting J_{ai} and J_{ci} approach infinity leads to

$$J_{ai} = J^{--}_{ai} + J^{++}_{ai} = J^{-}_{ai} + J^{+}_{ai} \qquad (3.3.35)$$

and

$$J_{ci} = J^{--}_{ci} + J^{++}_{ci} = J^{-}_{ci} + J^{+}_{ci} \qquad (3.3.36)$$

using (3.3.35) and (3.3.36), (3.3.29) is recast as

$$J_{iabc} = J^{--}_{ai} + J_{bi} + J^{++}_{ci} = J^{-}_{ai} + J_{bi} + J^{+}_{ci} \qquad (3.3.37)$$

Substituting J_{iabc} in (3.3.24) and (3.3.25) by (3.3.37) and making use of (3.3.34) yields

$$\begin{aligned}
\phi_{11} = \frac{1}{I_1} \int_{a_1} & A(-J^{++}_{a1} + J_{b1} + J^{++}_{c1} + J_{e1}) \ J_{a1} \ dS_1 \\
& + \frac{1}{I_1} \int_{b_1} A(J^{--}_{a1} + J_{b1} + J^{++}_{c1} + J_{e1}) \ J_{b1} \ dS_1 \\
& + \frac{1}{I_1} \int_{c_1} A(-J^{--}_{c1} + J_{b1} + J^{--}_{a1} + J_{e1}) \ J_{c1} \ dS_1 \\
& + \frac{1}{I_1} \int_{\substack{a_1 \\ z \le z_a}} A(J_{a1}) \ J_{a1} \ dS_1 + \frac{1}{I_1} \int_{\substack{c_1 \\ x \ge x_c}} A(J_{c1}) \ J_{c1} \ dS_1 \\
& + \frac{1}{I_1} \int_{\substack{a_1 \\ z_a < z < z_b}} A(J_{a1}) \ J_{a1} \ dS_1 + \frac{1}{I_1} \int_{\substack{c_1 \\ x_b < x < x_c}} A(J_{c1}) \ J_{c1} \ dS_1
\end{aligned} \qquad (3.3.38)$$

and

$$\phi_{12} = \frac{1}{I_1}\int_{a_1} A(-J_{a2}^{+} + J_{b2} + J_{c2}^{+} + J_{e2})\ J_{a1}\ dS_1$$
$$+ \frac{1}{I_1}\int_{b_1} A(J_{a2}^{-} + J_{b2} + J_{c2}^{+} + J_{e2})\ J_{b1}\ dS_1$$
$$+ \frac{1}{I_1}\int_{c_1} A(-J_{c2}^{-} + J_{b2} + J_{a2}^{-} + J_{e2})\ J_{c1}\ dS_1$$
$$+ \frac{1}{I_1}\int_{\substack{a_1 \\ z\le z_a}} A(J_{a2})\ J_{a1}\ dS_1 + \frac{1}{I_1}\int_{\substack{c_1 \\ x\ge x_c}} A(J_{c2})\ J_{c1}\ dS_1$$
$$+ \frac{1}{I_1}\int_{\substack{a_1 \\ z_a<z<z_b}} A(J_{a2})\ J_{a1}\ dS_1 + \frac{1}{I_1}\int_{\substack{c_1 \\ x_b<x<x_c}} A(J_{c2})\ J_{c1}\ dS_1 \qquad (3.3.39)$$

The last two integrals in the expressions for ϕ_{11} and ϕ_{12} are combined to give

$$l_a\ \phi_{a1} + l_c\ \phi_{c1} + (z_b - z_a + x_c - x_b)\ (L_{11w} + L_{12w})\ I_1 \qquad (3.3.40)$$

where L_{11w} and L_{12w} represent the inductance coefficients per unit length of the uniform coupled microstrip lines far away from the discontinuity. ϕ_{a1} and ϕ_{c1} are defined in the paragraph that follows (3.3.23).

Substituting J_{iabc} in (3.3.26) and (3.3.27) by (3.3.37) and making use of (3.3.34) yields

$$\phi_{22} = \frac{1}{I_2}\int_{a_2} A(-J_{a2}^{+} + J_{b2} + J_{c2}^{+} + J_{e2})\ J_{a2}\ dS_2$$
$$+ \frac{1}{I_2}\int_{b_2} A(J_{a2}^{-} + J_{b2} + J_{c2}^{+} + J_{e2})\ J_{b2}\ dS_2$$
$$+ \frac{1}{I_2}\int_{c_2} A(-J_{c2}^{-} + J_{b2} + J_{a2}^{-} + J_{e2})\ J_{c2}\ dS_2$$
$$+ \frac{1}{I_2}\int_{a_2} A(J_{a2})\ J_{a2}\ dS_2 + \frac{1}{I_2}\int_{c_2} A(J_{c2})\ J_{c2}\ dS_2 \qquad (3.3.41)$$

and

$$\phi_{21} = \frac{1}{I_2}\int_{a_2} A(-J_{a1}^{++} + J_{b1} + J_{c1}^{++} + J_{e1})\ J_{a2}\ dS_2$$

$$+ \frac{1}{I_2}\int_{b_2} A(J_{a1}^{--} + J_{b1} + J_{c1}^{++} + J_{e1})\ J_{b2}\ dS_2$$

$$+ \frac{1}{I_2}\int_{c_2} A(-J_{c1}^{--} + J_{b1} + J_{a1}^{--} + J_{e1})\ J_{c2}\ dS_2$$

$$+ \frac{1}{I_2}\int_{a_2} A(J_{a1})\ J_{a2}\ dS_2 + \frac{1}{I_2}\int_{c_2} A(J_{c1})\ J_{c2}\ dS_2 \quad (3.3.42)$$

The last two integrals in the expressions for ϕ_{22} and ϕ_{21} are combined to give

$$l_a\ \phi_{a2} + l_c\ \phi_{c2} \quad (3.3.43)$$

ϕ_{a2} and ϕ_{c2} are defined in the paragraph that follows (3.3.23).

Now the excess flux in (3.3.22) can be computed without performing the subtractions in (3.3.23) which enhances the accuracy of the method. Expressions for the excess flux

$$\phi_{e1} = \phi_{e11} + \phi_{e12} \quad (3.3.44)$$

$$\phi_{e2} = \phi_{e21} + \phi_{e22} \quad (3.3.45)$$

are summarized as follows

$$\phi_{e11} = \frac{1}{I_1}\int_{a_1} A(-J_{a1}^{++} + J_{b1} + J_{c1}^{++} + J_{e1})\ J_{a1}\ dS_1$$

$$+ \frac{1}{I_1}\int_{b_1} A(J_{a1}^{--} + J_{b1} + J_{c1}^{++} + J_{e1})\ J_{b1}\ dS_1$$

$$+ \frac{1}{I_1}\int_{c_1} A(-J_{c1}^{--} + J_{b1} + J_{a1}^{--} + J_{e1})\ J_{c1}\ dS_1$$

$$+ (z_b - z_a + x_c - x_b)\ L_{11w} \quad (3.3.46)$$

$$\phi_{e12} = \frac{1}{I_1}\int_{a_1} A(-J^{+}_{a2} + J_{b2} + J^{+}_{c2} + J_{e2})\ J_{a1}\ dS_1$$

$$+ \frac{1}{I_1}\int_{b_1} A(J^{-}_{a2} + J_{b2} + J^{+}_{c2} + J_{e2})\ J_{b1}\ dS_1$$

$$+ \frac{1}{I_1}\int_{c_1} A(-J^{-}_{c2} + J_{b2} + J^{-}_{a2} + J_{e2})\ J_{c1}\ dS_1$$

$$+ (z_b - z_a + x_c - x_b)\ L_{12w} \qquad (3.3.47)$$

$$\phi_{e22} = \frac{1}{I_2}\int_{a_2} A(-J^{+}_{a2} + J_{b2} + J^{+}_{c2} + J_{e2})\ J_{a2}\ dS_2$$

$$+ \frac{1}{I_2}\int_{b_2} A(J^{-}_{a2} + J_{b2} + J^{+}_{c2} + J_{e2})\ J_{b2}\ dS_2$$

$$+ \frac{1}{I_2}\int_{c_2} A(-J^{-}_{c2} + J_{b2} + J^{-}_{a2} + J_{e2})\ J_{c2}\ dS_2 \qquad (3.3.48)$$

$$\phi_{e21} = \frac{1}{I_2}\int_{a_2} A(-J^{++}_{a1} + J_{b1} + J^{++}_{c1} + J_{e1})\ J_{a2}\ dS_2$$

$$+ \frac{1}{I_2}\int_{b_2} A(J^{--}_{a1} + J_{b1} + J^{++}_{c1} + J_{e1})\ J_{b2}\ dS_2$$

$$+ \frac{1}{I_2}\int_{c_2} A(-J^{--}_{c1} + J_{b1} + J^{--}_{a1} + J_{e1})\ J_{c2}\ dS_2 \qquad (3.3.49)$$

The comparison of (3.3.46)-(3.3.49) and (3.3.44)-(3.3.45) with (3.3.22) leads to the identification of the inductance coefficients

$$L_{e11} = \frac{\phi_{e11}}{I_1} \qquad (3.3.50)$$

$$L_{e12} = \frac{\phi_{e12}}{I_1} \qquad (3.3.51)$$

$$L_{e21} = \frac{\phi_{e21}}{I_2} \qquad (3.3.52)$$

$$L_{e22} = \frac{\phi_{e22}}{I_2} \qquad (3.3.53)$$

By reciprocity, (3.3.51) and (3.3.52) have to be identical which provides a means of checking the formulation.

In order to compute (3.3.46) through (3.3.49), the excess current distribution $\mathbf{J}_e$ needs to be evaluated. In the following, integral equations for $\mathbf{J}_e$ are derived.

Substituting (3.3.28) in the boundary condition that the magnetic field be zero on the metallized surface S yields

$$\mathbf{n}\cdot\nabla \times \mathbf{A}(\mathbf{J}_{e1} + \mathbf{J}_{e2}) = -\mathbf{n}\cdot\nabla \times \mathbf{A}(\mathbf{J}_{1abc} + \mathbf{J}_{2abc}) \tag{3.3.54}$$

Due to the solenoidal character of $\mathbf{J}_{ei}$, there exists a scalar function u_i such that [40]

$$\mathbf{J}_{ei} = \mathbf{n} \times \nabla_s u_i(\mathbf{r}) \tag{3.3.55}$$

Construction of the moment solution of (3.3.54) is begun by expanding u_i as

$$u_i = I_i \sum_{j=1}^{N_i} a_{ji}\, u_{ji} \tag{3.3.56}$$

where u_{ji} are expansion functions on strip i and a_{ji} are constants to be determined. The discontinuity region b_i and the truncated strip regions a_i,c_i are modeled by triangular patches. The triangles are chosen such that none of them crosses the lines $z = z_a$ and $x = x_c$. Each triangle is either entirely on strip a_i, or entirely on the discontinuity region or entirely on strip c_i. Consider each triangle of which one vertex is the j^{th} interior node on S_i. Called (T_{jni}, n = 1,2,...,N_{ji}) these triangles encircle the j^{th} interior node on S_i. The set of these triangles is the domain of u_{ji}. u_{ji} is expressed in terms of area coordinates e_{jni} associated with the vertex of T_{jni}

$$u_{ji} = e_{jni} \qquad n = 1,2,\ldots,N_{ji} \tag{3.3.57}$$

If J_{ji} is the expansion function for J_{ei} associated with u_{ji} then

$$J_{ji} = \mathbf{n} \times \nabla_s u_{ji}(\mathbf{r}) = \frac{l_{jni}}{2A_{jni}} \qquad \text{on } T_{jni}\ ,\ n = 1,2,\ldots,N_{ji} \tag{3.3.58}$$

where l_{jni} is a vector whose length is the length of the side of T_{jni} opposite the j^{th} interior node on S_i. A_{jni} is the area of the triangle T_{jni} on S_i.

Testing (3.3.54) with u_{k1} on S_1 and u_{k2} on S_2 yields

$$\int u_{k1}\ \mathbf{n}\cdot\nabla \times A_1(J_{e1} + J_{e2})dS_1 = -\int u_{k1}\ \mathbf{n}\cdot\nabla \times A_1(J_{1abc} + J_{2abc})\ dS_1 \tag{3.3.59}$$

$$\int u_{k2}\ \mathbf{n}\cdot\nabla \times A_2(J_{e1} + J_{e2})dS_2 = -\int u_{k2}\ \mathbf{n}\cdot\nabla \times A_2(J_{1abc} + J_{2abc})\ dS_2 \tag{3.3.60}$$

Using Stokes' theorem [40] (3.3.59) and (3.3.60) are converted to

$$\int J_{k1}\ A_1(J_{e1} + J_{e2})\ dS_1 = -\int J_{k1}\ A_1(J_{1abc} + J_{2abc})\ dS_1 \tag{3.3.61}$$

$$\int J_{k2}\ A_2(J_{e1} + J_{e2})\ dS_2 = -\int J_{k2}\ A_2(J_{1abc} + J_{2abc})\ dS_2 \tag{3.3.62}$$

The RHS of (3.3.61) is replaced by a form which is more suitable for calculation. Let the RHS of (3.3.61) be

$$R_1 = R_{a1} + R_{b1} + R_{c1} \tag{3.3.63}$$

where R_{a1}, R_{b1}, and R_{c1} are the RHS of equation (3.3.61) evaluated over the region a_1, b_1 and c_1, respectively. After substituting (3.3.37) and (3.3.34) in (3.3.61) and making use of the fact that the normal magnetic field on two uniform coupled lines with the discontinuity removed is zero, the following expressions are obtained

$$R_{a1} = -\int J_{k1}\, A(-J_{a1}^{++} - J_{a2}^{+} + J_{b1} + J_{b2} + J_{c1}^{++} + J_{c2}^{+})\, dS_1 \tag{3.3.64}$$

$$R_{b1} = -\int J_{k1}\, A(J_{a1}^{--} + J_{a2}^{-} + J_{b1} + J_{b2} + J_{c1}^{++} + J_{c2}^{+})\, dS_1 \tag{3.3.65}$$

$$R_{c1} = -\int J_{k1}\, A(J_{a1}^{--} + J_{a2}^{-} + J_{b1} + J_{b2} - J_{c1}^{--} - J_{c2}^{-})\, dS_1 \tag{3.3.66}$$

Note that in (3.3.64) and (3.3.66) the integrations are performed over source free regions which enhances the accuracy of the solution. The RHS of (3.3.62) is decomposed in a similar manner and the result for

$$R_2 = R_{a2} + R_{b2} + R_{c2} \tag{3.3.67}$$

is given by

$$R_{a2} = -\int J_{k2}\, A(-J_{a2}^{+} - J_{a1}^{++} + J_{b1} + J_{b2} + J_{c1}^{++} + J_{c2}^{+})\, dS_2 \tag{3.3.68}$$

$$R_{b2} = -\int J_{k2}\, A(J_{a1}^{--} + J_{a2}^{-} + J_{b1} + J_{b2} + J_{c1}^{++} + J_{c2}^{+})\, dS_2 \tag{3.3.69}$$

$$R_{c2} = -\int J_{k2}\, A(J_{a1}^{--} + J_{a2}^{-} + J_{b1} + J_{b2} - J_{c1}^{--} - J_{c2}^{-})\, dS_1 \tag{3.3.70}$$

Again, the points of evaluation in (3.3.68) and (3.3.70) are free of source currents.

The final form of the linear system which results from the testing procedure in the moment method is given by

$$\begin{bmatrix} P_{11} & P_{12} \\ P_{21} & P_{22} \end{bmatrix} \begin{bmatrix} A_1 \\ A_2 \end{bmatrix} = \begin{bmatrix} V_1 \\ V_2 \end{bmatrix} \tag{3.3.71}$$

which is solved iteratively, at step n

$$\begin{aligned} P_{11}\, A_{1(n+1)} &= V_1 - P_{12}\, A_{2n} \\ P_{22}\, A_{2(n+1)} &= V_2 - P_{21}\, A_{1n} \end{aligned} \tag{3.3.72}$$

with matrix elements

$$P_{k1l1} = \sum_{m_1=1}^{N_{k1}} \frac{\mathcal{I}_{m1k1}}{2} [A(J_{l1})]^{m1k1}. \qquad \begin{matrix} k1 = 1,2,\ldots,N_1 \\ l1 = 1,2,\ldots,N_1 \end{matrix} \tag{3.3.73}$$

where the superscript m1k1 denotes evaluation at the centroid of T_{m1k1} and

$$[A(J_{l1})]^{m1k1} = \frac{\mu_o}{8\pi} \sum_{n_1=1}^{N_{l1}} \frac{1}{A_{nl1}} G(m1k1,nl11) \tag{3.3.74}$$

with G(m1k1,nl11) given by (3.2.49). In (3.3.72) vectors A_i contain the expansion coefficients of the basis elements as defined in (3.3.56). Expressions for the potential integrals in (3.3.72) are the same as for single structures and are given in the Appendix. The remaining expressions in (3.3.72) are defined as

$$P_{k1l2} = \frac{I_2}{I_1} \sum_{m_1=1}^{N_{k1}} \frac{\mathcal{I}_{m1k1}}{2} [A(J_{l2})]^{m1k1}. \qquad \begin{matrix} k1 = 1,2,\ldots,N_1 \\ l2 = 1,2,\ldots,N_2 \end{matrix} \tag{3.3.75}$$

$$P_{k2l1} = \frac{I_1}{I_2} \sum_{m_2=1}^{N_{k2}} \frac{\mathcal{I}_{m2k2}}{2} [A(J_{l1})]^{m2k2}. \qquad \begin{matrix} k2 = 1,2,\ldots,N_2 \\ l1 = 1,2,\ldots,N_1 \end{matrix} \tag{3.3.76}$$

$$P_{k2l2} = \sum_{m_2=1}^{N_{k2}} \frac{\mathcal{I}_{m2k2}}{2} [A(J_{l2})]^{m2k2}. \qquad \begin{matrix} k2 = 1,2,\ldots,N_2 \\ l2 = 1,2,\ldots,N_2 \end{matrix} \tag{3.3.77}$$

and

$$V_1 = -\frac{1}{I_1} \sum_{m_1=1}^{N_{k1}} \frac{\mathcal{I}_{m1k1}}{2} [A(J_{1abc} + J_{2abc})]^{m1k1} \tag{3.3.78}$$

$$V_2 = -\frac{1}{I_2}\sum_{m_2=1}^{N_{k2}} \frac{l_{m2k2}}{2}\,[A(J_{1abc} + J_{2abc})]^{m2k2} \tag{3.3.79}$$

where

$$\begin{aligned}[A(J_{1abc}+J_{2abc})]^{m1k1} &= [A(-J_{a1}^{++}- J_{a2}^{+}+ J_{b1}+ J_{b2}+ J_{c1}^{++}+ J_{c2}^{+})]^{m1k1} \text{ on region } a_1\\ &= [A(J_{a1}^{--}+ J_{a2}^{-}+ J_{b1}+ J_{b2}+ J_{c1}^{++}+ J_{c2}^{+})]^{m1k1} \text{ on region } b_1\\ &= [A(+J_{a1}^{--}+ J_{a2}^{-}+ J_{b1}+ J_{b2}- J_{c1}^{--}- J_{c2}^{-})]^{m1k1} \text{ on region } c_1\end{aligned} \tag{3.3.80}$$

$$\begin{aligned}[A(J_{1abc}+J_{2abc})]^{m2k2} &= [A(-J_{a2}^{+}- J_{a1}^{++} + J_{b1}+ J_{b2}+ J_{c1}^{++}+ J_{c2}^{+})]^{m2k2} \text{ on region } a_2\\ &= [A(J_{a1}^{--}+ J_{a2}^{-}+ J_{b1}+ J_{b2}+ J_{c1}^{++}+ J_{c2}^{+})]^{m2k2} \text{ on region } b_2\\ &= [A(+J_{a1}^{--}+ J_{a2}^{-}+ J_{b1}+ J_{b2}- J_{c1}^{--}- J_{c2}^{-})]^{m2k2} \text{ on region } c_2\end{aligned} \tag{3.3.81}$$

The superscript in (3.3.80) and (3.3.81) denotes the evaluation at the centroid of T_{miki}.

J_{bi} is expressed as

$$J_{bi} = \frac{I_i\, l_{bni}}{2\, A_{bni}} \tag{3.3.82}$$

where A_{bni} is the area of T_{bni} and l_{bni} is a vector that is independent of position on T_{bni}. The definition of l_{bni} assures continuous current flow from strip a_i through the discontinuity region b_i to strip c_i. The magnetic vector potential due to J_{bi} in (3.3.80) and (3.3.81) is given by

$$A(J_{bi})^{miki}/I_i = \frac{\mu_o}{8\pi}\sum_{n_i=1}^{N_{Ni+1}} \frac{1}{A_{bni}}\, G(miki,nili) \tag{3.3.83}$$

Where G(mili,nili) is defined in (3.2.49). The vector potentials in (3.3.80) and (3.3.81) are evaluated in the Appendix.

Once the excess current distribution is solved for in (3.3.72) the excess inductance coefficients can be computed from (3.3.50)-(3.3.53).

3.4 Implementation

The algorithm was implemented in a Fortran program for the computation of the discontinuity parameters for single and coupled microstrip bend configurations. To maintain a high degree of flexibility, the computation is divided into two parts. Part one consists of a program which generates the structural information about the discontinuity and all other data, necessary for the complete characterization of the discretized geometry. The second part consists of a program that solves the electromagnetic boundary value problem which makes use of the data generated in part one. This allows one to perform modifications of the geometry without changing the electromagnetic code.

An alternative algorithm which makes use of an adaptive grid generation scheme was also implemented. The procedure was applied in the computation of the excess inductance of a right angle bend. After a description of the geometry and data structure both of the algorithms are described in the next section. However, the emphasis will remain on the two step algorithm which was found to be more efficient as compared to the adaptive procedure.

3.4.1 Grid Generation

Various algorithms on automatic grid generation are published in the literature [28–31]. Most of these algorithms are designed for application in conjunction with a finite element method. Due to the special treatment of the problem using the excess formulation, a customized triangulation of the discontinuity region is necessary. In order to minimize computing requirements it is desirable to generate a grid with non uniform elements such that the element size becomes smaller as the discontinuity region is approached. For the fixed grid geometry this was accomplished by applying a division scheme which makes use of a geometric series. The adaptive algorithm uses a local error dependent element size.

3.4.1.1 Datastructure. Let NN be the number of nodes on S, where S is the triangulated surface of the discontinuity and the truncated strips. The triangles on strip a are called T_i, i=1,2,...,NTA, the triangles on the corner region b are called T_i, i=NTA+1,NTA+2,...,NTB, and the triangles on strip c are called T_i, i=NTB+1,NTB+2,...,NTC. Let N be the number of interior nodes on S. An interior node of S is a node not on any edge of S. NLA are the number of nodes on line a, the line at $z = z_a$ where strip a connects to the corner region b. The number of nodes on line a is the same as the number of nodes on the line c, NLC where region b connects to strip c. If the nodes of S are numbered from 1 to NN, then the input variables X(I), Z(I) are, respectively, the x and z coordinates of the I^{th} node on S.

The node numbers of the vertices of the triangles on S enter the program by means of the input array NNT. The first, second, and third vertices of the J^{th} triangle are, respectively, the NNT(3*J-2)th node of S, the NNT(3*J-1)th node of S, and the NNT(3*)th node of S. Except for the (NLA-1) corner triangles attached to line a and the first (NLC-2) corner triangles attached to line c, the order of the vertices of the triangles is arbitrary. A triangle is said to be a corner triangle attached to line a if this triangle is on the corner region b and if one side of it is a segment of line a. A similar argument hold for a corner triangle attached to line c, the connection where the corner region attaches to strip c. The first and second vertices of each of the (NLA-1) corner triangles attached to line a must be on line a. Moreover, the x coordinate of the second vertex must be larger than that of the first vertex. The first and second vertices of each of the first (NLC-2) corner triangles attached to line c must be on line c. The z coordinate of the second vertex must be larger than that of the first vertex. The order of vertices stipulated in the previous sentences facilitates determination of the limits of integration and signs for various integrals.

The array NTT serves to identify the (NLA-1) corner triangles attached to line a and the first (NLC-2) corner triangles attached to line c. The I^{th} corner triangle attached to line a is the NTT(I)th triangle defined by the array of node numbers NNT. Here, I=1,2,...,NLA-1. The (I-NLA+1)th corner triangle attached to line c

is the NTT(I)th triangle defined by the array of node numbers NNT. Here, I=NLA, NLA+1, ... NB, where

$$NB = NLA + NLC - 3 \tag{3.4.1}$$

The arrays NJ, NTJ, NL1, and NL2 serve to define the expansion functions J_j in (3.2.39) and the NB corner currents J_{bj} in (3.2.52). The corner currents J_{bj} are written as J_j, j=N+1, N+2,...N+NB, where J_j is given by (3.2.52). The integer NJ(j) is the number of triangles covered by J_j. The n^{th} triangle covered by J_j is the NTJ(M)th triangle defined by the array of node numbers NNT where

$$M = n + \sum_{k=1}^{j-1} NJ(k) \quad \begin{matrix} , \; n = 1,2,\ldots,NJ(j) \\ , \; j = 1,2,\ldots,N+NB \end{matrix} \tag{3.4.2}$$

If j=1, the sum of k is to be omitted from (3.4.2). On the n^{th} triangle covered by it, J_j is given by (3.2.39)

$$J_j = \frac{\boldsymbol{l}_{jn}}{2\,A_{jn}} \quad \begin{matrix} , \; n = 1,2,\ldots,NJ(j) \\ , \; j = 1,2,\ldots,N+NB \end{matrix} \tag{3.4.3}$$

where A_{jn} is the area of this triangle; $\boldsymbol{l}_{jn}$ is the vector that extends from the NL1(M)th node of S to the NL2(M)th node of S where M is given by (3.4.2). The orientation of $\boldsymbol{l}_{jn}$ is such that all interior nodes on S are encircled in a counterclockwise manner. The array NVBA identifies those nodes on line a that fall on an edge of S. All nodes that fall on an edge of S are stored in an array NVBC for use in the algorithm for the automated recognition of varies identification vectors.

Now the objective is to automatically generate the triangle nodes NNT, the node coordinates X,Z, the identification array NTJ for triangles which encircle interior nodes on S, the node numbers NL1 and NL2 which guarantee the counterclockwise direction of l_{jn} with respect to the interior node j for triangle T_{jn}, the identification array NJ(j) which stores the number of triangles that encircle the interior nodes j, the identification array NTT which stores the corner triangles at line a. The current J_b as defined in (3.2.52) is stored such that all information necessary to characterize J_b is augmented to the arrays NL1, NL2, NJ, NTJ, which facilitates the programming structure.

3.4.1.2 Fixed Grid Structure. Figure 3–3 shows the general geometry of the discontinuity region with bend angle α and a chamfer coefficient CH. The chamfer is defined by the percentage change in length of the diagonal d=s+l, caused by cutting the edge of the corner.

Any chamfer and bend configuration is derived from a right angle bend with zero chamfer by applying a linear compression. Naturally, this technique leads to the refinement of areas with large current or charge density which equalizes the error distribution on the strip surface S and therefore allows for an efficient evaluation of excess parameters. Consider the horizontal portion of the symmetric bend. In the x direction a uniform spacing is used. In the z direction a subdivision scheme is applied which causes an increase in the grid spacing away from the corner region by means of a geometric series. An example of a discretized rectangular corner with all relevant

quantities which have been defined in this paragraph is given in the Appendix.

If a geometry with variable bend angle α and chamfer ratio CH is to be considered only the coordinates of the nodes of the triangulated surface S need to be changed. All other quantities are the same as for the rectangular corner with zero chamfer, which is due to the fact that all quantities are derived in terms of node numbers rather than coordinates.

A geometry with bend angle α is derived from a geometry with bend angle $\alpha_0 = 90°$ by a linear transformation of coordinates in the discontinuity region. Now when the coordinates for the desired bend angle are generated, further adjustments are made to account for the specified chamfer ratio CH. This was done by a linear compression of the coordinates in the bend region b. A z-dependent stretch factor is defined which acts on the nodes in the bend region b with respect to suitably defined reference nodes.

Sample grid geometries are shown in Figure 3-4. The initial rectangular bend with zero chamfer is depicted in Figure 3-4a. Derived from this geometry is the zero chamfer bend with bend angle α as shown in Figure 3-4b from which a different chamfer geometry can be formed as is demonstrated in Figure 3-4c.

3.4.1.3 Dynamic Grid Structure. In the previous section an algorithm was described which generates the discontinuity geometry with all relevant information necessary for the solution of the boundary value problem which is solved in a subsequent step.

In the adaptive algorithm [24] the grid is established iteratively. Starting with an initial set of surface current elements as is shown in Figure 3-5, the excess currents are evaluated by enforcing the normal magnetic field at the interior nodes of the defined triangular grid to be zero. In the next step, the local element error is found by computing the residual flux through each triangular element. Those elements with a flux density greater than some threshold are refined by introducing an additional node at their center point thereby forcing the local error to zero. An optimum triangular grid is maintained in the sense of maximizing the minimum interior angle of each triangle [32] with the constraint of maintaining the border regions of areas a, b and c. This can be accomplished by applying the circle criterion to neighboring triangles as is illustrated in Figure 3-6. Consider two triangles A and B. Let a circle pass through three of the vertices of the quadrilateral which is formed by the triangles A and B. If the fourth vertex of the quadrilateral is interior to the circle, swap the common triangle side. If the fourth vertex is exterior to the circle do not swap the common triangle side. If the fourth vertex is on the circle either triangulation can be used. Suppose node C is introduced for refinement purpose, then the optimizing scheme can be summarized as follows:

1. delete the triangle that contains node C and create three new triangles.
2. consider successively each new created triangle and all its neighbors and apply the circle test to their common side if it is not a boundary of region a, b or c.

3. repeat step two to all new created triangles and their neighbors until no diagonal swap is performed.

Triangles for which one side falls on a border region require special treatment. If the side on the border region is the maximum length of the particular triangle then step one is modified as follows: delete the triangle that contains node C and create two new triangles by uniformly dividing the side which falls on the border line. Figure 3-7 shows the final grid for the excess current of a rectangular microstrip discontinuity. Note that the deviation of the assumed current from the actual current distribution is largest in the corner region.

3.4.1.4 Comparison. For the adaptive algorithm the number of elements required to obtain a converged solution is about a factor of five larger as compared to the fixed grid generation which is due to the fact that an optimum element size is maintained throughout the discontinuity region. However, the moment method does not require the elements to be of optimum shape in the sense as defined in section 3.4.1.3. This observation is supported by Figure 3-8 which demonstrates the convergence of the excess inductance of a right angle bend with respect to the number of subsections on the microstrip line in z direction. A microstrip line was assumed with a W/H ratio of 2, H = 0.5m and region a was chosen to be of length 5H. Ten subsections were used in the x direction on region a. The solution can be considered as converged for 8 subsections which yields a considerable reduction of the matrix size as compared to the case where a uniform grid size

were applied which would require 50 subsection in the z direction on region a.

Since the adaptive procedure makes use of an iterative scheme a number of boundary value problems have to be solved subsequently, each step consisting of the evaluation of the excess current and the determination of the residual error on each triangular element. Computation times for the adaptive algorithm are about a factor of 12 higher as compared to the fixed grid solution which requires only the solution of one boundary value problem.

All results are generated by using the fixed grid generator due to the superior computation times and storage requirements. However for general geometries where a geometric series is not straight forward to apply the adaptive algorithm can be a competitive alternative.

3.5 Numerical Results

3.5.1 Single Bends

As an initial confidence test results for a symmetric right angled bend are compared to previously published data for stripline W/H ratios in the range of 0.5 to 2. A relative dielectric constant of 12.9 was assumed for all cases.

Results for the excess capacitance obtained from this method are compared to simulated results from [8,19] and to experimental data [36] in Figure 3-9. The corner capacitance is normalized with respect to the capacitance per unit length of the microstrip line and the substrate height. The quasi-static simulations agree within less than 1% for W/H ratios between 0.8 to 2. The excess capacitance derived

from design equations in [36] deviates about 10% from the quasi-static results. The relatively large difference can be explained by considering the technique that was used to extract the static parameter from measurements. This will be analyzed in detail for the inductive case.

A comparison of excess inductance is shown in Figure 3-10. Unlike the capacitive case major discrepancies prevail for the inductive results obtained from different methods [13,17,36]. Kirschning [49] attributes the differences between the results obtained from [13] and [36] to the fact that [13] is obtained from static calculations whereas [36] is derived from statistical averaging from measurement data in the frequency range of 2-14 GHz. In addition, he observed a larger sensitivity of the error function in the identification process for the capacitance. The minimum of the error function in [49] depends on the selection of the p parameter. Only for the limiting case of a vanishing error function the minimum is independent of the p parameter. Results therefore depend on the choice of p.

Results obtained from the present method and [13,17] are all derived from the boundary value problem for static conditions. However, the present method makes use of various analytical manipulations in order to increase the accuracy of the method. The decomposition procedure for currents and the application of Stokes' Theorem leads to the evaluation of integrals over source free regions on the striplines. In addition, the partial inductance of a semiinfinite line

$$\frac{1}{I^2} \int A(J^+)\ J^- \qquad (3.5.1)$$

needs to be incorporated in the excess formulation if the striplines are assumed to extend to infinity. This is due to the definition of inductance which always has to be associated with a closed path. This was done in the analytical development in section 3. In previous publications, e.g. [13], the associated expression (3.5.1) was evaluated over a finite region. Since the magnetic vector potential $A(J^+)$ decays logarithmically, the upper limit for the integration in (3.5.1) has to be chosen rather large which results in excessive computation times. To demonstrate the behavior of $A(J^+)$ for various W/H ratios, the vector potential $A(J^+)$ at the center of a microstrip due to a unit current J^+ on a strip of width W = 1m is plotted in Figure 3-11. The current direction and the strip geometry are illustrated in the insert of Figure 3-11. Note, for small W/H ratios, the decay of $A(J^+)$ is rather slow which leads to unacceptable upper integration limits for the numerical evaluation of the integration in (3.5.1). An analytical expression was developed in this work (Appendix) to accurately incorporate the contribution of (3.5.1) to the excess inductance. To demonstrate the effect of truncating the integration in (3.5.1) the excess inductance of the bend is plotted for two cases in Figure 3-12 for a strip with W/H = 2. Case 1 denotes the evaluation of the excess inductance where the integration in (3.5.1) is performed to infinity using the analytical formula. Case 2 denotes the evaluation of the excess inductance where the integration in (3.5.1) is performed to an upper limit -z, where -z denotes the distance away from the junction plane T_1. Excess currents are assumed to have decayed to a negligible value at the distance -z away from T_1. For case 1 the convergence of

the excess inductance is reached at $-z/W \approx 5$. For case 2, a rather slow convergence behavior is observed which again, is due to the inadequate truncation of (3.5.1) and leads to higher values for the excess inductance.

Results for variable bend angle and chamfer geometries are illustrated for W/H ratios of 0.5, 1 and 2 in Figures 3-13 and 3-14 for the capacitance and inductance computations respectively. Similar investigations have been done previously by Anders and Arndt [20] who used line currents in the moment method which corresponds to a wire grid modelling approach whereas surface currents are used in this work. Glisson and Wilton [58] conclude that the wire grid modelling technique is "not well suited for calculating near field and surface quantities such as surface current ..." which was a motivation to use surface currents. An increase in chamfer ratio and a decrease in the bend angle lead to a reduction of the normalized excess capacitance which is due to the reduction of the area in the discontinuity region. Contrary to capacitance computations, an increase in chamfer ratio causes an increase in excess inductance which is due to current crowding effects in the corner region. Results for the excess inductance obtained from the present method agree within 10% to those of Arndt and Anders for W/H ratios of 2 (Fig. 3-14a). However, for smaller W/H ratios significantly lower results were obtained which could be due to the different modelling of the surface currents. Another source of disagreement could be related to the incorporation of the partial

inductance of the infinite line which has been discussed at the beginning of this section.

3.5.2 Coupled Bends

The computer programs for the coupled bend analysis were tested by the limiting case of infinite separation of the microstrip lines. All values for the inductance coefficients and capacitance coefficients as defined in sections 3.3.2 and 3.3.3 are normalized with respect to their corresponding quantities of two uniform parallel coupled microstrip lines and the substrate height. The equivalent circuit of coupled striplines is shown in Figure 3-15 where the circuit parameters are related to the capacitance and inductance coefficients by

$$C_w = C_{11ew} - C_{12ew}$$

$$C_m = -C_{12ew}$$

$$L_w = L_{11w}$$

$$L_m = L_{12w} \qquad (3.5.2)$$

In all illustrated cases, the separation of the lines is equal to the strip width. A dielectric constant of 12.9 was assumed for all simulations.

In Figure 3-16 the dependence of the capacitance coefficient versus bend angle α is shown. Note that the normalized coupling coefficient, c_{12e}, behaves in the same manner as the coefficients c_{11e} and c_{22e}. A decrease in the bend angle leads to a reduction of the

bend area between planes T_1 and T_2 in Figure 3-3b and, therefore, results in a reduction of excess capacitance.

Consider Figure 3-17 for the variation of the excess inductance versus bend angle. The normalized inductance L_{22e} and L_{12e} show a similar dependency versus bend angle. For a bend angle $\alpha = 0$ the corner is eliminated and the excess inductances reduce to 0. For a bend angle of 90° the current direction on the striplines that connect to the corner at planes T_1 and T_2 (Figure 3-3b) form an angle of 90° which results in a reduction of the partial inductance. For bend angles between 0° and 90° the reactance [59] between the currents on the striplines that connect to the corner increases which results in higher inductance values. Therefore a maximum of inductance can be observed between 0° and 90° bend angles. The situation is different for L_{11e} which is dominated by the partial inductance of the transmission line sections between the planes T_1–T_3 and T_4–T_2. The length of these sections increase with increasing bend angle which leads to an increase of L_{11e} versus bend angle.

3.6 Conclusion

Microstrip bends have been analyzed for single and coupled configurations. Compared to the coupling parameter of uniform coupled strip lines, the coupling parameter of the studied microstrip corner geometries are of the same magnitude relative to the substrate height. This demonstrates the significance of coupled discontinuity effects.

From the discussion in section 3.3 it is clear that the assumption of infinite extension of the microstrip lines is critical for the

exact determination of the excess inductance. However, the practical relevance of this issue is questionable since the assumptions are hardly ever met for various circuit configurations. Therefore the quasi-static results obtained here and elsewhere are to be considered as an approximation. The validity of their application depends on the circuit environment.

The second part of this work is concerned with a full wave treatment of shielded structures where the geometry of the investigated discontinuities are well defined.

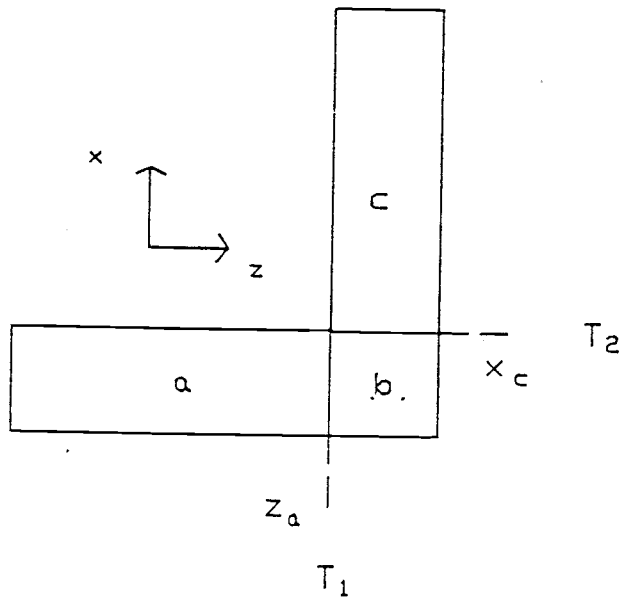

(a)

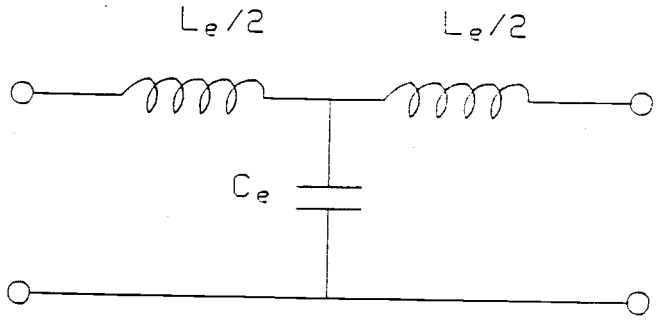

(b)

Figure 3–1. Microstrip right angle bend: (a) subdivided into regions for excess formulation; (b) equivalent circuit.

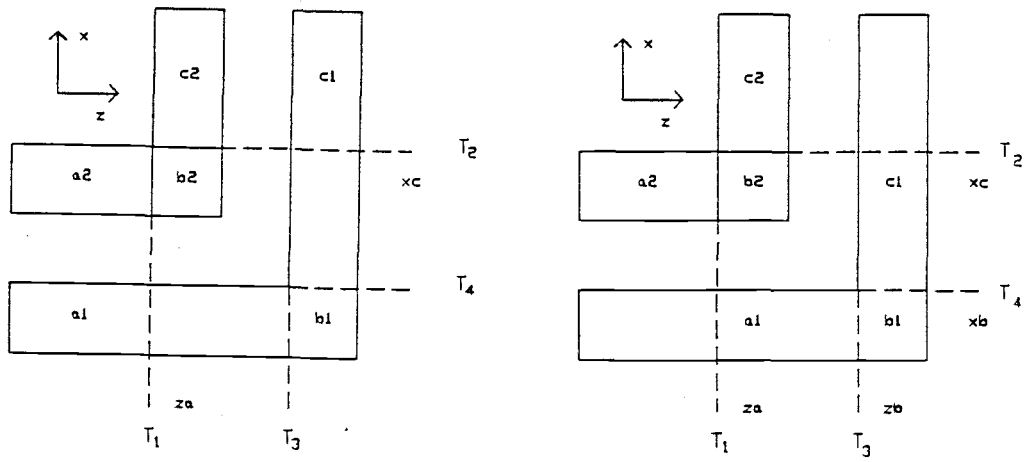

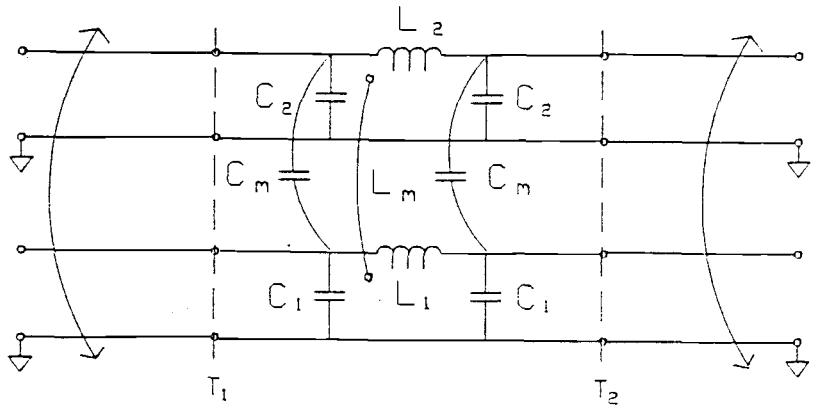

Figure 3-2. Coupled microstrip right angle beds: (a) subdivided into regions for capacitance computations; (b) subdivided into regions for inductance computations; (c) equivalent circuit.

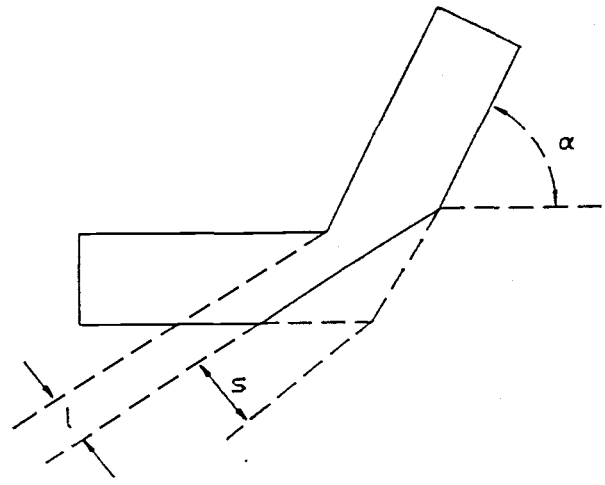

(a)

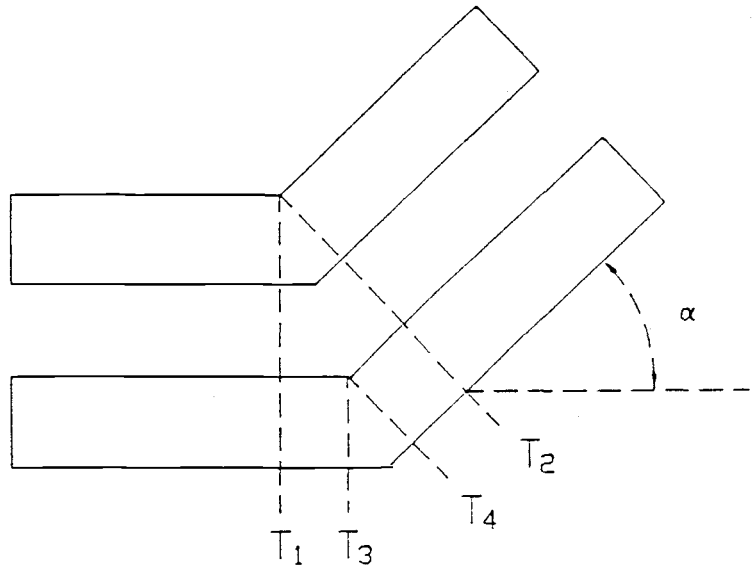

(b)

Figure 3-3. Modified bend geometry: (a) single bend with variable bend angle and chamfer; (b) coupled bends with variable bend angle.

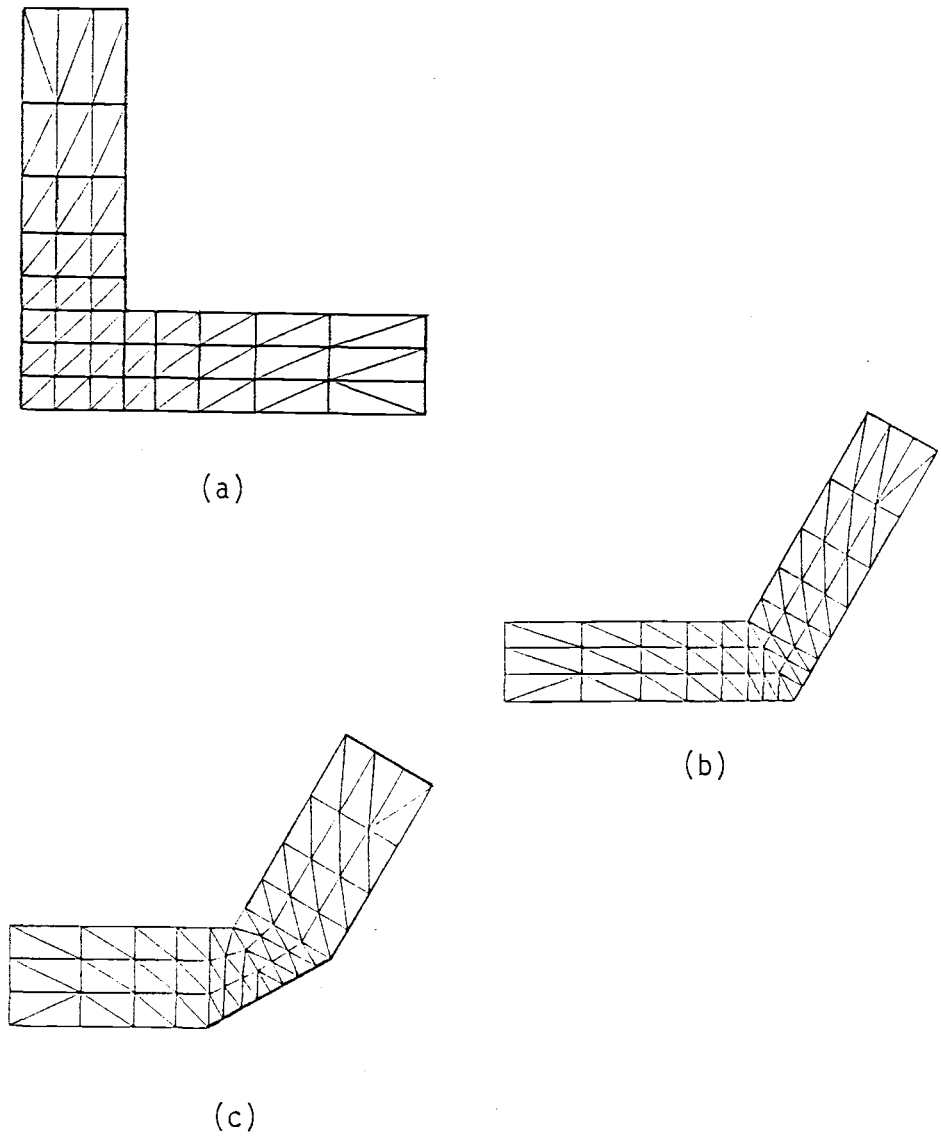

Figure 3–4. Derivation of variable bend angle and chamfer from right angle bend with 0% chamfer: (a) right angle bend; (b) variable bend angle derived from (a) by linear mapping; (c) variable chamfer derived from (b) by linear mapping.

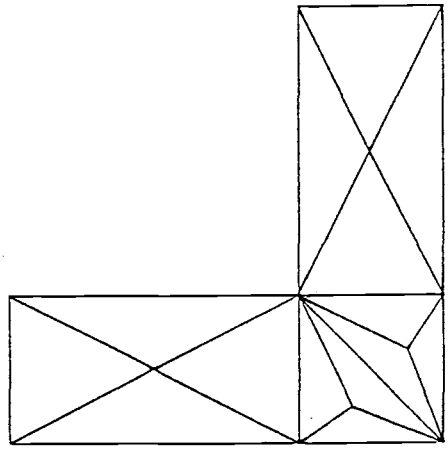

Figure 3-5. Initial grid for adaptive grid refinement.

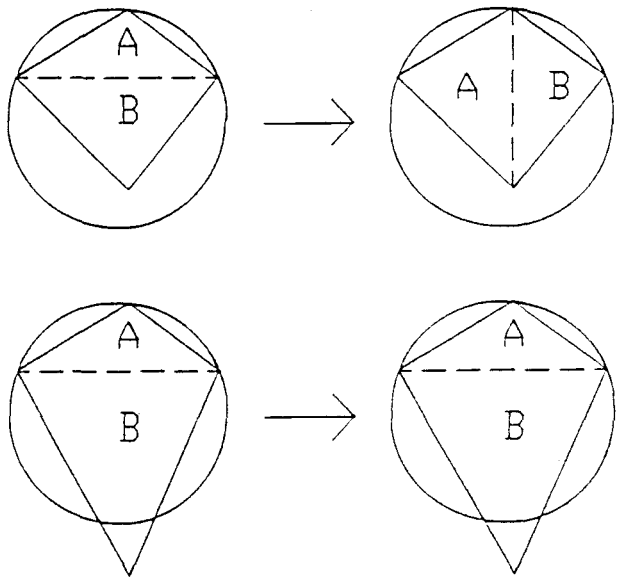

Figure 3-6. Circle criterion assures optimum triangle shape.

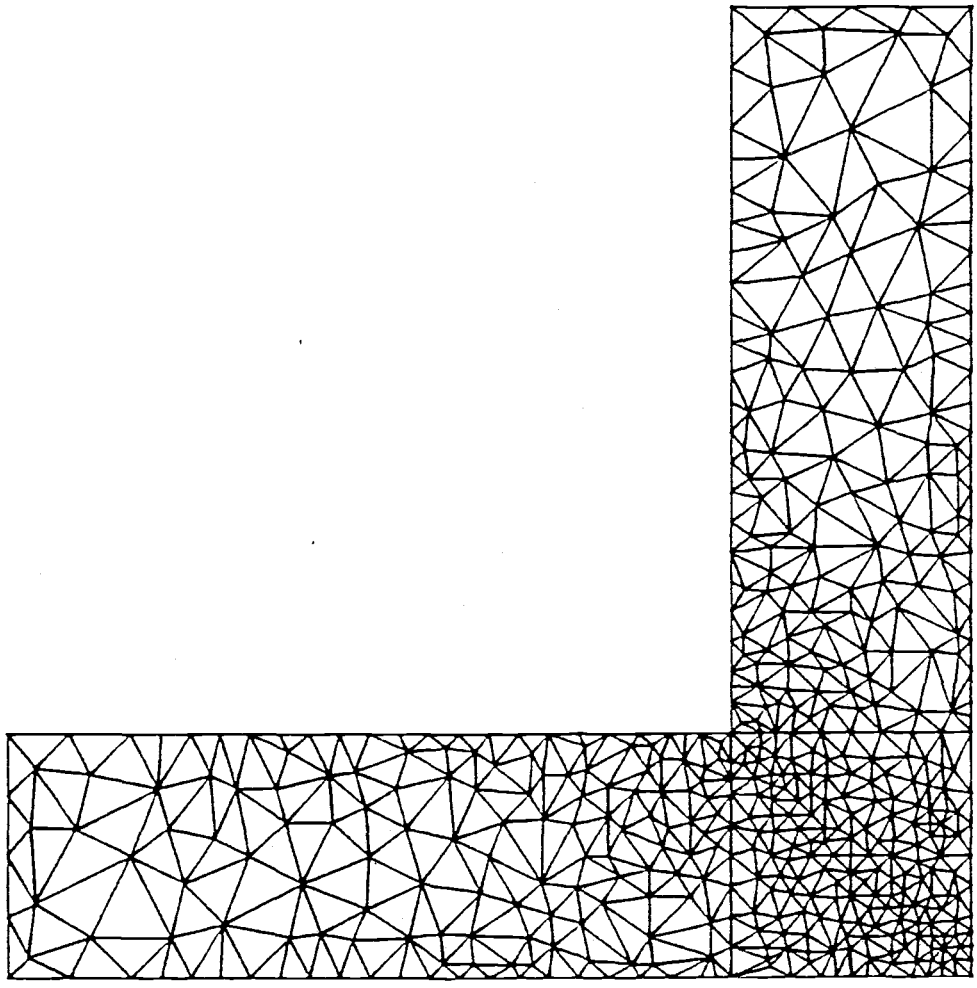

Figure 3-7. Optimized grid structure.

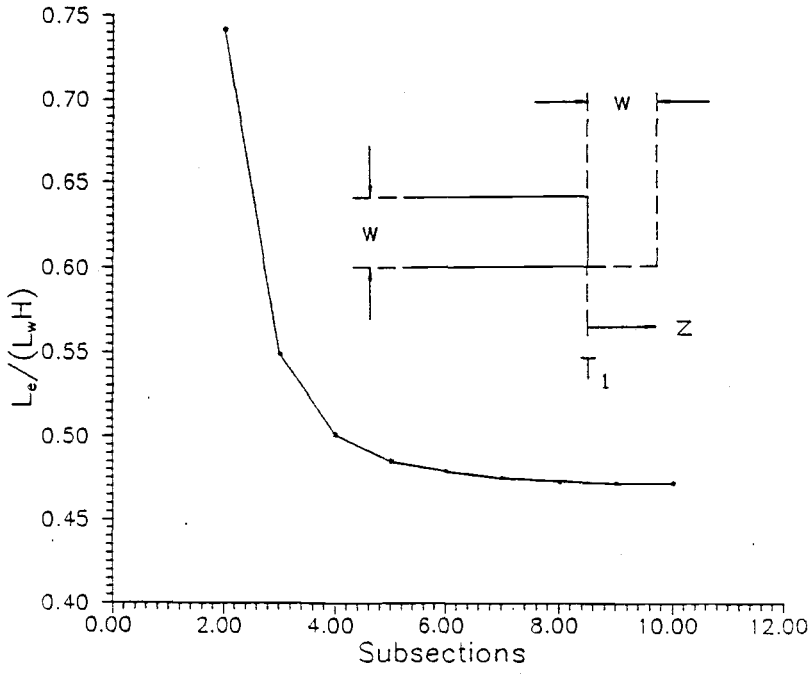

Figure 3-8. Convergence of excess inductance versus number of subsections in z direction on stripline (W/H = 2).

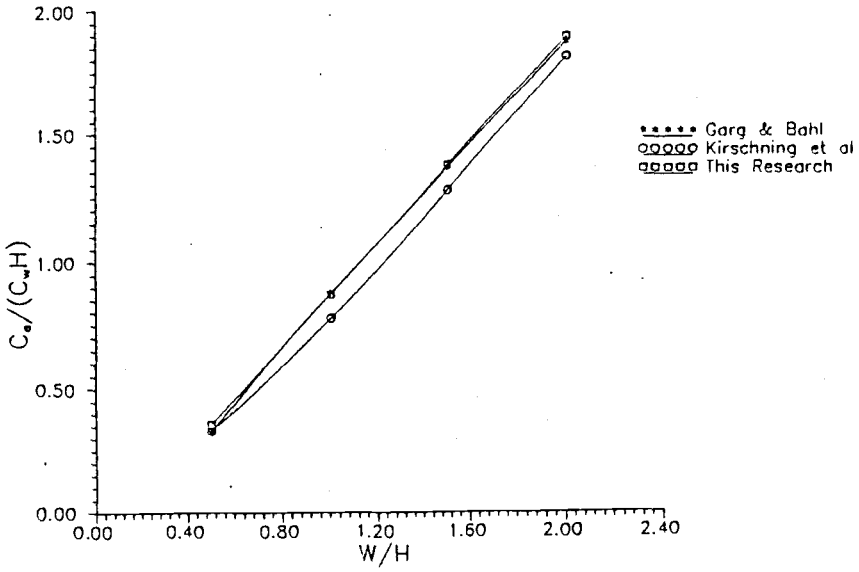

Figure 3-9. Excess capacitance of right angle bend (ϵ_r = 12.9).

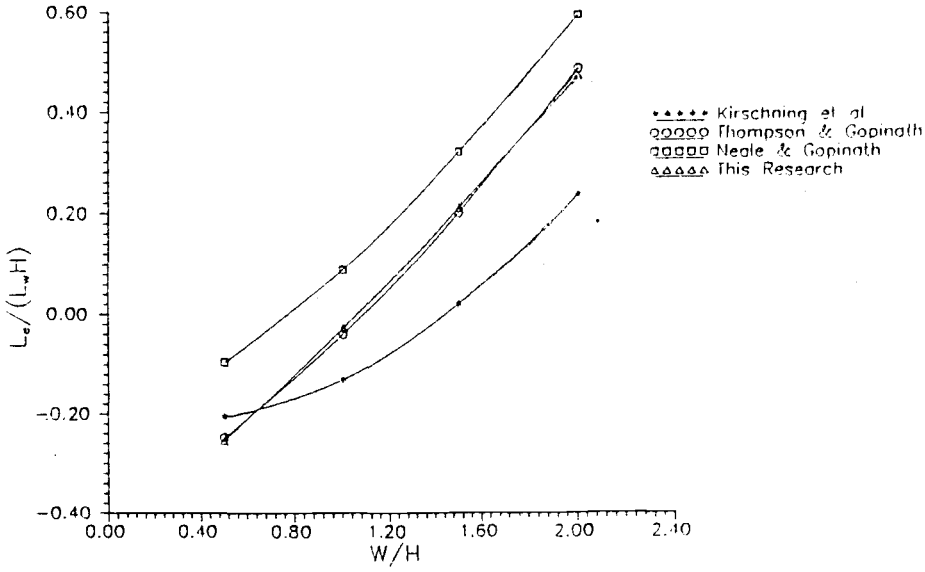

Figure 3-10. Excess inductance of right angle bend.

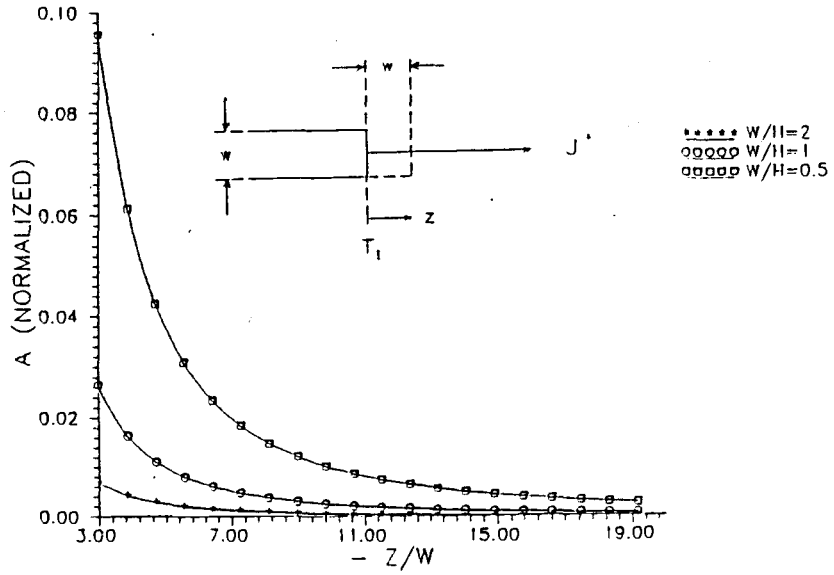

Figure 3-11. Vector potential due to semi-infinite current sheet (W/H = 2).

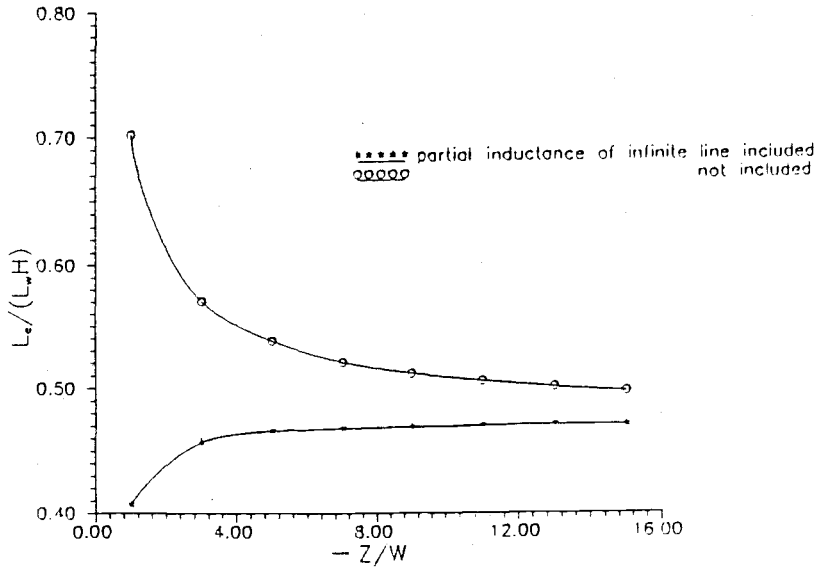

Figure 3-12. Convergence of excess inductance for case 1 and case 2.

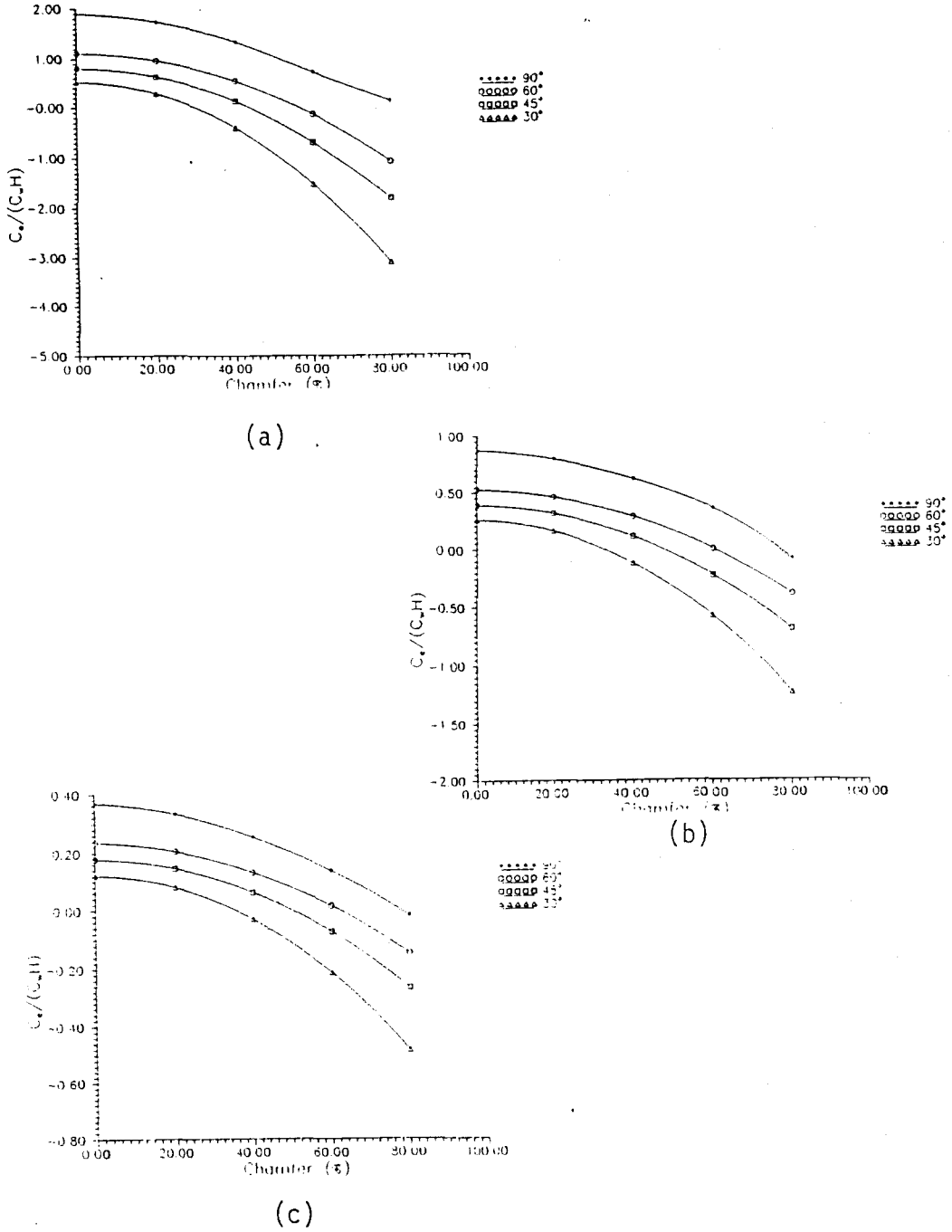

Figure 3–13. Excess capacitance versus chamfer for different bend angles (ϵ_r = 12.9): (a) W/H = 2; (b) W/H = 1; (c) W/H = 0.5.

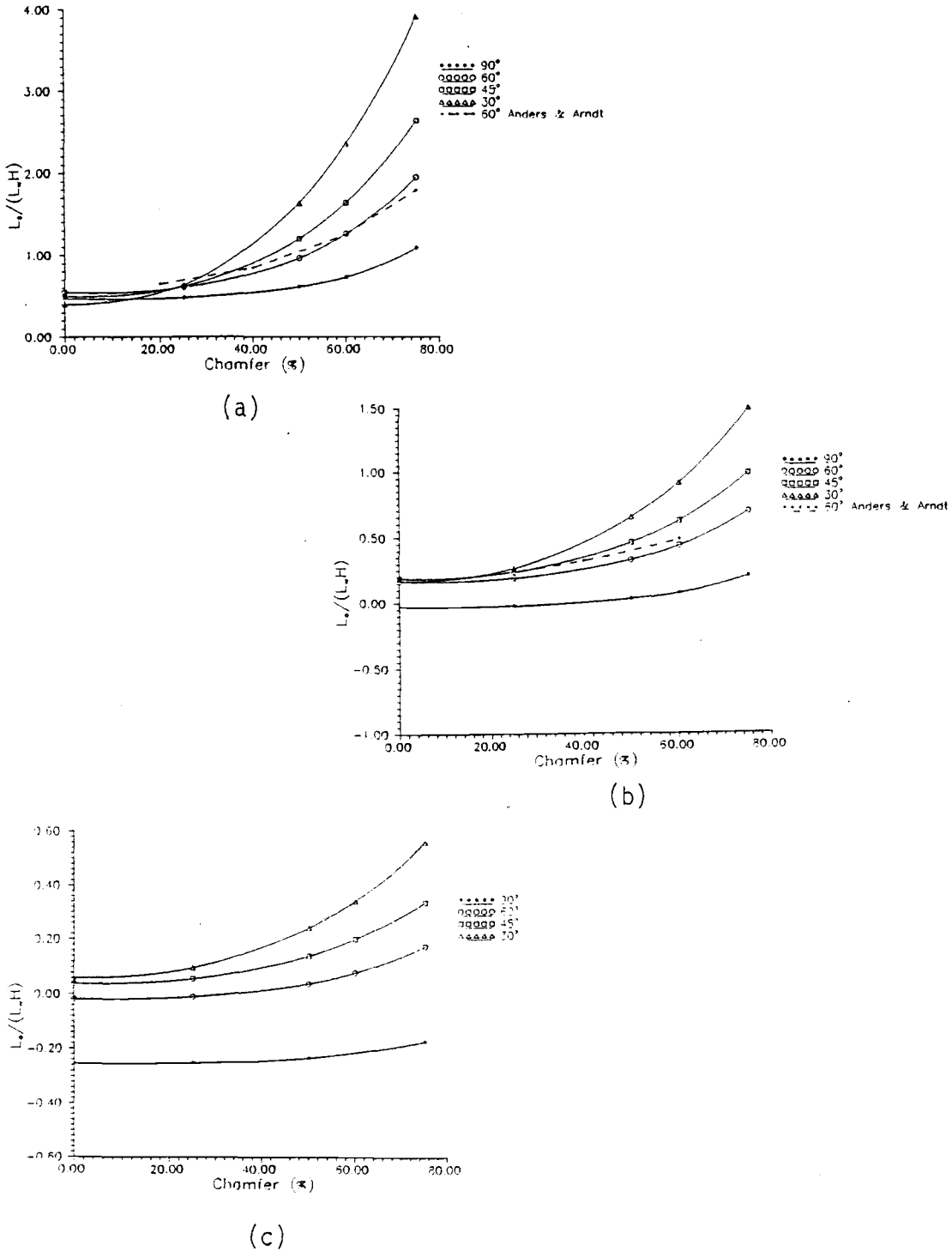

Figure 3-14. Excess inductance versus chamfer for different bend angles: (a) W/H = 2; (b) W/H = 1; (c) W/H = 0.5.

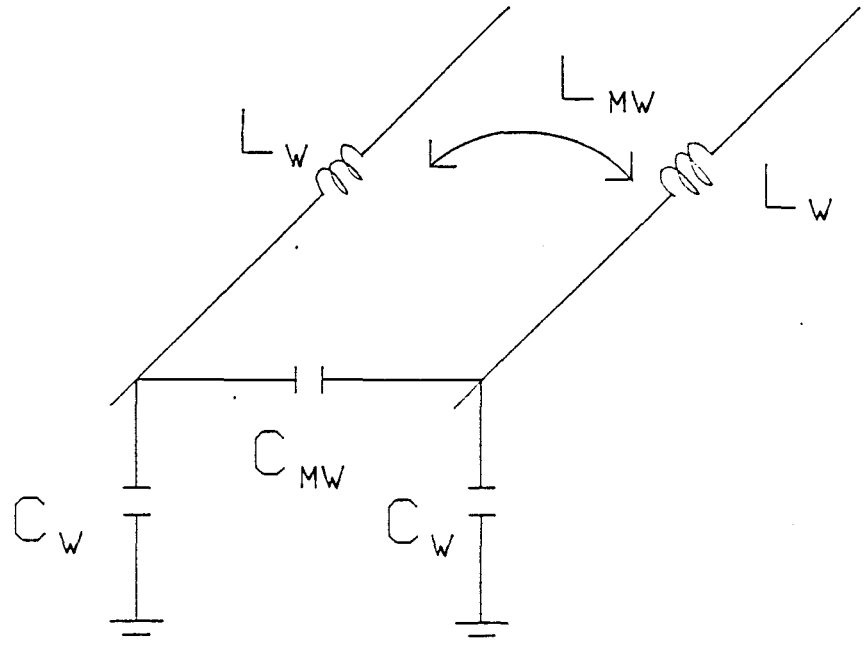

Figure 3-15. Equivalent circuit for uniformly coupled microstrip lines.

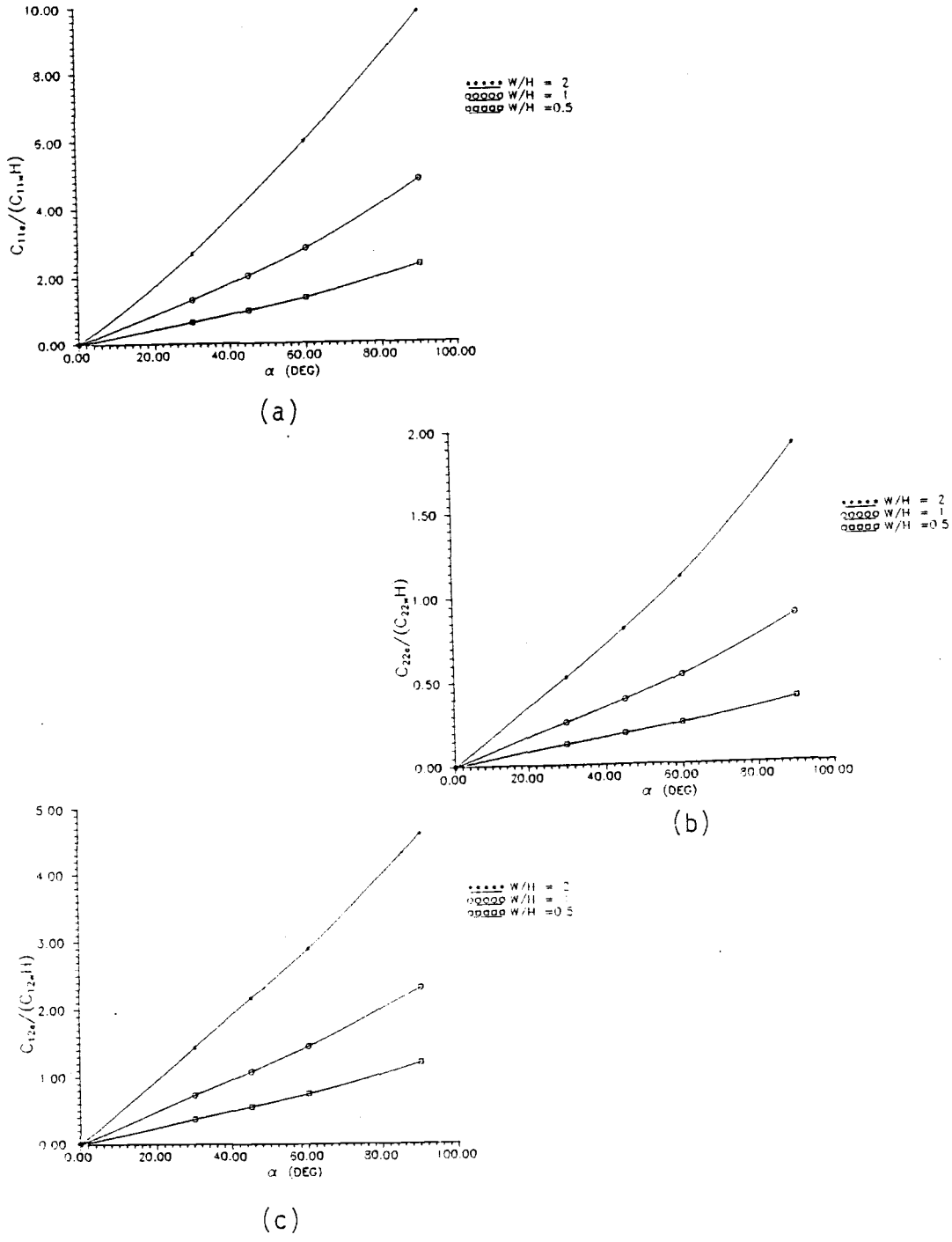

Figure 3-16. Normalized coefficients for the excess capacitance matrix versus bend angle for different W/H ratios (ϵ_r = 12.9): (a) C_{11e}; (b) C_{22e}; (c) C_{12e}.

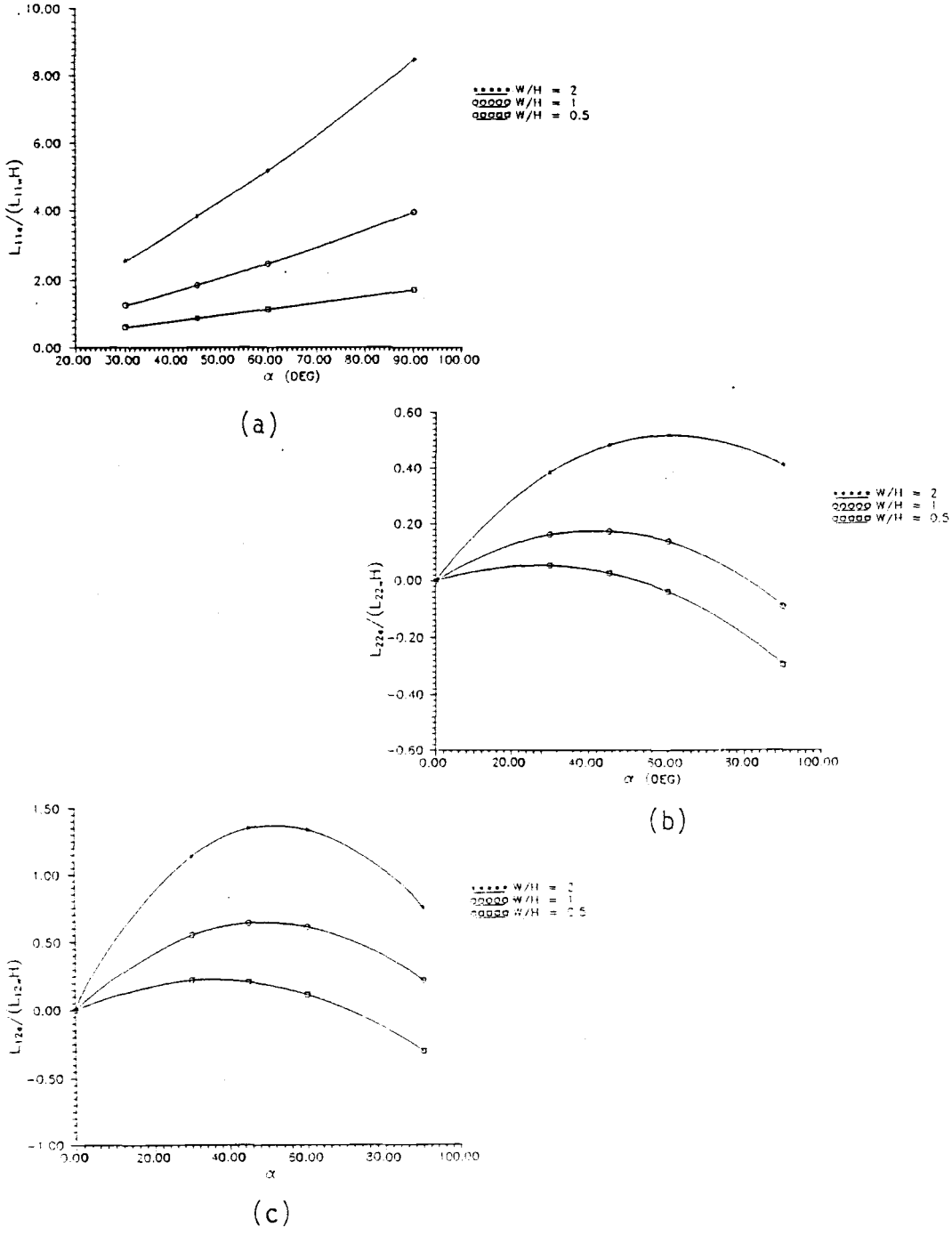

Figure 3-17. Normalized coefficients for the excess inductance matrix versus bend angle for different W/H ratios: (a) L_{11e}; (b) L_{22e}; (c) L_{12e}.

4. FULL WAVE ANALYSIS

4.1 Introduction

A method for calculating the dynamic properties of various discontinuities was suggested by Wolff et al. [25]. Their analysis uses a waveguide model and a field matching technique to determine scattering parameters of the discontinuity region. Chu and Itoh [45] replace the mode matching procedure in [25] by a modified residue calculus technique to describe a symmetrical T-junction. All of the above techniques use an equivalent waveguide model and therefore do not account for surface waves and radiation. These methods are not suitable for coupling considerations since the discontinuity region is transformed into an equivalent closed structure. The waveguide model has its limitations for applications in the higher frequency range. In addition, inaccuracies in the modeling of phase information have been reported [50]. Katehi and Alexopoulos [46] calculate equivalent circuit parameters by applying Pocklington's integral equation and solve it for the current distribution on the strip surface by using the moment method. Currents are expanded into piecewise sinusoidal functions and are assumed to be unidirectional, therefore limiting the analysis to striplines small in width. A gap generator is used as excitation mechanism. Jackson and Pozar [47] use a similar formulation as Katehi and Alexopoulos except that the excitation problem is overcome by assuming lines that extend to infinity away from the discontinuity. A current distribution that corresponds to the respective distribution on an infinite line is assumed to be incident on the

junction. Additional piecewise sinusoids are introduced to model the current distribution in the discontinuity region. Incident, reflected and transmitted amplitudes of the current are then used to calculate scattering parameters.

A resonance technique has been developed by Jansen [52] which has been used by Koster [51] for the characterization of strip- and slot-type MICs. The scattering matrix of the discontinuity is found by the evaluation of wave amplitudes of incident and reflected waves. In contrast to the previous two methods, a two-dimensional current distribution is assumed. A planar waveguide mode is employed as excitation mechanism. The incident current is truncated sufficiently far away from the discontinuity and global expansion functions are used in the junction region. The resonance technique has the advantage of providing phase information which is stationary with respect to the current density and field distribution. However, a simulated resonance experiment requires more intensive computations as compared to a deterministic approach. Sorrentino and Itoh developed a transverse resonance analysis for finline discontinuities [65] which has been extended to characterize crossing striplines by Uwano et al. [66]. The discontinuity structure with transmission line sections extending away from the discontinuity is embedded in a rectangular box. A resonance condition is formulated in terms of the network impedance matrix of the discontinuity region and the shorted transmission line impedances. For certain types of resonances (even,odd) the impedance matrix elements are expressed in terms of the transmission line input impedances, rendering enough equations to characterize the discontinu-

ity. Elements of an equivalent circuit are then derived from the impedance matrix of the discontinuity. A field analysis is formulated in terms of the eigenmodes of the box to find resonance conditions, e.g. transmission line lengths and resonant frequencies. In the Galerkin's procedure [60], two-dimensional sinusoidal currents with an edge term are applied to compute the current distribution on the striplines. Itoh [42] makes use of the spectral domain formulation to analyze microstrip resonators in a rectangular shield which lead to the dynamic characterization of open ended microstrip lines. Schmidt [64] and Chang [44] use a similar approach for the analysis of discontinuities. They describe the electromagnetic field on either side of the step discontinuity by an expansion in terms of shielded microstrip modes and satisfy the continuity of the transverse field at the step by using a mode-matching technique. The formulation in both cases is that of an excitation problem for the fundamental microstrip mode with all the higher order modes match terminated at infinity. Schmidt notes that the scattering parameter magnitudes behave less critically than the phase angles. Koster [51] overcomes the numerically sensitive phase problem by employing the resonance technique. Rautio and Harrington [62,63] describe a time harmonic analysis for planar circuit structures. Their analysis is a real space implementation of the previously developed spectral domain approach by Jansen [52,53]. Rautio employs two dimensional roof top functions as expansions in the moment procedure which makes his method very flexible. These functions have first been introduced by Glisson and Wilton [58] and have also been applied recently by Jackson [48], Skrivervik and Mosig [72].

Cendes and Lee [43] apply an adaptive algorithm in conjunction with a transfinite element method to analyze a T-junction. The problem region is divided into two parts, an interior region of finite extent and an exterior region that is homogeneous and unbounded. Within the inner region finite element basis functions are used to approximate the fields, in the exterior region analytical solutions of the Helmholtz equation provide a basis set for the field. Both sets of basis functions are employed in a variational procedure. Imposing continuity along the two regions gives a symmetric matrix equation that is solved for the fields. Field solutions are first calculated at two frequencies. These two solutions are then used as basis functions to generate a crude spectral response curve throughout the region of interest. The system is then solved again at the frequency that gave the maximal residual error on the last pass. The method of lines has been used by Worm and Pregla [74,75] to characterize 3D structures using a resonant method. A deterministic approach with the method of lines technique has been presented recently by Chen and Gao [76]. Jansen [69] comments that the method of lines as described in [74] "is not well suited to treat energy transport phenomena involving parasitic surface waves .. due to the difficulty of extracting mode related quantities from a mixed-mode field". Wertgen and Jansen propose a spectral iterative technique for the full wave 3D analysis of (M)MIC structures [67]. Fast fourier transforms are applied for the summation scheme of Dirac-type current distributions. The main advantage of such a technique is the reduced storage requirement as compared to moment method formulations. Unfortunately, the conver-

gence of the spectral iterative technique is nonuniform and can be rather slow for complex structures which can result in inferior performance as compared to moment method techniques. Dunleavy and Katehi [55,56,57] use unidirectional sinusoidal basis functions to analyze open end and various filter structures in a shielded box. Skrivervik and Mosig [72] make use of a previously developed mixed potential integral equation to characterize microstrip discontinuities in an open environment. Discontinuity parameters are extracted by using a generalized chain matrix formulation which is a straight forward technique to overcome the de-embedding problem. Harokopus and Katehi [73] extend the method developed in [46] to incorporate 2D basis functions which allows for the analysis of a wider class of structures. Jansen and Wertgen [69] presented a modular source type 3D analysis for general discontinuities in (M)MICs. The problem geometry is subdivided in a modular fashion. Suitable current expansions are then associated with each module. Amplitudes of incident and reflected waves are determined from the standing wave pattern on transmission line regions.

The simulation of passive (M)MIC structures can be classified into three categories, namely open, shielded and partly shielded configurations. Each shielding type requires a different numerical treatment. Efficient computational methods have been derived for the open [54] and partly shielded structures [70]. However, the shielded configuration still requires intensive computational treatment. The insufficient development of full wave simulators which accurately

incorporate housing effects has been pointed out by Jansen and Wiemer recently [71].

In this work a new technique is introduced which allows an efficient numerical treatment of the shielded circuit structure that leads to reasonable computation times for the analysis of 3D microstrip structures for the case when 2D locally defined surface currents are employed in the moment method. The analysis is based on previous work by Jansen [52], Koster [51], Rautio and Harrington [62,63].

4.2 Numerical Formulation

4.2.1 Green's Function

The derivation of Green's function for the boxed structure as shown in Figure 4-1 is summarized in the following. Notations are chosen to be similar as in [51]. The source free media consists of three homogeneous, isotropic dielectric layers and is bounded by a box of perfectly conducting metal. Each layer r (r=1,2,3) of thickness H_r is characterized by its relative dielectric constant ϵ_r. The box extends from x = 0 to x = a, y = 0 to y = b with bottom and cover plates at z = 0 and z = c.

The fields in each layer satisfy Maxwell's equations in the form

$$-\nabla \times \mathbf{E} = j\omega\mu_0 \mathbf{H} , \qquad \nabla\cdot\mathbf{H} = 0 \tag{4.2.1}$$

$$\nabla \times \mathbf{H} = j\omega\epsilon_0\epsilon_r \mathbf{E} , \qquad \nabla\cdot\mathbf{E} = 0 \tag{4.2.2}$$

Due to the vanishing divergence of **E** and **H**, the fields can be expressed in terms of magnetic vector potential **A** and electric vector potential F

$$\mathbf{E} = -\nabla \times \mathbf{F} - j\omega\mu_0 \mathbf{A} + \frac{1}{j\omega\epsilon_0\epsilon_r} \nabla(\nabla\cdot\mathbf{A}) \tag{4.2.3}$$

$$\mathbf{H} = \nabla \times \mathbf{A} - j\omega\epsilon_0\epsilon_r\mathbf{F} + \frac{1}{j\omega\mu_0} \nabla(\nabla\cdot\mathbf{F}) \tag{4.2.4}$$

Arbitrary fields in a homogeneous source free region can be expressed as the sum of a TM (to z) and a TE (to z) field. Choosing F = 0 and A = $(0,0,\phi)$ or F = $(0,0,\psi)$ and A = 0 uniquely characterizes TM or TE fields, respectively. The scalar potentials ϕ and ψ are solutions to the Helmholtz equation.

Once the scaler potentials are known the field quantities are derived from

$$\mathbf{E} = \left(\frac{1}{j\omega\epsilon_0\epsilon_r} \frac{d^2\phi}{dxdz} - \frac{d\psi}{dy} , \frac{1}{j\omega\epsilon_0\epsilon_r} \frac{d^2\phi}{dydz} + \frac{d\psi}{dx} , \frac{1}{j\omega\epsilon_0\epsilon_r} \left[\frac{d^2}{dz^2} + k^2 \right] \phi \right) \tag{4.2.5}$$

$$\mathbf{H} = \left(\frac{1}{j\omega\mu_0} \frac{d^2\psi}{dxdz} + \frac{d\phi}{dy} , \frac{1}{j\omega\mu_0} \frac{d^2\psi}{dydz} - \frac{d\phi}{dx} , \frac{1}{j\omega\mu_0} \left[\frac{d^2}{dz^2} + k^2 \right] \psi \right) \tag{4.2.6}$$

In the solution process for the scalar potentials ϕ and ψ, k is defined as

$$k^2 = k_x^2 + k_y^2 + k_z^2 \tag{4.2.7}$$

$$k^2 = \omega^2\epsilon_0\epsilon_r \tag{4.2.8}$$

After enforcing the boundary conditions on the perfect conduction wall and the interfaces, the field quantities in the interface plane of the metallization layer are found. Then the currents on the metallization are related to the tangential magnetic field on the metal in region 2

and 3. Electric field and surface currents on the interface between regions 2 and 3 are

$$E_x = \sum_m \sum_n (-k_{xm}\, p_{mn1} + k_{yn}\, p_{mn2}) \cos k_{xm}x \sin k_{yn}y$$

$$E_y = \sum_m \sum_n (-k_{yn}\, p_{mn1} - k_{xm}\, p_{mn2}) \sin k_{xm}x \cos k_{yn}y \qquad (4.2.9)$$

$$J_x = \sum_m \sum_n (-k_{xm}\, p_{mn3} - k_{yn}\, p_{mn4}) \cos k_{xm}x \sin k_{yn}y$$

$$J_y = \sum_m \sum_n (-k_{yn}\, p_{mn3} + k_{xm}\, p_{mn4}) \sin k_{xm}x \cos k_{yn}y \qquad (4.2.10)$$

The terms in brackets reflect the respective spectral representations of the components on the left hand side. Making use of the orthogonality between the harmonic functions in (4.2.9) and (4.2.10) leads to a representation that relates the electric field to the surface currents

$$E_x = \sum_m \sum_n F_{mn} XY_{mn} \int J_x(x',y') \cos k_{xm}x' \sin k_{yn}y'\, dx'dy' \cos k_{xm}x \sin k_{yn}y$$

$$+ \sum_m \sum_n F_{mn} RZ_{mn} \int J_y(x',y') \sin k_{xm}x' \cos k_{yn}y'\, dx'dy' \cos k_{xm}x \sin k_{yn}y$$

$$E_y = \sum_m \sum_n F_{mn} RZ_{mn} \int J_x(x',y') \cos k_{xm}x' \sin k_{yn}y'\, dx'dy' \sin k_{xm}x \cos k_{yn}y$$

$$+ \sum_m \sum_n F_{mn} YX_{mn} \int J_y(x',y') \sin k_{xm}x' \cos k_{yn}y'\, dx'dy' \sin k_{xm}x \cos k_{yn}y$$

(4.2.11)

Variables defined in (4.2.10) and (4.2.11) are given below

$$p_{mn1} = \frac{b_{mn}}{j\omega\epsilon_0}\left(\frac{T_{mn1}}{\epsilon_1} + \frac{T_{mn2}}{\epsilon_2}\right) \tag{4.2.12}$$

$$p_{mn2} = f_{mn}k_{zmn2}\left(\frac{T_{mn1}}{k_{zmn1}^2} + \frac{T_{mn2}}{k_{zmn2}^2}\right) \tag{4.2.13}$$

$$p_{mn3} = b_{mn}U_{mn} \tag{4.2.14}$$

$$p_{mn4} = \frac{f_{mn}}{j\omega\mu_0}\, k_{zmn2}\, V_{mn} \tag{4.2.15}$$

$$U_{mn} = 1 - \frac{\epsilon_2}{\epsilon_1}\frac{T_{mn1}\, T_{mn2}}{k_{zmn2}^2} + \left(\frac{T_{mn1}}{\epsilon_1} + \frac{T_{mn2}}{\epsilon_2}\right)\frac{\epsilon_3}{T_{mn3}} \tag{4.2.16}$$

$$V_{mn} = 1 - \frac{T_{mn1}\, T_{mn2}}{k_{zmn1}^2} + \left(\frac{T_{mn1}}{k_{zmn1}^2} + \frac{T_{mn2}}{k_{zmn2}^2}\right)\frac{k_{zmn3}^2}{T_{mn3}} \tag{4.2.17}$$

$$X_{mn} = \frac{R_{mn}}{(k_{xmn}^2 + k_{ymn}^2)\, U_{mn}} \tag{4.2.18}$$

$$Y_{mn} = \frac{S_{mn}}{(k_{xmn}^2 + k_{ymn}^2)\, V_{mn}} \tag{4.2.19}$$

$$Z_{mn} = X_{mn} - Y_{mn} \tag{4.2.20}$$

$$R_{mn} = \frac{T_{mn1}}{\epsilon_1} + \frac{T_{mn2}}{\epsilon_2} \tag{4.2.21}$$

$$S_{mn} = k_0^2\left(\frac{T_{mn1}}{k_{zmn1}^2} + \frac{T_{mn2}}{k_{zmn2}^2}\right) \tag{4.2.22}$$

$$XY_{mn} = k_{xm}^2\, X_{mn} + k_{yn}^2\, Y_{mn}\ ,\ YX_{mn} = k_{yn}^2\, X_{mn} + k_{xm}^2\, Y_{mn} \tag{4.2.23}$$

$$RZ_{mn} = k_{xm}\, k_{yn}\, Z_{mn} \tag{4.2.24}$$

$$F_{mn} = L_{mn} \frac{j\omega\epsilon_0}{ab} \tag{4.2.25}$$

$$L_{mn} = \begin{cases} 4 \;, & m \text{ and } n > 0 \\ 0 \;, & m \text{ and } n = 0 \\ 2 \;, & m \neq 0 \text{ and } n = 0 \text{ or } n \neq 0 \text{ and } m = 0 \end{cases} \tag{4.2.26}$$

$$k_0^2 = \frac{\omega^2}{v^2} \tag{4.2.27}$$

$$k_{xm} = \frac{m\,\pi}{a} \;\; ; \;\; k_{yn} = \frac{n\,\pi}{b} \tag{4.2.28}$$

$$k_{zmni} = \sqrt{k_0^2\, \epsilon_i - (k_{xm}^2 + k_{yn}^2)} \tag{4.2.29}$$

$$T_{mni} = k_{zmni} \tan (k_{zmni}\, H_i) \tag{4.2.30}$$

f_{mn} and b_{mn} were determined from the boundary condition in terms of currents.

The real space Green function for the electric field is obtained by replacing the surface currents in (4.2.11) by Dirac sources [79].

4.2.2 Moment Method

Equation (4.2.11) represents a Fredholm integral equation of the first kind which maps the surface current into an electric field on the interface. Following the moment method procedure, the current is expanded into basis functions. These are then substituted in (4.2.11). In a subsequent step (4.2.11) is tested with suitable functions which in the present case were chosen to be identical to the basis functions leading to a Galerkin implementation of the method.

The present method employs roof top functions as the basis elements. These were introduced by Glisson and Wilton [58] and have been applied by various authors [48,63,72]. Figure 4-2 shows the discretization of the metallized surface with discretization Δx and Δy in x and y direction, respectively. The center of x-directed currents is marked with a cross, the center of y-directed currents is marked with a circle. Note, the x and y directed currents are offset by $(\Delta x/2, \Delta y/2)$ in order to assure edge conditions and generate correct results. A detailed discussion for the current offset can be found in [62].

Following the discussion in the previous paragraph the total current is approximated by

$$J = \sum_k a_{xk}\, J_x(x,y,x_k,y_k) + \sum_l a_{yl}\, J_y(x,y,x_l,y_l) \tag{4.2.31}$$

with separable currents

$$J_x(x,y,x_k,y_k) = J_{xx}(x,x_k)\, J_{xy}(y,y_k) \tag{4.2.32}$$

$$J_y(x,y,x_l,y_l) = J_{yx}(x,x_l)\, J_{yy}(y,y_l) \tag{4.2.33}$$

where

$$J_{uu}(u,u_k) = \begin{cases} \dfrac{u - u_k}{\Delta u} + 1 & , \quad u_k - \Delta u < u < u_k \\ \dfrac{u_k - u}{\Delta u} + 1 & , \quad u_k < u < u_k + \Delta u \\ 0 & , \quad \text{otherwise} \end{cases} \tag{4.2.34}$$

u = x or y

$$J_{uv}(v,v_k) = \begin{cases} 1 & , \quad v_k - \Delta v/2 < v < v_k + \Delta v/2 \\ & \\ 0 & , \quad \text{otherwise} \end{cases} \tag{4.2.35}$$

uv = xy or yx.

With a scalar product between f(x,y) and g(x,y) defined as

$$s = \int\int f(x,y)\, g(x,y)\, dx\, dy \tag{4.2.36}$$

the linear system obtained, after applying the testing procedure, can be summarized as follows

$$\begin{bmatrix} V_x \\ V_y \end{bmatrix} = \begin{bmatrix} P_{xx} & P_{xy} \\ P_{yx} & P_{yy} \end{bmatrix} \begin{bmatrix} A_x \\ A_y \end{bmatrix} \tag{4.2.37}$$

The left hand side represents the reactance [59] of the electric field on the metallized surface and a testing current. These vanish on the metal except for subsections where sources are defined. The P matrix contains the testing products and the Green's dyadic of the associated boundary value problem. Vector A is formed by the expansion coefficients for current as given in (4.2.31). In particular

$$V_{xi} = \int\int E_x\, J_{xi}\, dx\, dy$$

$$V_{yi} = \int\int E_y\, J_{yi}\, dx\, dy \tag{4.2.38}$$

$$P_{xx}^{ij} = \sum_m \sum_n G_{mn}^{xx} \cos k_{xm}x_{jx} \sin k_{yn}y_{jx} \cos k_{xm}x_{ix} \sin k_{yn}y_{ix}$$

$$P_{xy}^{ij} = \sum_m \sum_n G_{mn}^{xy} \sin k_{xm}x_{jy} \cos k_{yn}y_{jy} \cos k_{xm}x_{ix} \sin k_{yn}y_{ix}$$

$$P_{yx}^{ij} = \sum_m \sum_n G_{mn}^{yx} \cos k_{xm}x_{jx} \sin k_{yn}y_{jx} \sin k_{xm}x_{iy} \cos k_{yn}y_{iy}$$

$$P_{yy}^{ij} = \sum_m \sum_n G_{mn}^{yy} \sin k_{xm}x_{jy} \cos k_{yn}y_{jy} \sin k_{xm}x_{iy} \cos k_{yn}y_{iy} \tag{4.2.39}$$

$$A_{xi} = a_{xi}$$
$$A_{yi} = a_{yi} \qquad (4.2.40)$$

and

$$G_{mn}^{xx} = F_{mn}\, XY_{mn}\, G_t^2(\Delta x)\, G_r^2(\Delta y)$$
$$G_{mn}^{xy} = F_{mn}\, R_{mn}\, G_t(\Delta y)\, G_r(\Delta x)\, G_t(\Delta x)\, G_r(\Delta y)$$
$$G_{mn}^{yx} = F_{mn}\, R_{mn}\, G_t(\Delta x)\, G_r(\Delta y)\, G_t(\Delta y)\, G_r(\Delta x)$$
$$G_{mn}^{yy} = F_{mn}\, YX_{mn}\, G_t^2(\Delta y)\, G_r^2(\Delta x) \qquad (4.2.41)$$

where

$$G_t(\Delta u) = \begin{cases} \dfrac{2}{\Delta u\, k_u^2}\,(1 - \cos(k_u \Delta u)) & k_u \neq 0 \\ \Delta u & k_u = 0 \end{cases} \qquad (4.2.42)$$

$$G_t(\Delta u) = \begin{cases} \dfrac{2}{k_u}\,(\sin(k_u \Delta u/2) & k_u \neq 0 \\ 0 & k_u = 0 \end{cases} \qquad (4.2.43)$$

The doubled infinite summations in (4.2.39) need to be truncated at a suitable upper bound.

4.2.3 Enhanced Algorithm

The evaluation of the elements P^{ij} of the moment matrix is rather time consuming due to the two-dimensional summation and the repeated computation of the Green's dyadic with associated harmonic functions. For instance, the computation of the input impedance of a stub using the formulation (4.2.39) required more than two hours per frequency on

an Ardent work station. With the novel technique developed in this work, a reduction in computation time to 0.4 seconds was achieved.

Let the total number of expansion functions be IEX. If the summations (4.2.39) are truncated at the upper limit ISU then a total number of ITC = $ISU^2*IEX*(IEX-1)/2$ operations are required to obtain the moment matrix. Where an operation is defined as the evaluation of one element in the summation for one element P^{ij}. With typical numbers e.g. ISU = 500 and IEX = 300, ITC amounts to about 11 billion operations. The time requirement for the solution of the linear system (4.2.37) is negligible compared to the formation of the matrix.

Efficiency considerations for the summation procedure in (4.2.39) have already been discussed by Rautio [62]. He recognized the periodicity of the harmonic functions and developed a summation scheme which avoids the periodic evaluation of the trigonometric functions. However, the reduction in operations per element P^{ij} is estimated to not more than a factor of 10. The possible application of fast Fourier transforms (FFT) has also been addressed by Rautio in [62]. The present approach makes use of two techniques which lead to a drastic reduction of computation times. As a first technique customized 2D-FFT routines are employed to compute index tables. The second technique constitutes the application of specialized indexing routines which allow the derivation of all elements of the moment matrix by simple linear combination of elements of the index tables. This second technique completely eliminates the IEX·(IEX-1)/2 operations for the formation of the moment matrix.

In order to employ FFT subroutines the representation of the moment matrix has to be transformed into a suitable form. In addition the interface is uniformly discretized in x and y direction such that

$$x_{ix} = p_{ix}\,\Delta x \quad , \quad p_{ix} = 0,1,\ldots,M$$

$$y_{iy} = s_{iy}\,\Delta y \quad , \quad s_{iy} = 0,1,\ldots,N$$

$$x_{iy} = \left(p_{iy} + \frac{1}{2}\right)\Delta x \quad , \quad p_{iy} = 0,1,\ldots,M-1$$

$$y_{ix} = \left(s_{ix} + \frac{1}{2}\right)\Delta y \quad , \quad s_{ix} = 0,1,\ldots,N-1 \qquad (4.2.44)$$

Since the respective operator of the Fredholm integral equation (4.2.39) is self-adjoint the moment matrix is symmetric and P_{yx} which is equal to P_{xy} is no longer considered in the numerical treatment. After using trigonometric identities and substituting (4.2.44) into (4.2.39) the moment matrix P can be rewritten as

$$P_{xx}^{ij} = f_{xx}(p_{jx}- p_{ix}\ ,\ s_{jx}- s_{ix}) - f_{xx}(p_{jx}- p_{ix}\ ,\ s_{jx}+ s_{ix})$$
$$+ f_{xx}(p_{jx}+ p_{ix}\ ,\ s_{jx}- s_{ix}) - f_{xx}(p_{jx}+ p_{ix}\ ,\ s_{jx}+ s_{ix}) \qquad (4.2.45)$$

$$P_{xy}^{ij} = f_{xy}(p_{jy}+ p_{ix}\ ,\ s_{jy}+ s_{ix}) - f_{xy}(p_{jy}+ p_{ix}\ ,\ s_{jy}- s_{ix})$$
$$+ f_{xy}(p_{jy}- p_{ix}\ ,\ s_{jy}+ s_{ix}) - f_{xy}(p_{jy}- p_{ix}\ ,\ s_{jy}- s_{ix}) \qquad (4.2.46)$$

$$P_{yy}^{ij} = f_{yy}(p_{jy}- p_{iy}\ ,\ s_{jy}- s_{iy}) + f_{yy}(p_{jy}- p_{iy}\ ,\ s_{jy}+ s_{iy})$$
$$- f_{yy}(p_{jy}+ p_{iy}\ ,\ s_{jy}- s_{iy}) - f_{yy}(p_{jy}+ p_{iy}\ ,\ s_{jy}+ s_{iy}) \qquad (4.2.47)$$

with

$$f_{xx}(u,v) = \sum_m \sum_n G_{mn}^{xx} \cos \frac{m\pi u}{M} \cos \frac{n\pi v}{N}$$

$$f_{xy}(u,v) = \sum_m \sum_n G_{mn}^{xy} \sin \frac{m\pi(u + 1/2)}{M} \sin \frac{n\pi(v + 1/2)}{N}$$

$$f_{yy}(u,v) = \sum_m \sum_n G_{mn}^{yy} \cos \frac{m\pi u}{M} \cos \frac{n\pi v}{N} \qquad (4.2.48)$$

The expressions for P^{ij} (4.2.45)–(4.2.47) are now in a form which is suited for the application of 2D discrete FFTs. Now each element in the moment matrix could be computed by making use of the FFT algorithm which would result in considerable computation time reductions. For a matrix with dimension IEX this would require IT = IEX*(IEX–1)/2 evaluations by FFT routines e.g. IT = 4485 if IEX = 300. A technique is presented here which allows us to reduce the IT evaluations to IT = 3 evaluations for any matrix size. A distinct feature of the developed technique is the fact that only 12 FFT transforms are necessary in order to establish the entire moment matrix, independent of matrix size. The elements P^{ij} are obtained from a linear combination of components of the FFTs with respect to the transform variable as will be outlined in the following. Instead of computing (4.2.45)–(4.2.47) for each P_{xx}^{ij}, P_{xy}^{ij}, P_{yy}^{ij}. Only three FFTs are computed and stored in suitable arrays:

$$P_{xx}(u,v) = f_{xx}(u,v) \quad , \quad u = 0,\ldots,M \quad ; \; v = 0,\ldots,N \qquad (4.2.49)$$

$$P_{xy}(u,v) = f_{xy}(u,v) \quad , \quad u = 0,\ldots,M-1 \; ; \; v = 0,\ldots,N-1 \qquad (4.2.50)$$

$$P_{yy}(u,v) = f_{yy}(u,v) \quad , \quad u = 0,\ldots,M \quad ; \; v = 0,\ldots,N \qquad (4.2.51)$$

The elements of the moment matrix are then derived from a linear combination of (4.2.49)-(4.2.51) as implied in (4.2.45)-(4.2.47) under consideration of the periodicity of the trigonometric functions.

As mentioned in a previous paragraph, the doubled infinite summations have to be truncated at a suitable bound such that a certain convergence criteria is fulfilled. This upper bound can exceed the period of the respective FFTs. In other words, the sampling ratio defined as the quotient of the number of spatial frequency samples per discretization length is larger than unity. To circumvent this problem the functions G_{mn} in (4.2.48) are presampled at periodic intervals to form a summation which is then submitted to the FFT routines. The idea of such a first stage summation has been used previously by Rautio [62]; however, the implementation was different. As a consequence of the first stage summation scheme, each of the 3 FFTs in (4.2.49)-(4.2.51) is split into 4 FFTs which yields a total number of 12 FFTs for the evaluation of the moment matrix. To incorporate an arbitrary number of spatial frequencies in the FFT algorithm, the three basic FFT formulations given in equations (4.2.49)- (4.2.51) are decomposed as follows.

$$\sum_m \sum_n G_{mn}^{xx} \cos \frac{m\pi p}{M} \cos \frac{n\pi s}{N} = \sum_m \sum_n G_{mn}^{xxee} \cos \frac{m\pi p}{M} \cos \frac{n\pi s}{N}$$

$$+ (-1)^s \sum_m \sum_n G_{mn}^{xxeo} \cos \frac{m\pi p}{M} \cos \frac{n\pi s}{N} + (-1)^p \sum_m \sum_n G_{mn}^{xxoe} \cos \frac{m\pi p}{M} \cos \frac{n\pi s}{N}$$

$$+ (-1)^{(s+p)} \sum_m \sum_n G_{mn}^{xxoo} \cos \frac{m\pi p}{M} \cos \frac{n\pi s}{N} \qquad (4.2.52)$$

$$\sum_m \sum_n G_{mn}^{xy} \sin \frac{m\pi(p+1/2)}{M} \sin \frac{n\pi(s+1/2)}{N} =$$

$$\sum_m \sum_n G_{mn}^{xyee} \sin \frac{m\pi(p+1/2)}{M} \sin \frac{n\pi(s+1/2)}{N}$$

$$+ (-1)^s \sum_m \sum_n G_{mn}^{xyeo} \sin \frac{m\pi(p+1/2)}{M} \cos \frac{n\pi(s+1/2)}{N}$$

$$+ (-1)^p \sum_m \sum_n G_{mn}^{xyoe} \cos \frac{m\pi(p+1/2)}{M} \sin \frac{n\pi(s+1/2)}{N}$$

$$+ (-1)^{(s+p)} \sum_m \sum_n G_{mn}^{xyoo} \cos \frac{m\pi(p+1/2)}{M} \cos \frac{n \text{ pai } (s+1/2)}{N} \qquad (4.2.53)$$

$$\sum_m \sum_n G_{mn}^{yy} \cos \frac{m\pi p}{M} \cos \frac{n\pi s}{N}$$

is identical to (4.2.52) with G_{mn}^{xx} replaced by G_{mn}^{yy}. The abbreviations in (4.2.52) and (4.2.53) are defined as follows

$$G_{mn}^{xxee} = \sum_{i_e} \sum_{j_e} G^{xx}(m+i_eM \ , \ n+j_eN)$$

$$G_{mn}^{xxeo} = \sum_{i_e} \sum_{j_o} G^{xx}(m+i_eM \ , \ n+j_oN)$$

$$G_{mn}^{xxoe} = \sum_{i_o} \sum_{j_e} G^{xx}(m+i_oM \ , \ n+j_eN)$$

$$G_{mn}^{xxoo} = \sum_{i_o} \sum_{j_o} G^{xx}(m+i_oM \ , \ n+j_oN)$$

$$G_{mn}^{yyee} = \sum_{i_e} \sum_{j_e} G^{yy}(m+i_eM \ , \ n+j_eN)$$

$$G_{mn}^{yyeo} = \sum_{i_e} \sum_{j_o} G^{yy}(m+i_eM \ , \ n+j_oN)$$

$$G_{mn}^{yyoe} = \sum_{i_o} \sum_{j_e} G^{yy}(m+i_oM \ , \ n+j_eN)$$

$$G_{mn}^{yyoo} = \sum_{i_o} \sum_{j_o} G^{yy}(m+i_oM\ ,\ n+j_oN)$$

$$G_{mn}^{xyee} = \sum_{i_e} \sum_{j_e} G^{xy}(m+i_eM\ ,\ n+j_eN)\ (-1)^{(ie/2+je/2)}$$

$$G_{mn}^{xyeo} = \sum_{i_e} \sum_{j_o} G^{xy}(m+i_eM\ ,\ n+j_oN)\ (-1)^{(ie/2+jo/2)}$$

$$G_{mn}^{xyoe} = \sum_{i_o} \sum_{j_e} G^{xy}(m+i_oM\ ,\ n+j_eN)\ (-1)^{(io/2+je/2)}$$

$$G_{mn}^{xyoo} = \sum_{i_o} \sum_{j_o} G^{xy}(m+i_oM\ ,\ n+j_oN)\ (-1)^{(io/2+jo/2)}$$

and

$$i_e, j_e = 0,2,4,\ldots$$

$$i_o, j_o = 1,3,5,\ldots \qquad (4.2.54)$$

The formation of the moment matrix is summarized in Figure 4-3. After discretizing the geometry, each Green's dyadic is presampled following equation (4.2.54). Next, 2D FFTs are applied as outlined in Equations (4.2.49) through (4.2.51). Results of the FFTs are then stored to form index tables. Now the moment matrix of any geometry on the discretized interface can be built by a suitable linear combination of the elements of the three index tables as implied in Equations (4.2.45) through (4.2.47). As long as the geometry of the shielding and the dielectric layers remain the same, any metallization pattern can be characterized by the same index tables. In this case computation times are determined by the time requirement for the solution of the linear system in the moment procedure.

4.3 Identification of Discontinuity Parameter

4.3.1 Review

Two conceptually different approaches have been used for the determination of the parameter of a discontinuity in a uniform transmission structure. In a deterministic procedure an impressed source is applied as excitation mechanism for a transmission line. Katehi and Alexopoulos [46] introduced a gap generator as excitation mechanism of a microstrip transmission line. From the standing wave ratio on the transmission line and the location of current or voltage maxima the parameter associated with the discontinuity can be determined. Jackson and Pozar [47] use sinusoidal incidental and reflected waves with the coefficient of the reflected wave being determined from the numerical treatment. Jansen and Wertgen [69] apply a current source and determine the amplitudes of the incident and reflected waves from the standing wave pattern by an extraction technique. Skrivervik and Mosig [72] recently presented a flexible technique which is adaptable to various excitation mechanisms. In the first step, the impedance matrix of the entire structure including excitations, transmission lines and discontinuities is computed. In the second step, the Z matrix of only the transmission lines is computed where the same excitation mechanism is used as in the first step. The impedance matrix of the discontinuity is then extracted by employing a generalized chain matrix formulation.

As opposed to a deterministic procedure the second approach to the parameter identification of discontinuities is the resonant tech-

nique which leads to an eigenvalue problem. In [52] Jansen describes a simulated resonant experiment for n port discontinuity structures. This has been applied by Koster [51] for the characterization of various discontinuities. Sorrentino and Itoh [65] make use of a transverse resonant technique for the analysis of finline discontinuities. In resonant simulations no sources need to be specified, thus source related problems can be eliminated. As Koster and Jansen point out, "due to the stationary property which the approach exhibits it is suited to provide even the numerically sensitive phase information for strip and slot-type discontinuities" [50].

Due to these advantages, resonant techniques are also popular for the experimental investigation of microstrip discontinuities [33-36]. A major draw back of resonant simulations has been the intensive computer time requirement which is about a factor of 100 larger as compared to the deterministic approach. Due to this reason, resonant simulations have been limited to basic structures such as microstrip open end, steps and gaps.

4.3.2 Symmetric Two Port

A symmetric two port is characterized by two parameters. These can be determined from the linearly independent modes of the system.

Consider the symmetric two port in Figure 4-4a. Transmission lines are connected at the terminals for the resonant experiments as shown in Figures 4-4b and 4-4c. The lines of characteristic impedance Z and propagation constant β are short circuited at the end. These shorts are realized in the numerical experiment to be electric walls.

To derive the resonance condition of the symmetric two port shown in Figure 4-4a, the terminal voltages are written as

$$\begin{bmatrix} U_1 \\ U_2 \end{bmatrix} = \begin{bmatrix} Z_{11} & Z_{12} \\ Z_{12} & Z_{11} \end{bmatrix} \begin{bmatrix} I_1 \\ I_2 \end{bmatrix} \tag{4.3.1}$$

with the terminal constraints

$$\begin{bmatrix} U_1 \\ U_2 \end{bmatrix} = -\begin{bmatrix} Z_i & 0 \\ 0 & Z_i \end{bmatrix} \begin{bmatrix} I_1 \\ I_2 \end{bmatrix} \tag{4.3.2}$$

which yields the system

$$\begin{bmatrix} Z_{11}+Z_i & Z_{12} \\ Z_{12} & Z_{11}+Z_i \end{bmatrix} \begin{bmatrix} I_1 \\ I_2 \end{bmatrix} = 0 \tag{4.3.3}$$

and represents a generalized eigenvalue problem. The eigenvalue represents the resonant frequency or alternatively the resonant stub length l, where the input impedance of the transmission line is given by

$$Z_i = j\, Z \tan(\beta l) \tag{4.3.4}$$

The two solutions of (4.3.3) with corresponding eigenvectors are

$$Z_e = -Z_i = Z_{11} + Z_{12}\ ,\ (I_1, I_2) = (1,1)\ \ ,\ \text{even mode} \tag{4.3.5}$$

$$Z_o = -Z_i = Z_{11} - Z_{12}\ ,\ (I_1, I_2) = (1,-1)\ ,\ \text{odd mode} \tag{4.3.6}$$

The network representation of both resonant conditions are shown in Figures 4-4b and 4-4c. The normalized impedance matrix is computed from the resonant length of the respective modes. The propagation constant β must be derived from the same numerical technique which is

used for the resonant experiment since Z_i can be rather sensitive to the argument βl. The S parameter representation of the two port can be obtained from the transform

$$[S] = [Z' + I]^{(-1)}[Z' + I] \tag{4.3.7}$$

where I is the identity matrix and Z′ represents the normalized impedance matrix.

4.4 Parasitic Waveguide Modes

In shielded microstrip structures, parasitic waveguide modes exist above their cut off frequency. These modes are excited at discontinuities and form a resonant system for boxed microstrip housings. Since the presented method is a rigorous full wave analysis these modes can be present and influence the parameter extraction process. A prior knowledge of the conditions under which resonant parasitic waveguide modes exist is essential.

The treatment of waveguide modes can be found in the literature [59,61,64,77]. It has been demonstrated [64] that the field pattern of the dominant LSM_0 mode is not significantly disturbed by the incorporation of a metal strip with moderate dimensions. Results of the analysis for the parasitic waveguide modes for the microstrip structure with removed metallization are then adopted for the metallized configuration. The determination of the propagation constant of the waveguide modes can be computed from the transcendental dispersion relation for LSE and LSM modes. In Figure 4–5 the normalized square of the propagation constant is plotted for various housing dimensions.

If electric walls are placed perpendicular to the propagation path to form a boxed structure the continuous spectrum of the propagating modes is reduced to form the discrete resonant spectrum. The normalized square of the resonant wave numbers of first and second order

$$\frac{(m\pi/a)^2}{k_0^2} \quad , \quad m = 1,2 \tag{4.3.8}$$

are also plotted in the diagrams. The resonant frequencies of the boxed structure are then determined from the intersection of these curves with the continuous waveguide spectrum. Comparing Figure 4-5a to Figure 4-5c demonstrates that larger housing dimensions cause a reduction in parasitic resonant frequencies. For resonant experiments (of the microstrip mode) it is therefore necessary to choose a small housing which however has to be large enough such that discontinuity effects have decayed at the location of the housing and which allows the establishment of the linearly independent resonant microstrip modes necessary for the determination of symmetric two port parameter. In addition, the distance between the striplines and the shielding walls have to be chosen appropriately in order to avoid undesired interactions with the microstrip housing.

4.5 Numerical Results

4.5.1 Open Circuited Microstrip Stub

4.5.1.1 Input Impedance. As an initial confidence test for the presented technique, the input impedance of a microstrip stub was computed and compared to results obtained by Rautio and Harrington

[63]. Dimensions for the shielding box and strip geometry are adopted from [63]. The box was 4 cm long, 2 cm wide and 5 cm high. The strip line was 1 cm wide and 2.81 cm long and was deposited on a 1 cm thick substrate with a relative dielectric constant of 10. The results are shown in Figure 4-6 and the agreement is obvious.

4.5.1.2 Effective Length. The open end discontinuity of a microstrip line can be characterized by an effective length extension l_{eff} or an equivalent terminating capacitance which accounts for the fringing fields at the open end. A dynamic simulation of the open end effect in a shielded environment has been developed by Itoh [42], Jansen and Koster [78], Dunleavy and Katehi [55] and are included for comparison in Figure 4-7. The box and strip dimensions were chosen to be identical to those used by Dunleavy. The box was 7.747 mm wide and 5.08 mm high. The strip was deposited on a substrate 0.635 mm in height with an effective dielectric constant of 9.6. The W/H ratio was 1.57. The frequency behavior of the effective length computed in this work behaves in the same manner as was described by Koster [51]. For low frequencies the length decreases then passes through a minimum and increases for higher frequencies. Dunleavy obtains a steady increase with frequency for the effective length. The box used in the presented analysis exhibits a resonance around 24 GHz for the specified dimensions which explains the deviation of the effective length at this point from the results of Jansen and Dunleavy. The corresponding dispersion diagram for this particular configuration is shown in Figure 4-5e. Itoh's results deviate considerably from the remain-

ing curves which has already been discussed by Jansen [78]. He attributes the difference in part to the inadequacy of the applied basis functions.

4.5.2 Microstrip Gap Discontinuity

4.5.2.1 Network Parameter. To further verify the proposed technique, a microstrip series gap has been analyzed and compared to recent results from Dunleavy [57] in Figure 4-8. The shielding box of equal height and width was 6.35 mm wide. A substrate thickness of 0.635 mm was assumed and the stripline width was chosen to be equal to the substrate height. The gapwidth g was 0.381 mm. Close agreement for the phase of the S parameter was achieved. The magnitude of the transmission S_{12} exhibits a slightly different slope and crosses at about 12 GHz.

4.5.3 Microstrip Right Angle Bend

4.5.3.1 Introduction. It appears that up to the first half of this year, results for the scattering parameter of microstrip bends in a shielded environment have not been published. This is believed to be due to the large matrix sizes encountered due to the 2D current distribution on the metallized surface. In addition the infinite 2D summation in the associated Green's function of the conventional approach resulted in unacceptable computation times. Very recently Jansen and Wiemer [71] presented a full-wave theory based development of mm-wave circuit models for microstrip open end, gap, step, bend and tee discontinuities. A topology-sensitive modeling concept is intro-

duced which accounts for package effects in MMIC housing. Data was presented that demonstrates the effect of box resonances on the S parameter of a right angle bend geometry.

In the following, various microstrip right angle bend discontinuities are analyzed. Housing effects, current distributions and a compensation effect are illustrated for single and doubled layer substrates.

4.5.3.2 Current Distribution. As a first example the current distribution on a right angled bend is illustrated for the even and odd resonance. A second order resonance is simulated for the even mode and a first order resonance is shown for the odd mode. The strip with a W/H ratio of 1 was deposited on a 0.635 mm Alumina substrate and analyzed in a housing of a = 12.7 mm, b = 12.7 mm, and c = 3.81 mm. In Figure 4-9 the total y directed current on one arm of the bend is plotted for the even mode. At the shielding wall the current exhibits a maximum then passes through a minimum, reaches another maximum and terminates in a minimum at the corner region. The associated total x directed current (Figure 4-9b) is an order of magnitude smaller than the y directed current at a location away from the corner. As the corner is approached the x directed current increases to compensate for the change in the direction of current flow. In Figure 4-10 the current density distribution at a cross section perpendicular to the y axis is illustrated for different distances away from the bend region.

Figure 4-11a illustrates the total y-directed current on the stripline for the odd mode resonance. Starting with a maximum at the

shielding walls, the current passes through a minimum and approaches a maximum in the bend region. The corresponding total x-directed current, shown in Figure 4-11b increases as the corner is approached which again is due to the change of the current direction. The current density distribution at a cross section perpendicular to the y axis is illustrated in Figure 4-12.

4.5.3.3 Network Parameter.

4.5.3.3.1 Right angle bend. The S parameters for typical right angle bend geometries having various W/H ratios are shown in Figure 4-13 for an alumina substrate of height 0.635 mm. All bends are analyzed in a square box of 12.7 mm side length and 3.81 mm height. The corresponding dispersion diagram is shown in Figure 4-5b. Note that the box resonance in the vicinity of 15 GHz does not coincide with a microstrip resonance and is therefore not included in Figure 4-13. As can be seen from Figure 4-13a, for the chosen geometries, the reflection coefficient increases with the W/H ratio. For the 50 Ohm line (W/H = 1) S parameter simulations are compared to design formulas from Kirschning et al. [36] which were derived from measurements in the frequency range between 2 GHz to 14 GHz. The deviation in magnitude of S_{11} is within 3% for the frequency range up to 14 GHz. However, larger differences are observed for the phase beyond 4 GHz.

As a next example, a right angle bend on a 0.503 mm substrate with dielectric constant of 9.9 is analyzed. S_{11} is shown in Figure 4-14a for W/H = 1 and it compares favorably to results of the same bend in an open environment which has been simulated recently by

Harokopus and Katehi [73]. However, agreement in the phase could not be achieved. S parameters obtained from the waveguide model [80] are also included and in this case the magnitude for S_{11} does not match the results obtained from this method and from Harokopus. However, reasonable agreement is obtained for the phase. Dimensions of the shielding were chosen as a = b = 10.84 mm, c = 5.08 mm.

Next, a bend is simulated in the frequency range between 50 GHz and 150 GHz. The bend of 100 μm in width is deposited on a 100 μm GaAs substrate with a 5 μm oxide layer. The box dimensions were a = 1.9 mm and c = 1.05 mm. Figure 4-15 shows the associated S parameter.

To show the effect of box resonances, the height of the box is reduced to c = 200 μm. The oxide layer is removed in this example. The corresponding dispersion diagram for this configuration is shown in Figure 4-5d and predicts a resonance of the parasitic waveguide modes in the vicinity of 80 GHz which is verified by the S parameter computations shown in Figure 4-16.

4.5.3.3.2 Compensated bend. As a last example the S parameter of a right angle bend are compared for a compensated corner. The compensation is obtained by cutting out a square at the corner of the bend. The form of the compensation is shown in the insert of Figure 4-16. The configuration of the first example is used with a W/H ratio of 2. The S parameter are compared for a compensation ratio of s/W = 0.8. Figure 4-16a shows the magnitude of S_{11}. For the compensated case a considerable reduction of S_{11} is achievable. The ratio of S_{11} for the compensated case and S_{11} for the uncompensated case is about 0.125 at the low frequency end at 6 GHz and 0.27 at the high frequency

end at 20 GHz. Comparing the deviation in phase of S_{11} (Figure 4-16b) yields a change of capacitive to inductive loading which is due to the increased current crowding in the corner region of the compensated edge.

4.6 Conclusion

A full wave analysis has been presented which is capable of characterizing a variety of microstrip discontinuities on a multilayered substrate. Limitations of some previous full wave methods are overcome by the development of a new technique which considerably reduces the computing time. This allows for the incorporation of 2D surface currents in the analysis. The method was applied to simulate resonant modes for various discontinuity structures in order to demonstrate its capabilities.

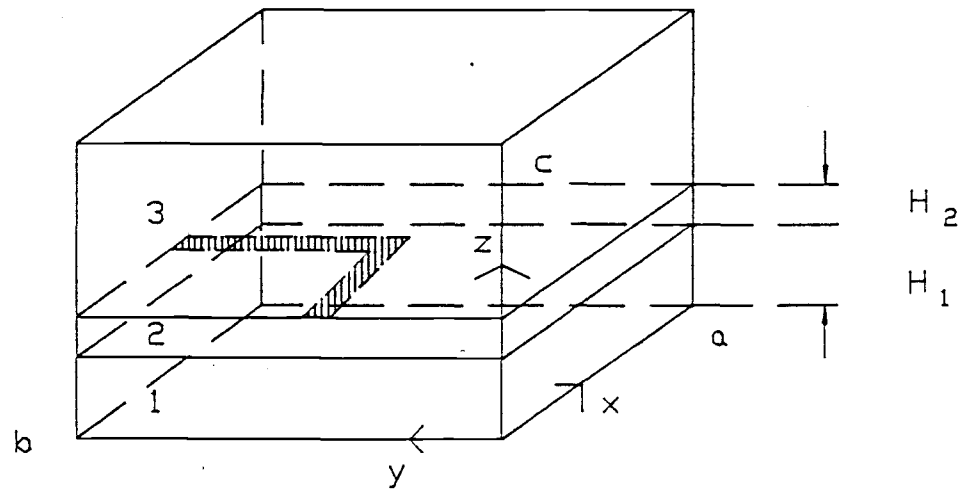

Figure 4-1. Microstrip discontinuity in shielded box.

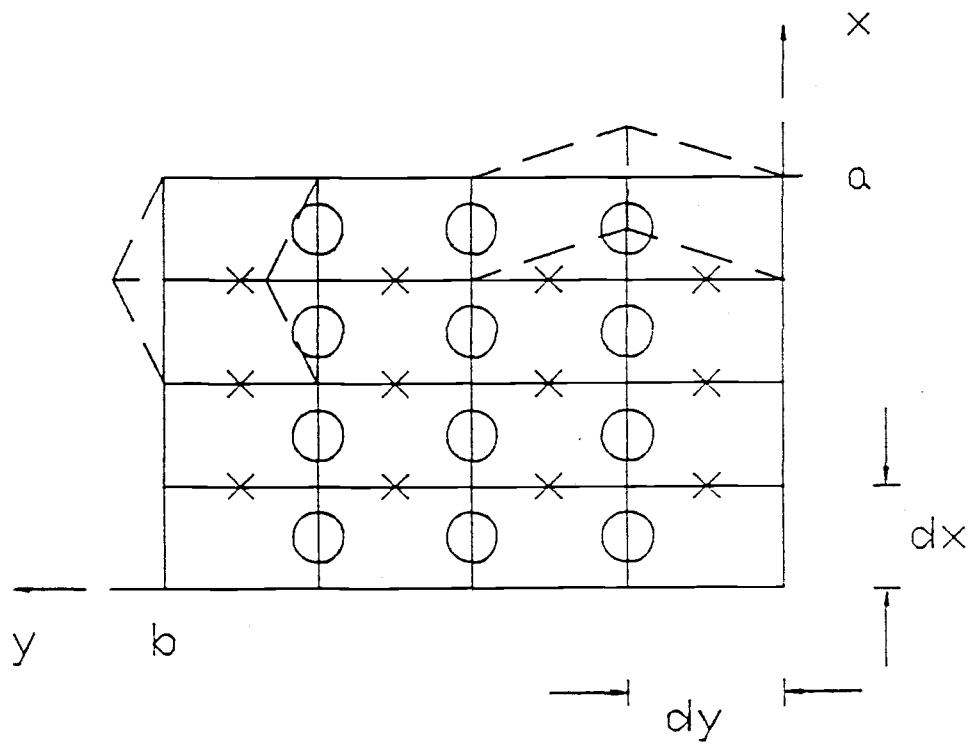

Figure 4-2. Discretization of conductor surface. Crosses represent center of x-directed current; circles represent centers of y-directed currents.

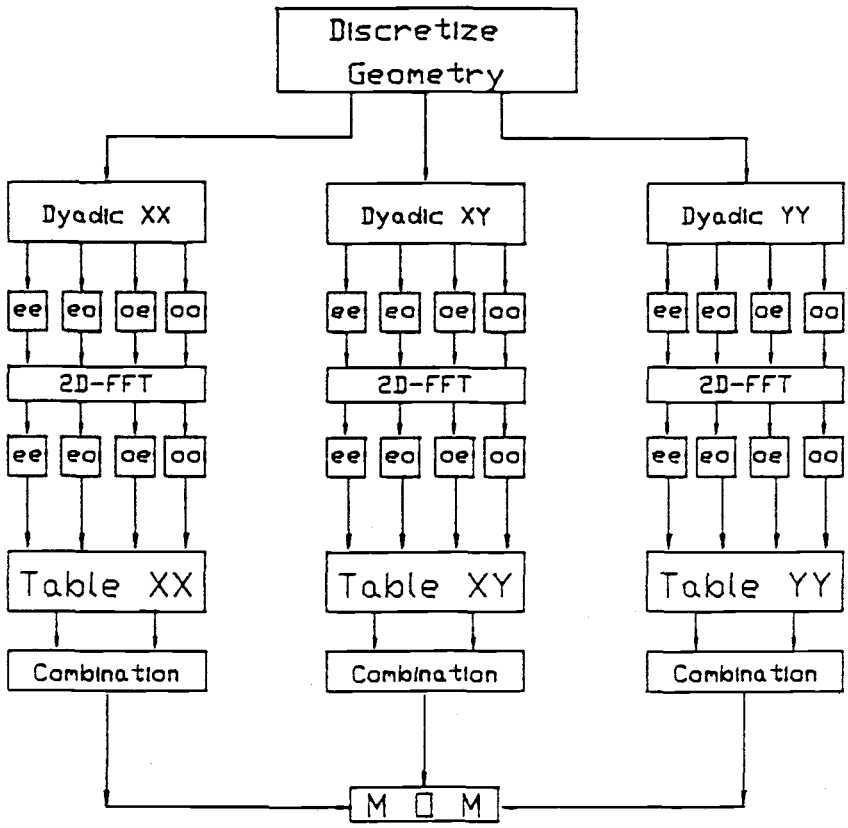

Figure 4-3. Enhanced algorithm for establishing the moment matrix (MOM).

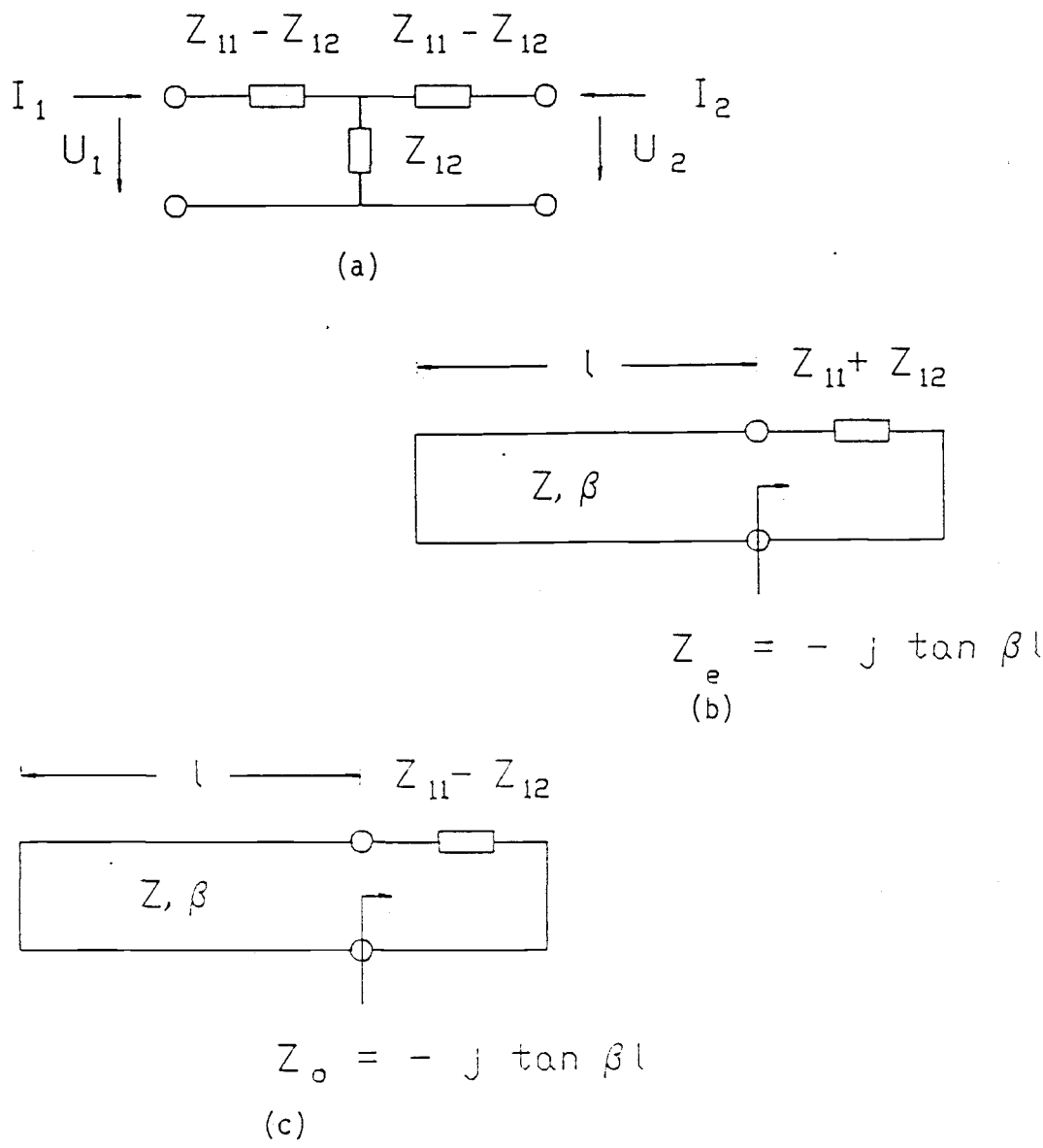

Figure 4-4. Symmetric two port: (a) Network representation; (b) Network representation with terminating transmission line - even mode; (c) Network representation with terminating transmission line - odd mode.

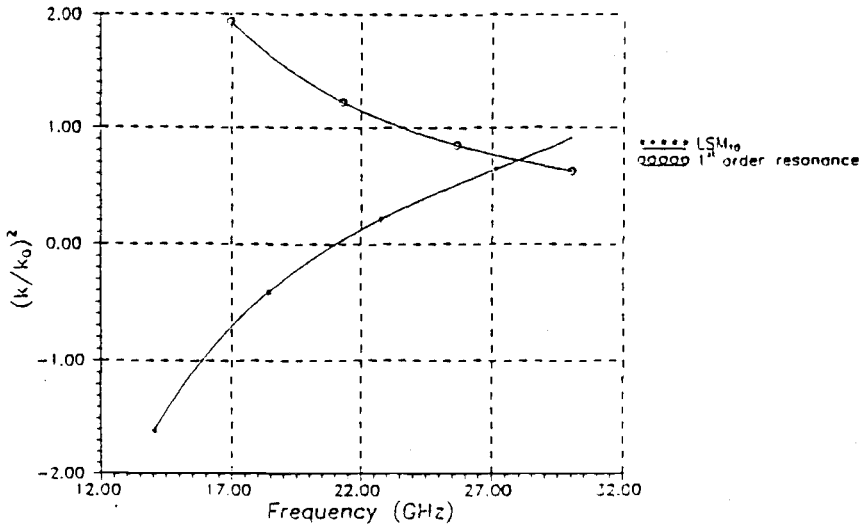

(a)

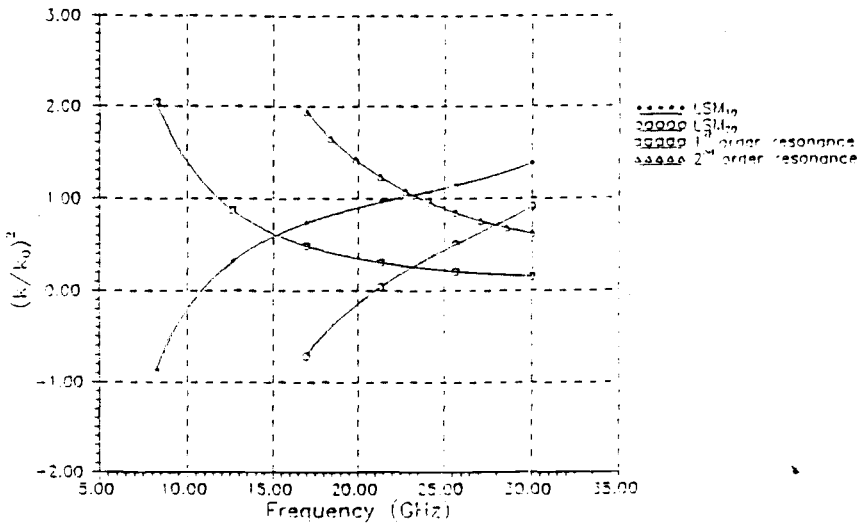

(b)

Figure 4–5. Dispersion diagram for certain wave guide geometries with resonant modes for structures in a shielding box: (a) Box dimension a=6.35mm, b=a, c=3.81mm, H_1=0.635mm, ϵ_1=9.8; (b) Box dimension a=12.7mm, b=a, c=3.81mm, H_1=0.635mm, ϵ_1=9.8.

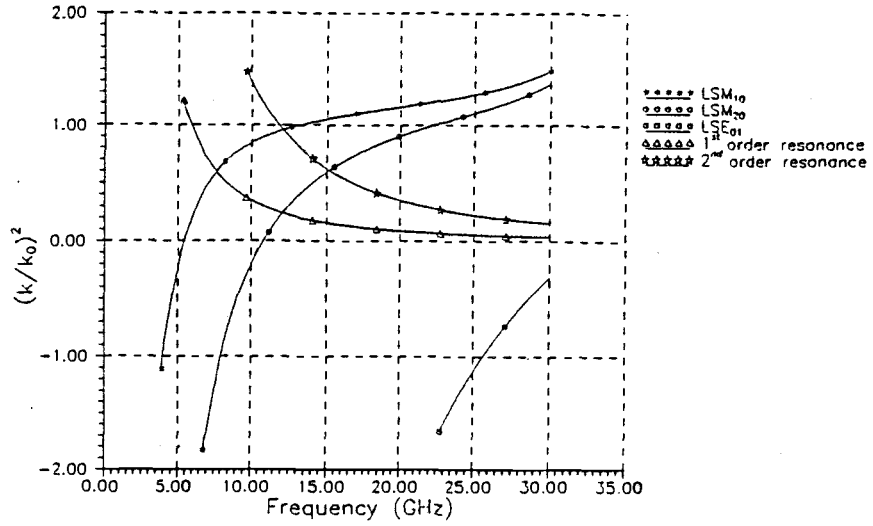

(c)

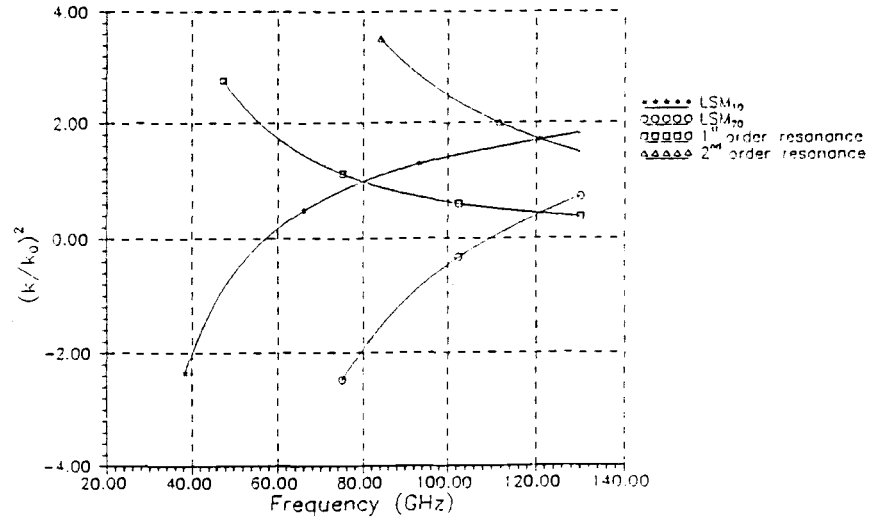

(d)

Figure 4-5. Continued: (c) Box dimension a=25.4mm, b=a, c=3.81mm, H_1=0.635mm, ϵ_1=9.6; (d) Box dimension a=1.9mm, b=a, c=0.2mm, H_1=0.1mm, ϵ_1=12.9.

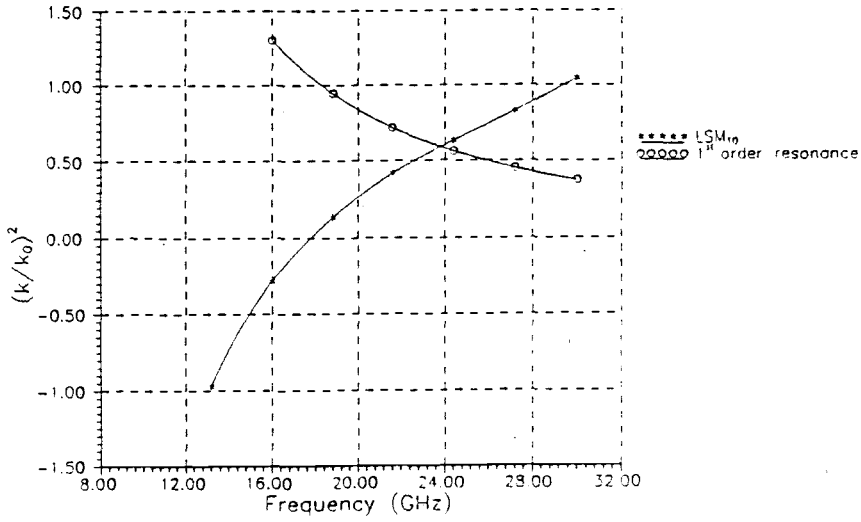

(e)

Figure 4–5. Continued: (e) Box dimension a=7.8mm, b=8.2mm, c=5.08mm, H_1=0.635mm, ϵ_1=9.6.

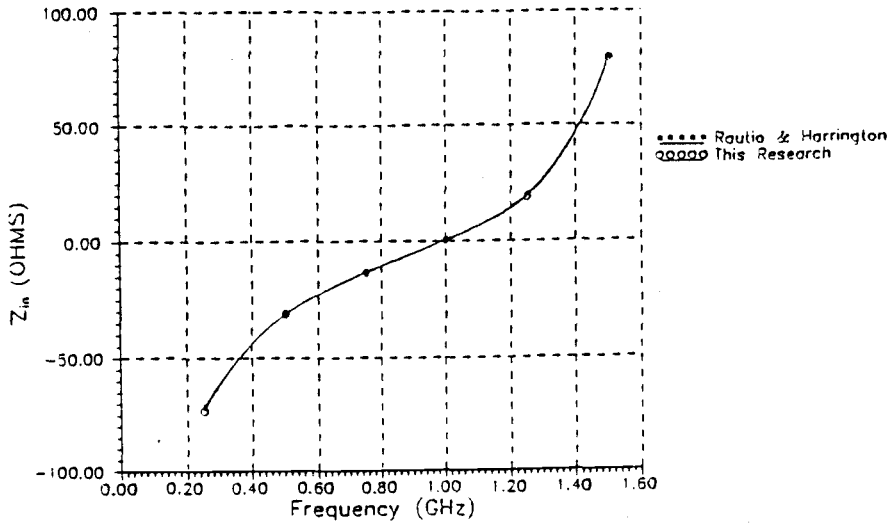

Figure 4-6. Stub input impedance (a=2cm, b=4cm, c=5cm, H_1=1cm, ϵ_1=10).

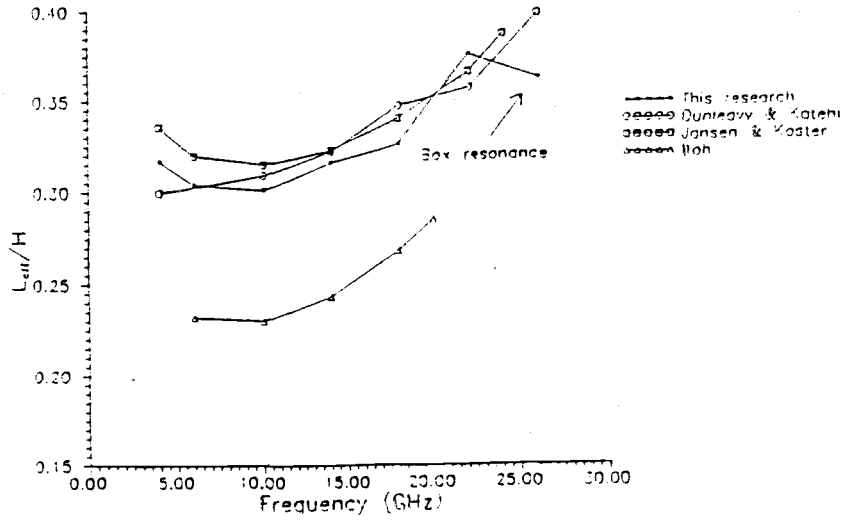

Figure 4-7. Effective length of open microstrip end (a=7.747mm, c=5.08mm, H_1=0.635mm, ϵ_1=9.6, W/H_1=1.57).

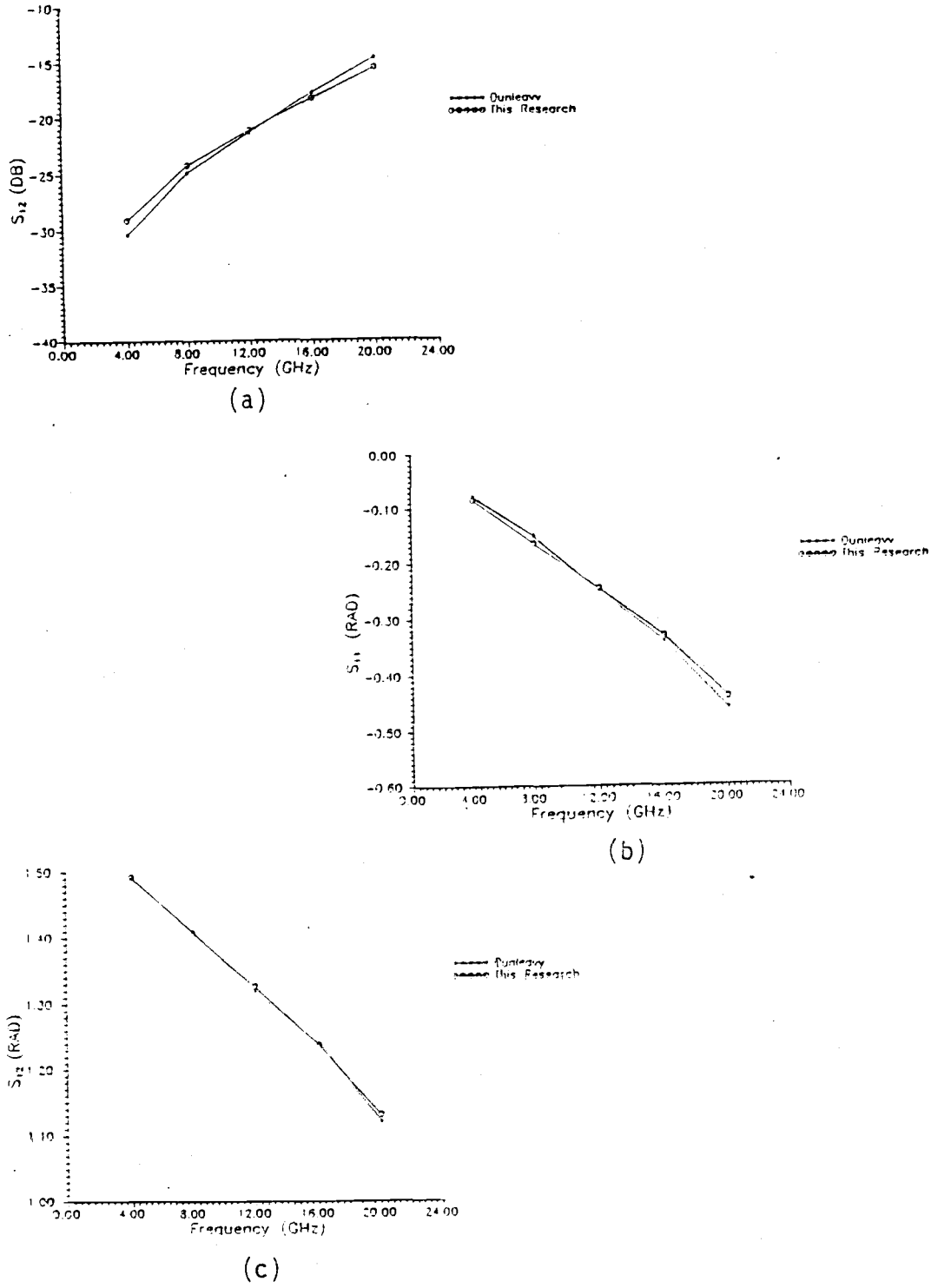

Figure 4-8. S parameter for microstrip gap discontinuity (a=c=6.35mm, H_1=0.635mm, W/H_1=1, g=0.381mm, ϵ_1=9.7): (a) S_{11} (MAG); (b) S_{11} (RAD); (c) S_{12} (RAD).

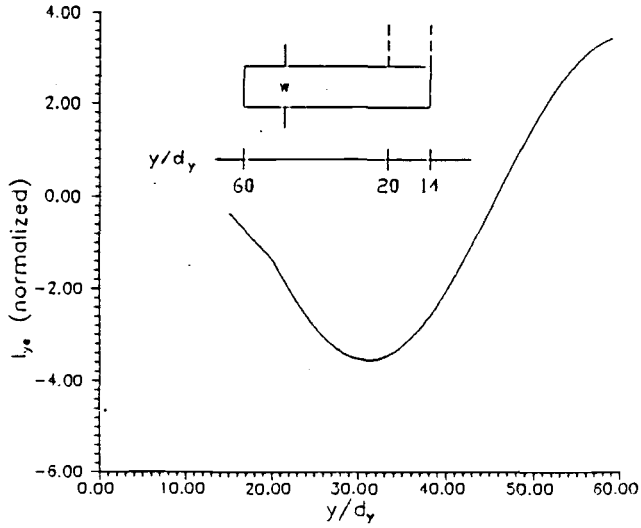

(a)

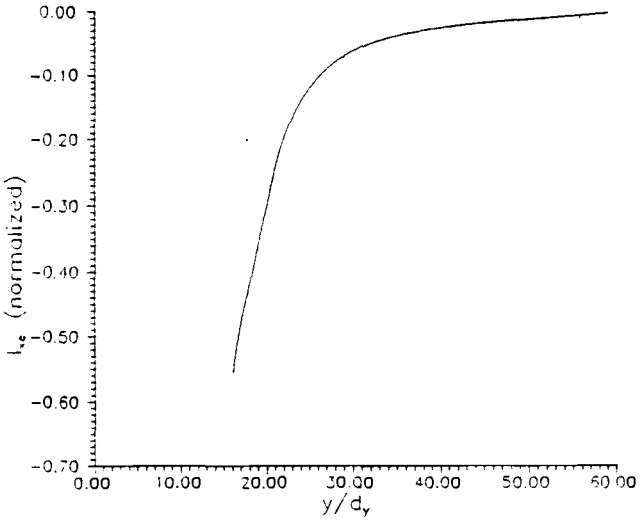

(b)

Figure 4-9. Current on resonant right angle bend- even mode (a=b=12.7mm, c=3.81mm, H_1=0.635mm, ϵ_1=9.8, W/H_1=1): (a) Total y-directed current on stripline; (b) Total x-directed current on stripline.

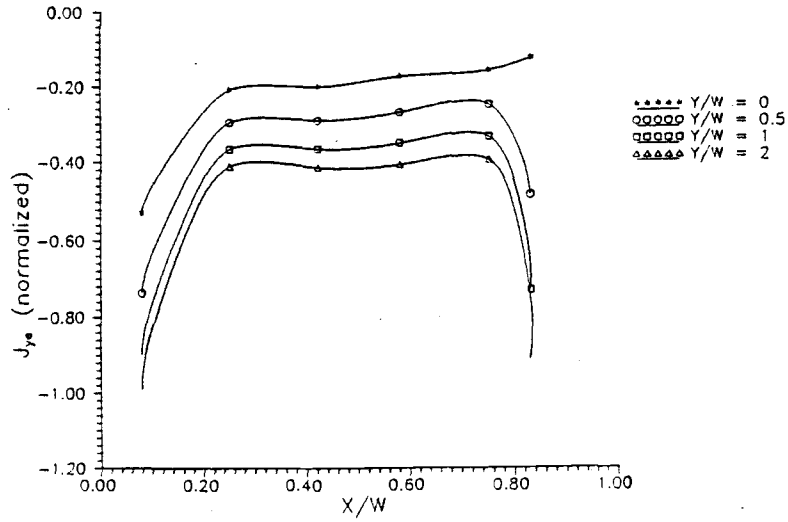

(a)

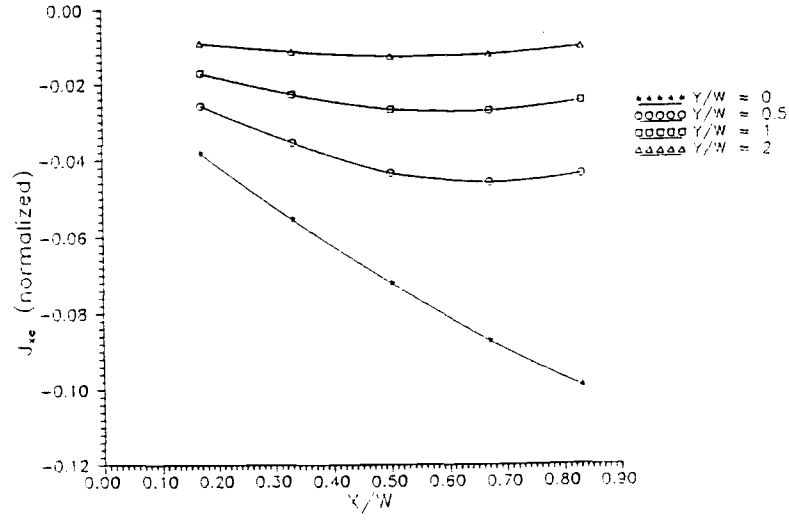

(b)

Figure 4-10. Current distribution on resonant right angle bend - even mode (dimensions as in Figure 4-8): (a) Y-directed current density at various stripline cross sections; (b) X-directed current density at various stripline cross sections.

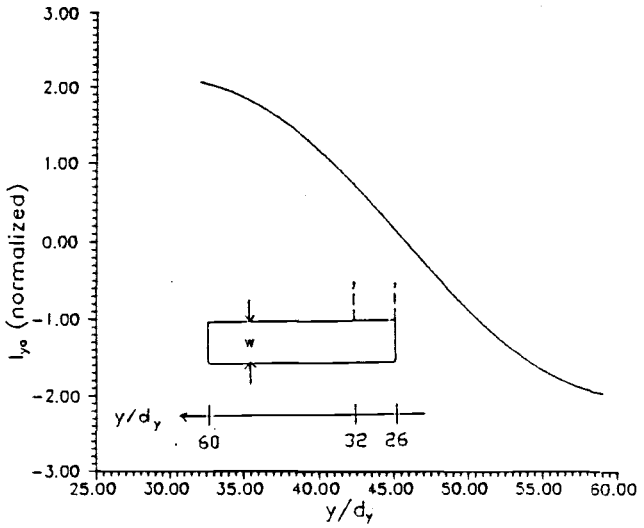

(a)

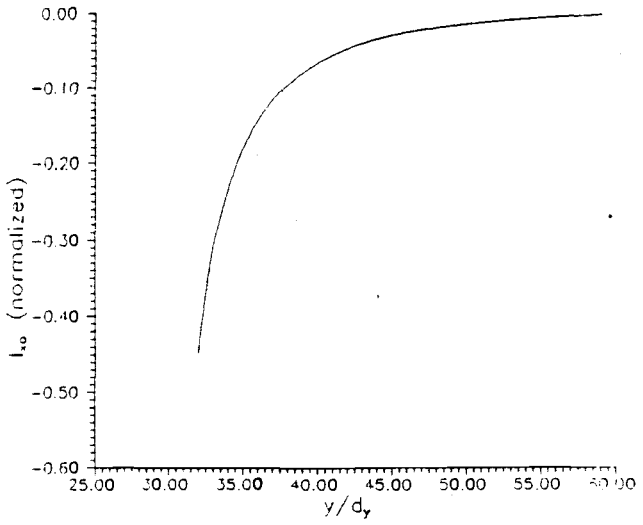

(b)

Figure 4-11. Current on resonant right angle bend - odd mode (dimensions as in Figure 4-8): (a) Total y-directed current on stripline; (b) Total x-directed current on stripline.

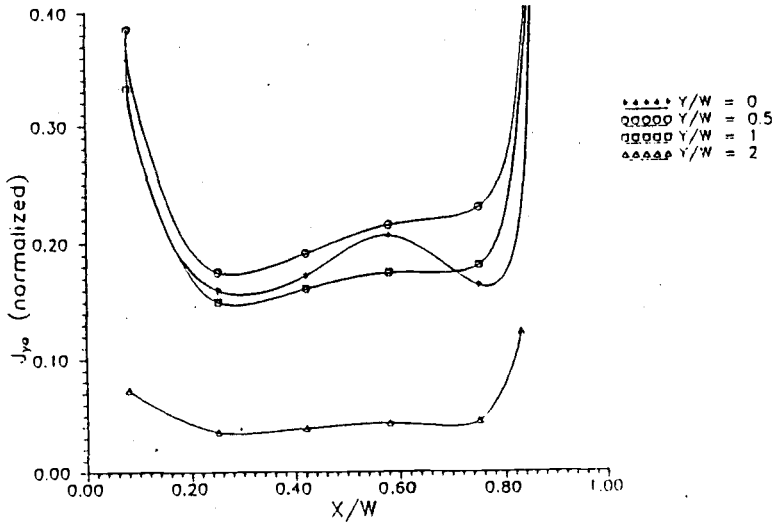

(a)

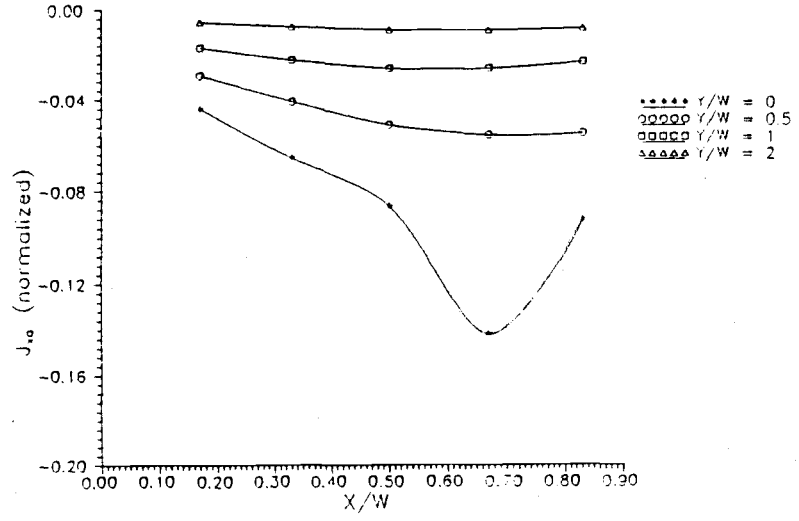

(b)

Figure 4-12. Current distribution on resonant right angle bend - odd mode (dimensions as in Figure 4-8): (a) Y-directed current density at various stripline cross sections; (b) X-directed current density at various stripline cross sections.

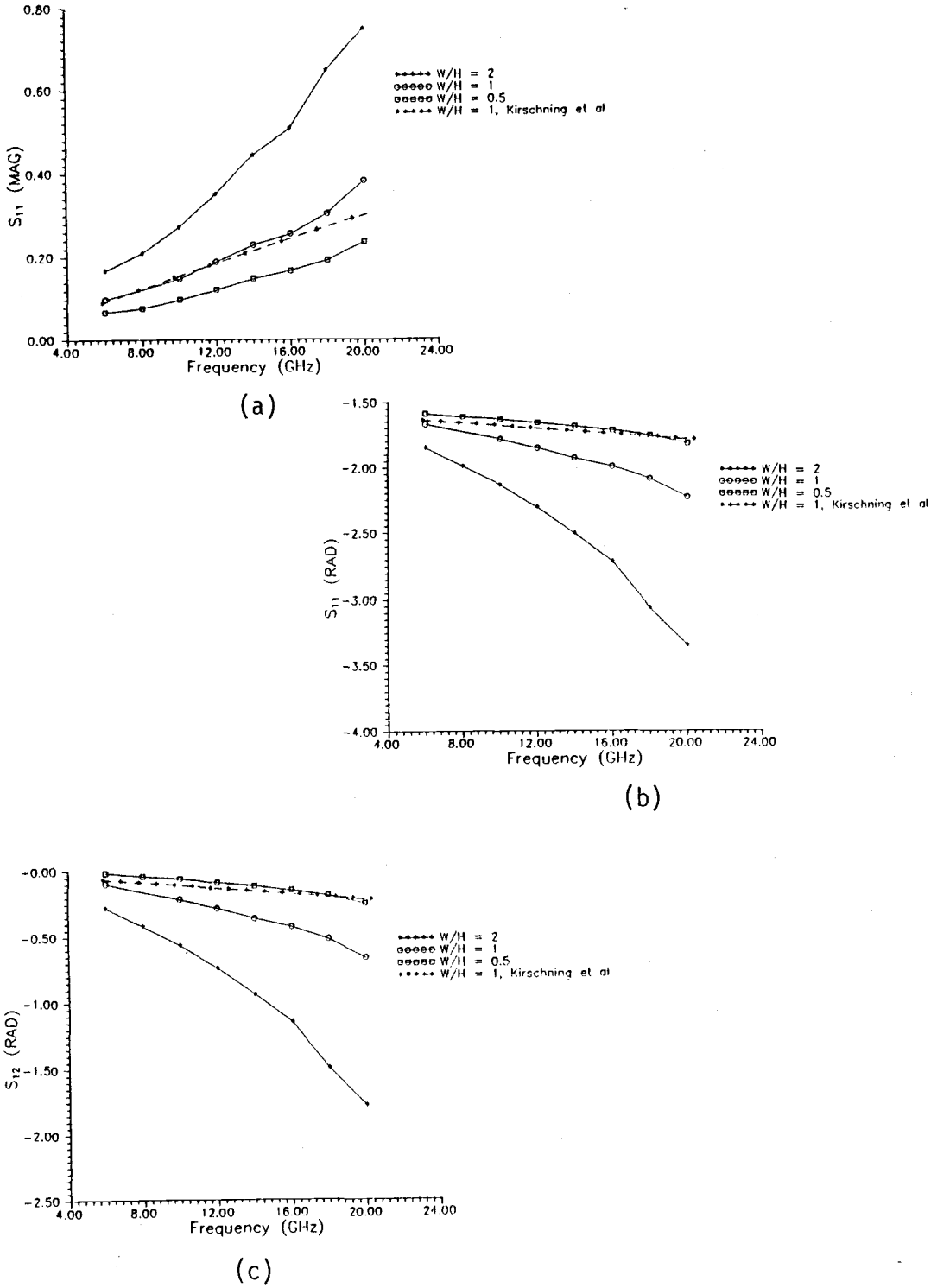

Figure 4-13. S parameter of right angle bend for various W/H_1 ratios ($a=b=12.7mm$, $c=3.18mm$, $H_1=0.635mm$, $\epsilon_1=9.8$): (a) S_{11} (MAG); (b) S_{11} (RAD); (c) S_{12} (RAD).

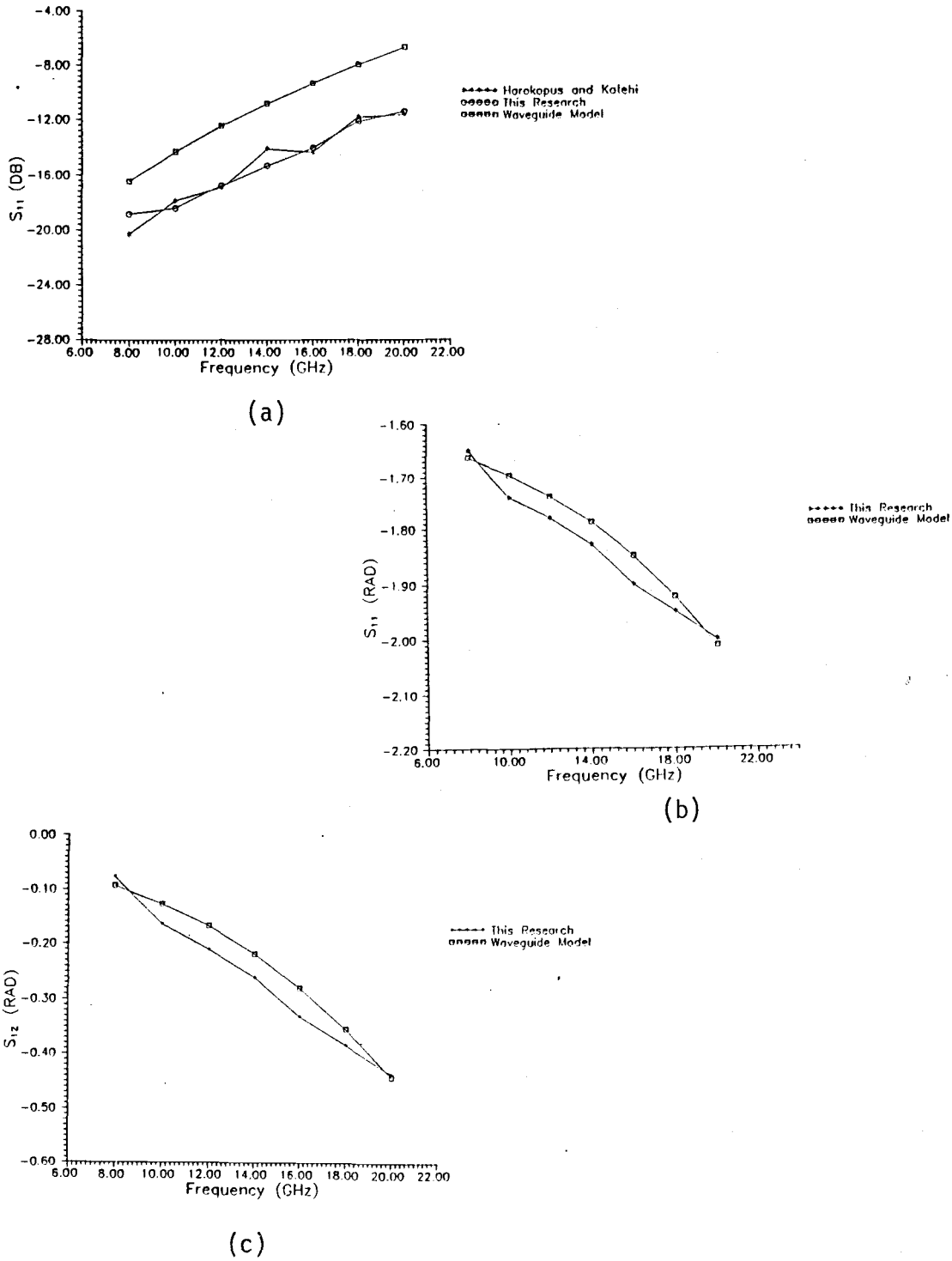

Figure 4-14. S parameter of right angle bend (a=b=10.84mm, c=5.08mm, ϵ_1=9.9, W/H_1=1): (a) S_{11} (MAG); (b) S_{11} (RAD); (c) S_{12} (RAD).

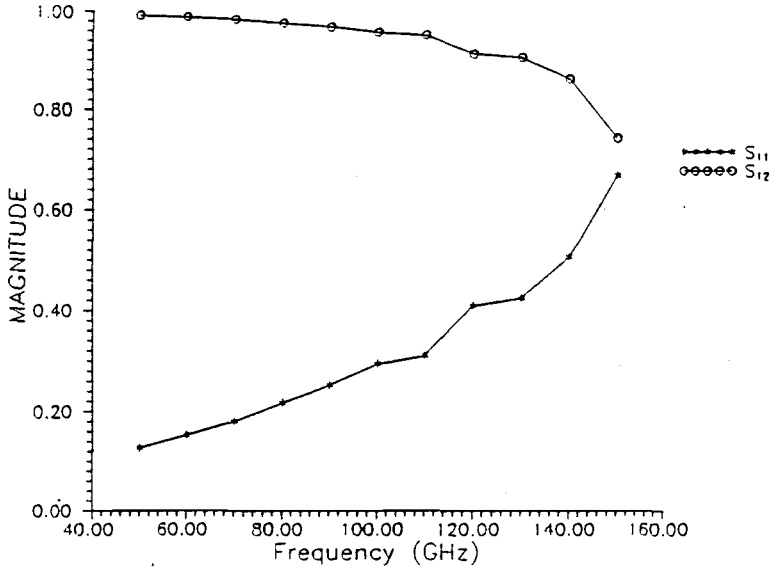

(a)

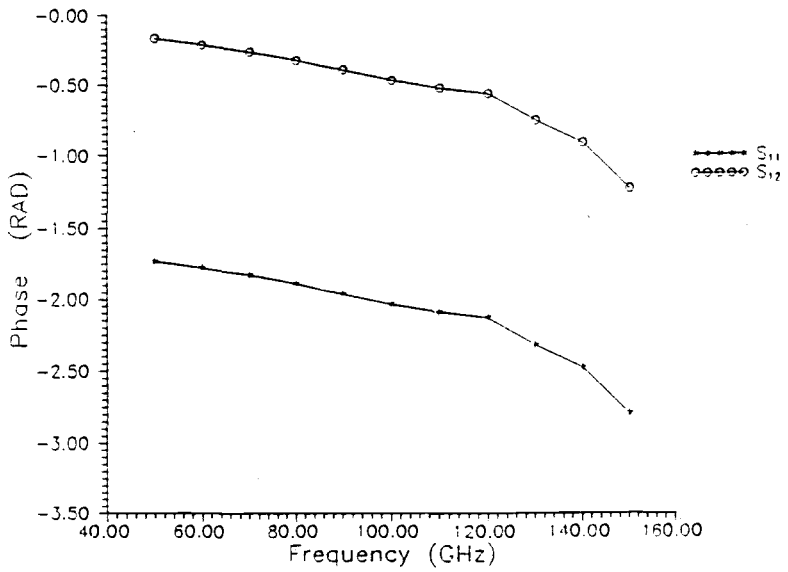

(b)

Figure 4-15. S parameter of right angle bend, double-layered substrate (a=b=1.9mm, c=1.05mm, H_1=0.1mm, H_2=0.005mm, ϵ_1=12.9, ϵ_2=3.9, W=0.100mm): (a) S_{11} (MAG), S_{12} (MAG); (b) S_{11} (RAD), S_{12} (RAD).

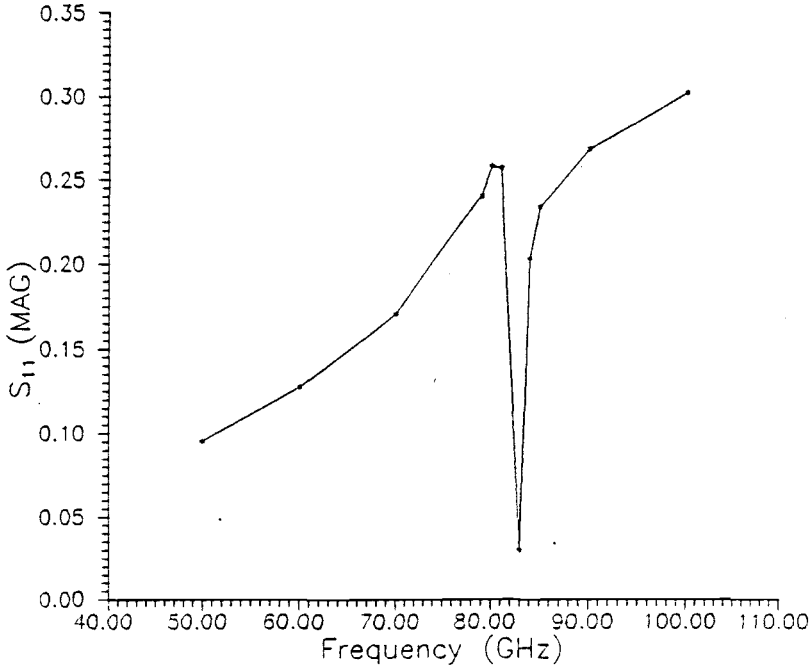

Figure 4-16. S_{11} (MAG) of right angle bend at box resonance (a=b=1.9mm, c=0.2mm, H_1=0.1mm, W/H_1=1).

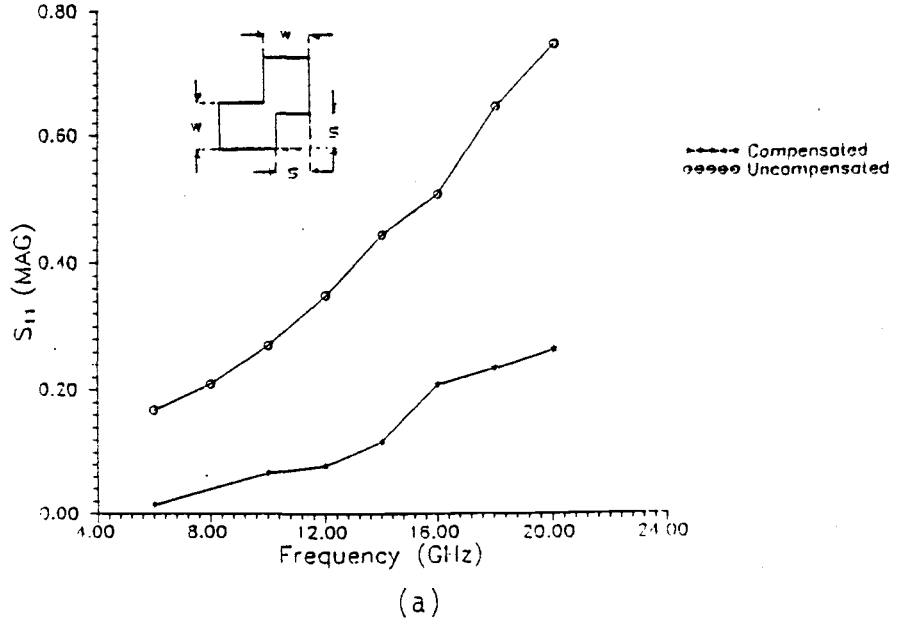

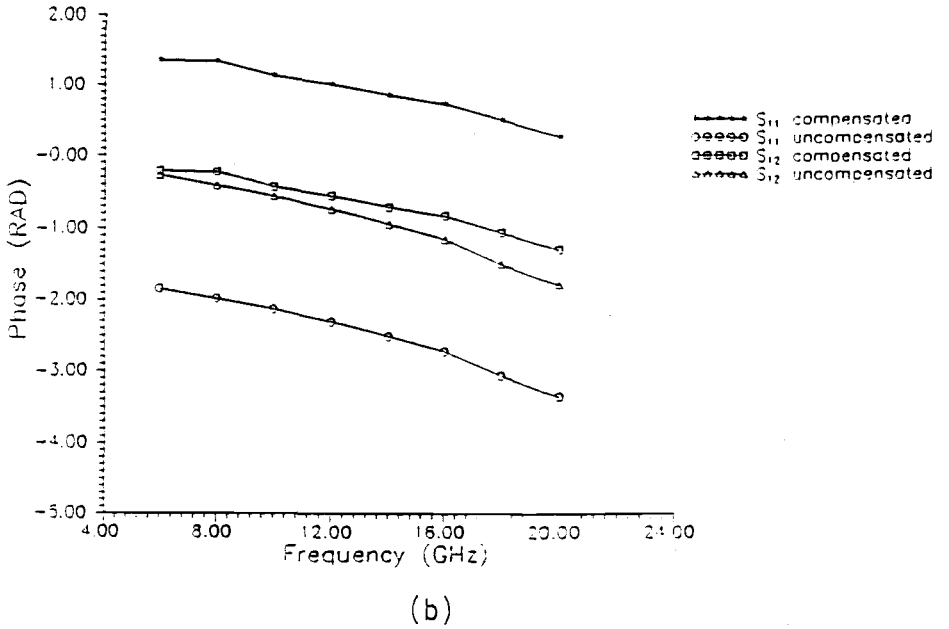

Figure 4–17. Comparison of S parameter for compensated bend and right angle bend (a=b=12.7mm, c=3.18mm, H_1=0.635mm, ϵ_1=9.8, W/H_1=2): (a) S_{11} (MAG); (b) S_{11} (RAD), S_{12} (RAD).

5. SUMMARY AND SUGGESTIONS FOR FUTURE STUDY

The purpose of this work was twofold. A quasi-static analysis was applied to compute equivalent circuit parameters of coupled microstrip bend discontinuities. Due to the large sensitivity of the parameter identification process for single and coupled microstrip corners an excess formulation was applied in conjunction with an efficient mathematical treatment. It was demonstrated that significant coupling occurs between adjacent microstrip corners where the stripline separation is identical to the line width. Such configurations are frequently encountered in practical integrated circuit structures such as spiral inductors and transformers. The equivalent circuit can be used in the design of various (M)MIC components such as filters, couplers, spiral inductors and high speed interconnects.

The second part of this work was concerned with the rigorous 3D simulation of lossless (M)MIC circuit structures. A new formulation was presented which leads to the efficient computation of network parameters for various (M)MIC components on a single and doubled layered dielectric medium. It is now possible to simulate resonance experiments even for two-dimensional, locally defined current distributions. The presented method allows the analysis of distributed passive structures including proximity and housing effects such as parasitic waveguide modes and associated box resonances.

Contrary to common belief, it was found that the implementation of the specialized, quasi-static solution is a time consuming, tedious

process as compared to the dynamic case presented in the second part of this work.

Further, future development of the dynamic model presented here could be directed towards the development of triangular subdomain basis functions which could replace the rooftop functions and make the method truly adaptable to arbitrarily shaped conductor geometries. In addition, Green's function of arbitrary dielectric layers can be readily incorporated. Multilevel metallization pattern and circuits should then be analyzed. A development of the associated Green's function is recommended. Finally the incorporation of both conductor and dielectric losses as well as finite thickness metallization pattern will create a rigorous fullwave simulator for distributed passive circuits which accommodates the requirement of state-of-the-art (M)MIC technology.

BIBLIOGRAPHY

1. Altschuler H.M., Oliner A.A., "Discontinuities in the center conductor of symmetric strip transmission line," IRE Trans. Microwave Theory and Techniques, vol. MTT-8, pp. 328-339, 1960.

2. Oliner A.A., "Equivalent circuits for discontinuities in balanced strip transmission lines," Trans. on Microwave Theorie and Tech., vol. MTT-3, pp. 134-143, November 1955.

3. Farrar A., Adams A.T., "Computation of lumped microstrip capacities by matrix methods: rectangular sections and end effect," IEEE Trans. on Microwave Theorie and Tech., vol. MTT-19, pp. 495-496, May 1971.

4. Farrar A., Adams A.T., "Matrix methods for microstrip three-dimensional problems," Trans. on Microwave Theorie and Tech., vol. MTT-20, pp. 497-504, August 1972.

5. Silvester P., Benedek P., "Equivalent capacitance of microstrip open circuits," Trans. on Microwave Theorie and Tech., vol. MTT-20, pp. 511-516, August 1972.

6. Benedek P., Silvester P., "Equivalent capacitance for microstrip gaps and steps," Trans. on Microwave Theorie and Tech., vol. MTT-20, pp. 729-733, September 1972.

7. James D.S., Tse S.H., "Microstrip end effects," Electronic Letters, vol. 8, No. 2, 1972.

8. Silvester P., Benedek P., "Microstrip discontinuity capacitances for right angle bends, T-junctions and crossings," Trans. on Microwave Theorie and Tech., vol. MTT-21, pp. 341-346, May 1973. Correction: vol. MTT-21, p 456, 1973.

9. Horton R., "Equivalent representation of an abrupt impedance step in microstrip line," Trans. on Microwave Theorie and Tech., vol. MTT-21, pp. 562-564, August 1973.

10. Horton R., "A static approximation of the inductive and capacitive elements associated with some common microstrip discontinuities," Proc. European Microwave Conf., paper B.8.4, pp. 1-4, 1973.

11. Horton R., "The electrical characterization of a right-angled bend in microstrip line," Trans. on Microwave Theorie and Tech., vol. MTT-21, pp. 427-429, June 1973.

12. Gopinath A., Easter A., "Moment method of calculating discontinuity inductance of microstrip right angle bends," Trans. on Microwave Theorie and Tech., vol. MTT-22, pp. 880-883, October 1974.

13. Thompson A.F., Gopinath A., "Calculation of microstrip discontinuity inductances," Trans. on Microwave Theorie and Tech., vol. MTT-23, pp. 648-655, August 1975.

14. Easter B., "The equivalent circuit of some microstrip discontinuities," Trans. on Microwave Theorie and Tech., vol. MTT-23, pp. 655-660, August 1975.

15. Hammerstad E.O., "Equations for microstrip circuits design," Proc. European Microwave Conf., Hamburg, paper C.4.2, 1975.

16. Gopinath A. et al., "Equivalent circuit parameters of microstrip step change in width and cross junctions," Trans. on Microwave Theorie and Tech., vol. MTT-24, pp. 142-144, 1976.

17. Neale B.M., Gopinath A., "Microstrip discontinuity inductances," Trans. on Microwave Theorie and Tech., vol. MTT-26, pp. 827-830, October 1978.

18. Gopinath A., Gupta C., "Capacitance parameters of discontinuities in microstrip lines," Trans. on Microwave Theorie and Tech., vol. MTT-26, pp. 831-836, October 1978.

19. Garg R., Bahl I.J., "Microstrip discontinuities," Internat. J. Electronics, vol. 45, No 1, pp. 81-87, 1978.

20. Anders P., Arndt F., "Kompensierte Mikrostrip- Leitungsknicke mit beliebigem Knickwinkel," Arch. Elektr. Uebertragungstech. (AEU), vol. 33, pp. 371-375, 1979.

21. Hammerstad E., Jensen O., "Accurate models for microstrip computer aided design," IEEE MTT-S Internat. Microwave Symp. Digest, pp. 407-409, 1980.

22. Hammerstad E., "Computer-aided design of microstrip couplers with accurate discontiuity modes," IEEE MTT-S Internat. Microwave Symp. Digest, pp. 54-56, 1981.

23. Hill A., Tripathi V.K., "Analysis and modelling of coupled right angle microstrip bend discontinuities," IEEE MTT-S, Intl. Microwave Symp. Digest, pp. 1143-1146, 1989.

24. Hill A., Tripathi V.K., "Adaptive algorithm for the analysis of a microstrip discontinuity inductance," 5th annual review of progress, ACES Proceedings, pp. 183-189, 1989.

25. Wolff I. et al., "Calculation method for microstrip discontinuities and T-junctions," Electronic Letters, vol. 8, pp. 177-179, 1972.

26. Chadha R., Gupta K.C., "Compensation of discontinuities in planar transmission lines," Trans. on Microwave Theorie and Tech., vol. MTT-30, December 1982.

27. Silvester P., "TEM properties of microstrip transmission lines," Proc. IEE, vol. 115, January 1968.

28. Cohen H.D., "A method for the automatic generation of triangular elements on a surface," Int. J. Num. Meth. Eng. vol. 15, pp. 470-476, 1980.

29. Heighway E.A., Biddlecombe C.S., "Two dimensional automatic triangular mesh generation for the finite element electromagnetics package PE2D," IEEE Trans. Magnetics, vol. MAG-18, pp. 594-598, 1982.

30. Lindholm D.A., "Automatic triangular mesh generation on surface of polyhedra," IEEE Trans. Magnetics, vol. MAG-19, pp. 2539-2542, 1983.

31. Sadek E.A., "A scheme for the automatic generation of triangular finite elements," Int. J. Num. Meth. Eng., vol. 15, pp. 1813-18-22, 1980.

32. Lawson C.L., "Software for C^1 surface interpolation," in Mathematical Software 3, edited by Rice J.C., 1977.

33. Douville R.J.P., James D.S., "Experimental study of symmetric microstrip bends and their compensation," IEEE Trans. on Microwave Theorie and Tech., vol. MTT-26, pp. 175-182, March 1978.

34. Hoefer W.J.R., Chattopadhyay A., "Evaluation of the equivalent circuit parameters of microstrip discontinuities through perturbation of a resonant ring," IEEE Trans. on Microwave Theorie and Tech., pp. 1067-1071, December 1975.

35. Rizzoli V., Lipparini A., "A resonance method for the broad-band characterization of general two-port microstrip disconinuities," IEEE Trans. on Microwave Theorie and Tech., vol. MTT-29, pp. 655-660, July 1981.

36. Kirschning M. et al., "Measurement and computer aided modelling of microstrip discontinuities by an improved resonator method," IEEE MTT-S Intl. Microwave Symp. Digest, pp. 595-597, 1983.

37. Rao S.M. et. al, "Electromagnetic scattering by surface of arbitrary shape," IEEE Trans. on Microwave Theory Tech., vol. MTT-20, pp. 409-418, May 1982.

38. Wilton D.R. et al., "Potential integrals for uniform and linear source distributions on polygonal and polyhedral domains," IEEE Trans. on Antennas Prop. vol. AP-32, pp. 276-281, March 1984.

39. Mautz J.R., Harrington R.F., "Calculation of the excess capacitance of a microstrip discontinuity," Technical Report, Syracuse University, February 1984.

40. Mautz J.R., Harrington R.F., "Calculation of the excess inductance of a microstrip discontinuity," Technical Report, Syracuse University, 1984.

41. Groebner W., Hofreiter N., "Integraltafel," Spinger Verlag, 1950.

42. Itoh T., "Analysis of microstrip resonators," IEEE Trans. on Microwave Theorie and Tech., vol. MTT-22, pp. 946-952, November 1974.

43. Cendes Z.J., Lee J., "The transfinite element method for modeling MMIC devices," IEEE Trans. on Microwave Theorie and Tech., vol. MTT-36, pp. 1639-1649, December 1988.

44. Chang W.L., "Filterelemente und Resonatoren aus geschirmten Streifenleitungen mit sprunghafter Breitenaenderung," PhD thesis, TH Darmstadt, West Germany, 1977.

45. Chu T.S., Itoh T., "Analysis of microstrip discontinuity by the modified residue calculus technique," IEEE Trans. on Microwave Theorie and Tech., vol. MTT-33, pp. 1024-1028, October 1985.

46. Katehi P.B., Alexopoulos N.G., "Frequency-Dependent characteristics of mocrostrip discontinuities in millimeter-wave interated circuits," IEEE Trans. on Microwave Theorie and Tech., vol. MTT-33, pp. 1029-1035, October 1985.

47. Jackson R.W., Pozar D.M., "Full-Wave analysis of microstrip open-end and gap discontinuity," IEEE Trans. on Microwave Theorie and Tech., vol. MTT-33, pp. 1036-1042, October 1985.

48. Jackson R.W., "Full-Wave, finite element analysis of irregular microstrip discontinuities," IEEE Trans. on Microwave Theorie and Tech., vol. MTT-37, pp. 81-89, January 1989.

49. Kirschning M., "Entwicklung von Naeherungsmodellen fuer den rechnergestuetzten Entwurf von hybriden und monolithischen Schaltungen in Mikrostreifenleitungstechnik," PhD thesis, Universitaet Duisburg, 1984.

50. Koster N.H.L., Jansen R.H., "The microstrip step discontinuity: a revised description," IEEE Trans. on Microwave Theorie and Tech., vol. MTT-34, pp. 213-222, February 1986.

51. Koster N.H.L., "Zur charakterisierung der frequenzabhaengigen Eigenschaften von Diskontinuitaeten in planaren Wellenleitern," PhD thesis, Universitaet Duisburg, 1984.

52. Jansen R.H., "Hybrid mode analysis of end effects of planar microwave and millimetrewave transmission lines," IEE Proceedings, vol. 128, Pt.H, no.2, pp. 77-86, April 1981.

53. Jansen R.H., "The spectral-domain app.roach for microwave integrated circuits," IEEE Trans. on Microwave Theorie and Tech., vol. MTT-33, pp. 1043-1056, October 1985.

54. Mosig J.R., "Arbitrarily shaped microstrip structures and their analysis with a mixed potential integral equation," IEEE Trans. on Microwave Theorie and Tech., vol. MTT-36, pp. 314-323, February 1988.

55. Dunleavy L.P., Katehi P.B., "A generalized method for analyzing shielded thin microstrip discontinuities," IEEE Trans. on Microwave Theorie and Tech., vol. MTT-36, pp. 1753-1766, December 1988.

56. Dunleavy L.P., Katehi P.B., "Shielding effects in microstrip discontinuities," IEEE Trans. on Microwave Theorie and Tech.,vol. MTT-36, pp. 1767-1774, December 1988.

57. Dunleavy L.P., "Discontinuity characterization in shielded microstrip: a theoretical and experimental study," PhD thesis, University of Michigan 1988.

58. Glisson A.W., Wilton D.R., "Simple and efficient numerical methods for problems of electromagnetic radiation and scattering from surfaces," IEEE Trans. on Antennas and Propagation, vol. AP-28, pp. 593-603, September 1980.

59. Harrington R.F., "Time-harmonic electromagnetic fields," McGraw-Hill, 1961.

60. Harrington R.F., "Field Computation by Moment Methods," New York: Macmillan, 1968.

61. Collin R.E., "Field theory of guided waves," New York, McGraw-Hill, 1960.

62. Rautio J.C., "A time-harmonic electromagnetic analysis of shielded microstrip circuits," PhD thesis, Syracuse University, 1986.

63. Rautio J.C., Harrington R.F., "An electromagnetic time- harmonic analysis of shielded microstrip circuits," IEEE Trans. on Microwave Theorie and Tech., vol. MTT-35, pp. 726-730, August 1987.

64. Schmidt L.P., "Zur feldtheoretischen Berechnung fon transversalen Diskontinuitaeten in Mikrostrip-Leitungen," PhD thesis, RWTH Aachen, West Germany, 1979.

65. Sorrentino R., Itoh T., "Transverse resonance analysis of finline disconinuities," IEEE Trans. on Microwave Theorie and Tech., vol. MTT-32, pp. 1633-1638, December 1984.

66. Uwano T., Sorrentino R., Itoh T., "Characterization of strip line crossing by transverse resonance analysis," IEEE Trans. on Microwave Theorie and Tech., vol. MTT-35, pp. 1369-1376, 1987.

67. Wertgen W., Jansen R.H., "Spectral iterative techniques for the full-wave 3D analysis of (M)MIC structures," IEEE MTT-S Intl. Microwave Symp. Digest, pp. 709-712, 1988.

68. Gupta K.C. ,"Modeling of discontinuities in planar transmision lines - an overview," IEEE MTT-S Intl. Microwave Symp. Digest, Workshop on CAD oriented modelings of discontinuities in microwave/mmwave transmission structures, 1988.

69. Jansen R.H., Wertgen W., "Modular source-type 3D analysis of scattering parameters for general discontinuities, components and coupling effects in (M)MICs," 17th European Microwave Conference, pp. 427-432, 1987.

70. Nakatani A., Maas S.A., Castaneda J., "Modeling of high frequency MMIC pasive components," IEEE MTT-S Intl. Microwave Symp. Digest, pp. 1139-1142, 1989.

71. Jansen R.H., Wiemer L., "Full-Wave theory based development of mm-wave circuit models for microstrip open end, gap, step, bend and tee," IEEE MTT-S Intl. Microwave Symp. Digest, pp. 779-782, 1989.

72. Skrivervik A., Mosig J.R., "Equivalent circuits of microstrip discontinuities including radiation eeffects," IEEE MTT-S Intl. Microwave Symp. Digest, pp. 1147-1150, 1989.

73. Harokopus W.P., Katehi P.B., "An accurate characteriztion of open microstrip discontinuity including radiation losses," IEEE MTT-S Intl. Microwave Symp. Digest, pp. 231-234, 1989.

74. Worm B.S., Pregla R., "Hybrid-Mode analysis of arbitrarily shaped planar microwave structures by the method of lines," IEEE Trans. on Microwave Theory and Tech., vol. MTT-32, pp. 191-196, February 1984.

75. Worm B.S., "Analyse planarer Mikrowellenstrukturen beliebiger Kontur," PhD Fernuniversitaet Hagen, 1983.

76. Chen Z., Gao B., "Deterministic approach to full-wave analysis of discontinuities in MICs using the method of lines," IEEE Trans. on Microwave Theory and Tech., vol. MTT-37, pp. 606-611, March 1989.

77. Hoffman R.K., "Integrierte Microwellenschaltungen," Springer Verlag, 1983.

78. Jansen R.H., Koster N.H.L, "Accurate results on the end effect of single and coupled lines for use in microwave circuit design," AEU, Band 34, pp. 453–459, 1980.

79. Lehner G., "Theorie der Felder und Wellen," Lecture notes, University of Stuttgart, 1983.

80. Menzel W., Wolff I., "A method for calculating the frequency-dependent properties of microstrip discontinuities," IEEE Trans. on Microwave Theory and Tech., vol. MTT-25, pp. 107–112, February 1977.

APPENDICES

A.1 Analytical Expression for Flux Due to Semi-Infinite Surface Current

The flux on a microstrip line due to a semi-infinite surface current is evaluated in equations (3.2.34) and (3.3.46)-(3.3.49). The type of integral that occurs in the evaluation of the flux is given by

$$I = \int A(J_a^-(z,x))\ J_{a1}(x)\ dS_1 \tag{A1.1}$$

where J_{a1} is a constant surface current on S_1. S_1 extends from $z = z_1$ to $z = z_2$ and has a constant width of ΔW. J_a^- exists on a uniform microstrip line that extends from $z = -\infty$ to $z = 0$. The normal distance from the lower and upper edge of the strip where J_a^- exists to the center of S_1 is x_1 and x_2, respectively.

The following expressions are defined

$$f1(z,x) = \frac{z + \sqrt{(z^2 + x^2 + H_2^2)}}{z + \sqrt{(z^2 + x^2)}} \tag{A1.2}$$

$$f2(z,x,H_2) = \sqrt{(z^2 + x^2 + H_2^2)} \tag{A1.3}$$

$$f3(x,z,H_2) = x + z + \sqrt{(z^2 + x^2 + H_2^2)} \tag{A1.4}$$

$$f4(z,x) = \frac{x + \sqrt{(z^2 + x^2 + H_2^2)}}{x + \sqrt{(z^2 + x^2)}} \tag{A1.5}$$

$$f5(x,z,H_2) = z + \sqrt{(z^2 + x^2 + H_2^2)} \tag{A1.6}$$

$$f6(x,z,H_2) = \frac{f5^2(x,z,H_2) + 2\ x\ f5(x,z,H_2) + x^2 + H_2^2}{f5(x,z,H_2)} \tag{A1.7}$$

Loss of significance occurs in $f1(z,x)$ for $z < 0$, therefore for $z < 0$ $f1(z,x)$ is replaced by

$$f1(z,x) = \frac{(x^2 + H_2^2)(-z + \sqrt{(z^2 + x^2)})}{x^2(-z + \sqrt{(z^2 + x^2 + H_2^2)})} \tag{A1.8}$$

Loss of significance occurs in $f4(z,x)$ for $x < 0$, therefore for $x < 0$ $f4(z,x)$ is replaced by

$$f4(z,x) = \frac{(z^2 + H_2^2)(-x + \sqrt{(z^2 + x^2)})}{z^2(-x + \sqrt{(z^2 + x^2 + H_2^2)})} \tag{A1.9}$$

Let

$$\begin{aligned} I_1(z) = {} & x_2\ z\ \ln(f1(z,x_2)) - x_1\ z\ \ln(f1(z,x_1)) \\ & - x_2/2\ (f2(z,x_2,H_2) - f2(z,x_2,0)) \\ & + x_1/2\ (f2(z,x_1,H_2) - f2(z,x_1,0)) \\ & + z^2/2\ \ln(f4(z,x_2)\ /\ f4(z,x_1)) \\ & - H_2^2/2\ \ln(f6(z,x_2,H_2)\ /\ f6(z,x_1,H_2)) \\ & + H_2\ (f3(x_2,z,H_2) - \frac{H_2^2 + x_2\ f3(x_2,z,H_2)}{f3(x_2,z,H_2) - x_2}) \\ & \cdot \tan^{-1}(f3(x2,z,H_2)/H_2) \end{aligned}$$

$$+ H_2^2 \ln \frac{[(z + f2(z,x_2,H_2)][H_2^2 + f3^2(x_1,z,H_2)]}{[H_2^2 + f3^2(x_2,z,H_2)][(z + f2(z,x_1,H_2)]} \qquad \text{(A1.10)}$$

where

$$H_2 = 2 \cdot H \qquad \text{(A1.11)}$$

Then

$$I = (I_1(z_2) - I_1(z_1)\Delta W \qquad \text{(A1.12)}$$

The analytical expressions have been verified by numerical evaluation of the integral (A1.1). In the development of (A1.1) use was made of integration tables by Groebner and Hofreiter [41].

A.2 Potential Due to Charge on Semi-Infinite Microstrip Line on Dielectric Interface

The electrostatic potential due to a semi-infinite microstrip line of constant charge density q on a substrate with relative dielectric constant ϵ_r is evaluated. The strip extends from $z = -\infty$ to $z = 0$ and from $x = x_1$ to $x = x_2$, it is mounted at $y = H$ over a ground plane. This type of potential occurs on the right hand side of (3.2.16) and (3.3.18). The potential U at the field point (x,z,H), $z > 0$ is given by

$$U = \frac{q}{2\pi\epsilon_0} \sum_{n=0}^{\infty} K^n F(n) \tag{A2.1}$$

where ϵ_0 is the dielectric constant in air, K is the image constant as defined in [27]

$$K = \frac{1-\epsilon_r}{1+\epsilon_r} \tag{A2.2}$$

Let

$$P(x,n) = x \ln\left(\frac{z + \sqrt{x^2 + z^2 + [(n+1)\,H_2]^2}}{z + \sqrt{x^2 + z^2 + [n\,H_2]^2}}\right)$$

$$+ z \ln\left(\frac{x + \sqrt{x^2 + z^2 + [(n+1)\,H_2]^2}}{x + \sqrt{x^2 + z^2 + [n\,H_2]^2}}\right)$$

$$+ 2(n+1)\,H_2 \tan^{-1}\left(\frac{x + |z| + \sqrt{x^2 + z^2 + [(n+1)\,H_2]^2}}{(n+1)\,H_2}\right)$$

$$- 2\, n\, H_2 \tan^{-1}\left(\frac{x + |z| + \sqrt{x^2 + z^2 + [n\, H_2]^2}}{[n\, H_2]^2}\right) \qquad \text{(A2.3)}$$

with $H_2 = 2\, H$, then

$$F(n) = P(x_2, n) - P(x_1, n) \qquad \text{(A2.4)}$$

A.3 Potential Due to Sheet of Charge on Triangular Region on Dielectric Interface

In the testing procedure of the moment method the electrostatic potential due to a constant surface charge density q over a triangular region situated on a dielectric substrate over a ground plane is evaluated. This type of potential occurs on the left hand side of (3.2.16) and (3.3.18). The potential U is given by

$$U = \frac{q}{2\pi\epsilon_0(1 + \epsilon_r)} \left(F(0) - (1 - K) \sum_{n=1}^{\infty} K^{n-1} F(n)\right) \qquad \text{(A3.1)}$$

where F(n) is the potential of the image of the triangular sheet at a distance of n 2 H normal to the substrate surface in free space. The expression for F(0) has been developed in [38]. F(n) is obtained from F(0) in [38] by replacing H by n 2 H.

A.4 Magnetostatic Vector Potential Due to Semi-Infinite Current

The normalized magnetostatic vector potential due to a semi-infinite microstrip line of z-directed, constant current density J_a is evaluated. The current density J_a is assumed to exist for a pair of symmetrically coupled striplines with equal total current I and inductance coefficients L_{11w} and L_{12w}. The strip extends from $z = -\infty$ to $z = 0$ and from $x = x_1$ to $x = x_2$, it is mounted at $y = H$ over a ground plane. This type of potential occurs on the right hand side of (3.3.46)-(3.3.49) and (3.3.64)-(3.3.66). The z component of the magnetic vector potential A at the field point (x,z,H) is given by

$$A(J_a)/I = \frac{\mu_o}{4\pi I}\int_{x_1}^{x_2} J_a(x')\,\ln\frac{z+\sqrt{z^2+(x-x')^2+H_2^2}}{z+\sqrt{(z^2+(x-x')^2)}}\,dx' \qquad (A4.1)$$

if $J_a(x')$ is piecewise constant with magnitude I_{aj} for $x_{aj} < x < x_{aj+1}$, $j = 1, N_a$ then (A4.1) can be computed from

$$A(J_a)/I = (L_{11w} + L_{12w}) \cdot \sum_{j=1}^{N_a} I_{ja}\int_{x_1}^{x_2} \ln\frac{z+\sqrt{z^2+(x-x')^2+H_2^2}}{z+\sqrt{(z^2+(x-x')^2)}}\,dx' \qquad (A4.2)$$

the integral in (A4.2) is given by (A2.1) for $\epsilon_r = 1$ and $n = 1$. L_{11w} and L_{12w} are defined in section 3.3.1.

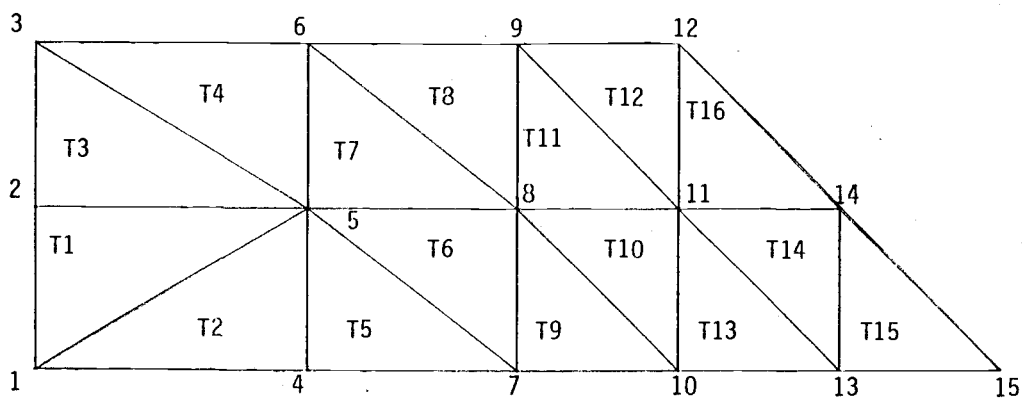

Figure A5-1. Sample grid geometry with numbering scheme.

```
NN,NTA,NTB,N,NB,NASTR,NBC,NTA11
15    12    16     4     2    10    13    12

BET,W,H
    .7853982E+00    .1000000E+01    .1000000E+01
    .1000000E+01   -.1000000E+01    .0000000E+00   -.2000000E+01
    .1000000E+01   -.9999999E+00    .0000000E+00    .0000000E+00
    .1000000E+01    .0000000E+00   -.2000000E+01    .0000000E+00
   -.2000000E+01   -.1000000E+01    .0000000E+00   -.1000000E+01

NVBC
   4     1     2     6     3     7     9    10    13    15    12

 X
   -.1000000E+01   -.5000000E+00    .0000000E+00   -.1000000E+01
   -.5000000E+00    .0000000E+00   -.1000000E+01   -.5000000E+00
    .0000000E+00   -.1000000E+01   -.5000000E+00    .0000000E+00
   -.1000000E+01   -.5000000E+00   -.9999999E+00

 Z
   -.2000000E+01   -.2000000E+01   -.2000000E+01   -.1151388E+01
   -.1151388E+01   -.1151388E+01   -.4999996E+00   -.4999996E+00
   -.4999996E+00    .0000000E+00    .0000000E+00    .0000000E+00
    .5000000E+00    .5000001E+00    .1000000E+01

NNT
   1     2     5     4     5     1     2     3     5     3
   6     5     4     5     7     5     8     7     5     6
   8     6     9     8     7     8    10     8    11    10
   8     9    11     9    12    11    10    11    13    11
  14    13    13    14    15    11    12    14

 NTT
  13    16

 NJ
   7     6     6     3     3     1

 NTJ
   1     2     3     4     5     6     7     6     7     8
   9    10    11    10    11    12    13    14    16    14
  15    16    13    14    15    16

 NL1
   2     1     3     6     4     7     8     5     6     9
   7    10    11     8     9    12    10    13    14    11
  13    12    10    11    13    11

 NL2
   1     4     2     3     7     8     6     7     5     6
  10    11     9    10     8     9    13    14    12    13
  15    11    13    14    15    14

 NVBA
  10    12
```